Bulk Nested-Network Nanoporous Gold via Dealloying

Vom Promotionsausschuss der

Technischen Universität Hamburg-Harburg

zur Erlangung des akademischen Grades

Doktor-Ingenieur (Dr.-Ing.)

genehmigte Dissertation

Von

Zhen Qi

aus

Shandong, China

2015

Abstract

Nanoporous metals attract great attention due to their interesting properties such as high surface area, low density and properties of metal itself, such as gold and platinum which possess unique catalytic property. Dealloying is a corrosion process that one or more elements are dissolved by chemical or electrochemical ways from an alloy, resulting in the formation of a 3D randomly distributed solid/void interconnected bicontinuous structure. It is a facile way to fabricate nanoporous metals with a uniform distribution of ligaments and pores with a shape from thin film to bulk samples.

Applications of porous microstructures in functional materials often impose conflicting requirements on the pore size, which may be met by hierarchical structures that combine porosity on distinctly different length scales. In order to investigate the advantage of hierarchical structures on charge and mass transport, a new two-step dealloying strategy is proposed to fabricate hierarchical nanoporous gold with a bulk size. A nanoscale network of solid ligaments forms the lower hierarchy level, which is nested within the geometrically similar, but much larger, network of the upper hierarchy level. Starting out from a dilute solid solution of Au in Ag, controlled electrochemical corrosion yields a nanoporous Ag-Au alloy as an intermediate product. Coarsening of the porous alloy creates the large ligaments of the upper hierarchy level. Those are then again dealloyed, which creates the fine ligaments of the lower hierarchy level. The material exhibits enhanced charge transport kinetics while maintaining a large specific surface area.

By replacing 1 at.% of Au by Pt, another similar two-step dealloying strategy is stated to fabricate hierarchical nanoporous gold with ultrafine lower hierarchy level ligaments. The Pt addition is able to pin a high Ag retention and meanwhile increases the initial Au content in Ag-Au alloy to the standard composition range (20-50 at.%). Therefore, a small volume shrinkage is expected. Using scanning electron microscope and small angle X-ray scattering, the microstructure evolution of the Pt doped Ag-Au alloy in each stage was characterized. After the first dealloying process, a nanoporous Ag-Au-Pt alloy with high Ag retention was obtained by removing part of the Ag from the master alloy as an intermediate product. With different annealing temperatures, the upper hierarchy level ligament size can be modulated freely. Those were then followed by another dealloying process to further remove the Ag which results in the formation of lower hierarchy level ligaments. The corresponding lower hierarchy level ligament size is as small as 6 nm, which is also confirmed by the small angle X-ray scattering experiments.

Acknowledgements

I would like to show my greatest acknowledgements to the following people who make this dissertation into reality. Without their support and help, I will not be able to fulfill my PhD work.

First of all, I express my deepest and sincerest acknowledgement to my supervisor Prof. Jörg Weissmüller. I am deeply grateful for the supervision and guidance during my PhD work and for the freedom I was given. He guided me into various scientific issues which are really helpful and constructive during my PhD study and will have a long-lasting impact on my future career. I really appreciate that I got such a great opportunity to work under his supervision.

I would like to thank my previous supervisor, during my master study, Prof. Zhonghua Zhang (Shandong University) who introduced me into the wonderful world of nanoporous metals when I started my master study in China.

I would like to acknowledge Dr. Haijun Jin (Institute of Metal Research, Chinese Academy of Science) for his valuable suggestions on alloy composition selection and useful discussion. Dr. Ulla Vainio (DESY) for SAXS measurements and data processing. Prof. Horst Weller and Mr. Andreas Kornowski (Hamburg University) for HRSEM imaging. Dr. Martin Ritter for EBSD measurements and data processing and Dr. Daniel Gosslar for critical reading on the draft (Technical University of Hamburg).

I would also like to thank my colleagues in the Institute of Materials Physics and Technology and Microscopy Center, Technical University of Hamburg. With their company, I spent a pleasant time in the past 4 years. It is indeed a valuable period in my whole life and I will definitely cherish those wonderful memories.

Finally, I would thank my parents Yunfeng Qi and Derong Yuan who give their endless and unselfish love on me, my wife Yanmin Huang for her understanding and support both in my career and family, and my beloved little daughter Qingqing.

Contents

List of Abbreviation

WE	Working electrode
CE	Counter electrode
RE	Reference electrode
LNE	Less noble element
MNE	More noble element
SEM	Scanning electron microscope
EDS	Energy dispersive X-ray spectroscopy
WDS	Wavelength dispersive X-ray spectroscopy
EBSD	Electron backscattering diffraction
SAXS	Small angel X-ray scattering
CV	Cyclic voltammetry
MDP	Massive dealloying potential
LPP	Loss of passivation potential
E_c	Critical dealloying potential
E_D	Dealloying potential
NPG	Nanoporous gold
N^3PG	Nested network nanoporous gold

Chapter 1

Introduction

1.1 Background and motivation

Nanostructured materials are those whose length scale at least one dimension falls in the nanometer scale, namely 1-100 nm, and include nanoparticles, nanorods and nanowires, thin films, and bulk materials made of nanoscale building blocks or consisted of nanoscale structures [1]. Due to their unique physical and chemical properties, nanomaterials received great attention toward the development of fabrication methods for creating novel functional materials at the nanometer scale. Two different nanofabrication methods are normally classified as: bottom-up and top-down [2]. Namely, bottom-up means the material is constructed from atomic or molecular precursors that are the building blocks, or self-assemble into more complex structures. By contrast, the top-down approach creates nanoscale structures by controlled removal of materials from larger or bulk solids. According to those definitions, the method of dealloying that is employed to prepare hierarchical nanoporous structure in the present thesis belongs to the top-down approach. Starting out from a bulk solid body (alloy precursor), this method can prepare a nanostructured material with a monolithic bulk shape, millimeter-sized bodies containing approximately 10^{15} nanoscale ligaments per cubic millimeter, which is interesting for fundamental research and functional applications.

The challenge here in the present thesis is how to precisely control the microstructure with a uniform distribution over a bulk sample with the desired shape and size. Especially, two levels of self-similar nanostructure will be constructed within a bulk material. The definition of bulk is that all three dimensions are at least larger than millimeter size. It has been shown that dealloying could prepare hierarchical or bimodal nanoporous structures from thin film to bulk solids [3–11]. However, previous methods reported to fabricate hierarchical or bimodal nanoporous gold with dealloying are not applicable to bulk samples or not controllable over the size of each level. In the present thesis, a new routine to create a nanoporous structure with two levels of self-similar structures from a bulk sample with precise control throughout the whole sample is to be explored. The advantage of present routine is that both levels of structure can be tuned freely.

1.1.1   General background of dealloying

Dealloying refers to a selective (chemical or electrochemical) dissolution of the less noble elements (LNE)s from an alloy and the more noble elements (MNE)s in the alloy experience a self-assembly process through surface diffusion which results in the formation of a solid/void bicontinuous structure with a random 3D distribution [12, 13]. Historically, dealloying is related in the context of corrosion, for example stress corrosion cracking (SCC) and corrosion fatigue [14] are common failures in engineering materials. Corrosion devours almost 3 % of world's GDP per year [15]. Therefore, dealloying has been intensively investigated in the context of corrosion protection for more than a century. Not until a decade ago, dealloying acquired renewed attention because it provides a facial and effective fabrication method to prepare nanoporous metals, from thin films to bulk sample, with a uniform distribution of solids/pores all over the sample. In order to dealloy an alloy, the two elements of a binary alloy should have well distinguished equilibrium potentials, allowing the LNE to dissolve away while the other remains intact. For instance, when Ag and Au form an alloy, here Ag is LNE and Au is MNE. When dissolving this alloy in HNO_3 solution, Ag dissolves away while leaving Au intact which forms the nanoporous structure.

To date, various kinds of nanoporous metals such as Au, Pt, Pd, Ag, Cu, and Ni by dealloying in aqueous solution and recently nanoporous Ti by dealloying in melt (also defined as dealloying) [6, 12, 16–23] have been successfully prepared from various master alloys including Ag-Au, Ag-Pt, Cu-Pd, Al-Ag, Al-Cu, Cu-Ti, etc. Among those master alloys, binary Ag-Au alloy is extensively studied as a prototype system for fundamental studies in understanding dealloying. Because it forms a solid solution across the whole composition range with no phase separation prior to dealloying. Furthermore, Au exhibits interesting properties such as serving as low temperature CO oxidation catalyst [24] when its size falls to nanometer range. It is well known that limited numbers of binary alloy systems form a solid solution, and most of them form intermetallic compounds which are normally hard and brittle, not ideal for mechanical processing. Despite their disadvantages in mechanical properties, intermetallic compounds offer the opportunity to prepare nanoporous metals with various porous structure. Additionally, a fast dissolution process is expected when an even less noble element like Al is in the alloy compared with Ag in the same solution. Thus, it could increase the production efficiency where only nanoporous structure is needed regardless of its integrity. Using different sample preparation approaches, the shape of nanoporous metals fabricated by dealloying can be selected based on the application requirements from thin film (sputtering) or gold leaf (nanometer range), ribbons (melt spinning) (micron range) to bulk size like millimeter cuboid (casting and processing), or even centimeter size. Nanoporous metals show plenty of interesting and potential applications such as electrochemically or chemically driven actuators [25–27], materials with switchable strength and ductility [28], varistors [29, 30] and catalysts [24, 31–33].

Traditionally, dealloying can be classified into two methods, namely, chemical and electrochemical dealloying. Chemical dealloying also refers to a free corrosion process. An alloy is immersed into a corrosive solution, normally acid or oxidative solutions which can dissolve the LNEs. In a special case, Al can be also dissolved in alkaline solutions [6, 20]. During chemical dealloying, a concentrated solution is preferred to dissolve the LNEs. With increased dealloying time the concentration will decrease as a result of replacement reactions. Since the ligament

formation is sensitive to the solution concentration, not uniform ligament distribution can be found in the chemical dealloyed samples, especially, in bulk shape sample due to the variation of concentration during dealloying. The dealoying solution concentration decreases from the outside to the inner part of the sample. Also the diffusivity of metals in concentrated solutions is fast therefore a postpone coarsening can cause the ligament size variation where the outside part is different from the inner part [34–36].

The other method is called electrochemical dealloying that a potential is applied to the sample to remove the LNEs. The advantages of this method is that a dilute concentration solution can be chosen as the electrolytes and sometimes neutral solutions also can be used for dealloying which is good from safety and green chemistry points of view. No concentration changes can be observed during electrochemical dealloying process, leaving only the potential to control the final ligament size. As the concentration of the LNE needs to be controlled and the composition across the whole sample is expected to be homogenous in the present thesis, the parameters to control the dealloying process should be as simple as possible. Therefore, electrochemical dealloying is employed in the present thesis where dealloying process can be easily controlled by changing the dealloying potential. Especially, when the dealloying potential is close to the critical dealloying potential, a high LNE retention is observed after dealloying process. The LNE retention shows a strong dependence on the dealloying potential. The high LNE retention is a prerequisite to perform a second dealloying process which is the central issue for the purpose of a two-step dealloying strategy.

Recently, a new method using metallic melt as the dealloying solutions is introduced to dealloy Cu-Ti alloy in a Mg melt to form a nanoporous Ti [22]. The Mg melt will dissolve Cu while leaving Ti which is similar as the dealloying in aqueous solution. By removing the cooled Mg in an acid, a nanoporous structure will form. The metallic melt approach is a new dealloying strategy which has a potential to prepare new nanoporous materials, especially, those can be dissolved easily in aqueous solutions.

1.1.2   Gold hierarchical structure by dealloying

Hierarchies can be observed everywhere including biological systems such as woods and bones [37], building blocks for example which make up the eiffel tower. The hierarchical order of a structure or a material may be defined as number (n) of levels of scale with recognized structure [38]. For instance, the material is viewed as a continuum for analysis of physical properties when $n = 0$; $n = 1$ (first order) may represent a latticework of continuous ribs or the atomic lattice of a crystal [38]. The blocks that build up those hierarchical structure can be divided into three catalogues: 1D fibers, 2D layers, and 3D pores.

Over the last two decades, significant interest has been devoted to the synthesis and applications of hierarchically structured porous materials. Porous materials are defined as materials that contain a porous structure consisting of interconnected pores on different length scales from micro- (< 2 nm), meso- (2-50 nm) to macropores (> 50 nm) based on IUPAC definition. Porous materials can also show a hierarchical porous structure, which means that pores of different dimensions, at least 2 dimensions, should be present in the same material.

Several approaches to render a bimodal structure or hierarchical structure by dealloying have been reported. Basically, those approaches can be divided into the following four categories:

- **Deposition** Since almost all the LNE is removed during dealloying process, if one wants to perform a second dealloying process it is reasonable to deposit a certain amount of LNE onto the surface of newly formed ligaments by electrochemical, electroless plating or nanocasting techniques. Thereafter, letting the LN and MN elements form an alloy through solid diffusion by annealing, and meanwhile the large structure is also formed. Finally, a second dealloying will remove the deposited LNE thus new pores will be created.

  Ding *et al.* [3] employed an electroless plating method by using a reduction agent to convert Ag^+ into Ag. After that the sample was annealed at a certain high temperature to allow the full diffusion of Ag and Au atoms to form an alloy, meanwhile, the ligaments started coarsening which also constructs the large ligaments. Finally, a second dealloying process will dissolve the deposited Ag which results in the formation of the small ligaments. The corresponding microstructure is shown in Figure 1.1a. A similar process was developed by Xing *et al.* [8], and the hierarchical structure is shown in Figure 1.1b. They used an electrochemical deposition process to deposit Cu onto the surface of ligaments. After that the sample is treated by annealing to tune the large ligaments. Finally, the deposit Cu was removed by another dealloying process. Owing to the slow solid diffusivity of metals at low temperature, it is hard to allow the Ag and Au to form a homogenous solid solution alloy during annealing process. Therefore, the deposition approach may not be able to produce a complete nanoporous structure after the second dealloying process, which means the fine ligaments may only form on the outer surface of large ligaments. On the contrary, a higher annealing temperature is helpful in getting a homogenous solid solution but it will lead to an extreme large ligament size.

- **Intermetallic phase** Zhang *et al.* [6, 9] found out that the initial structure of starting alloys, mainly the alloys contain intermetallic phases, can be inherited after dealloying process which generates a nanoporous structure with bimodal pore distribution, as shown in Figure 1.1 c and d. Considering that most of alloys form an intermetallic compound, this approach has a potential to prepare various combination of two different structures. However, this technique to control the distribution of microstructure during rapid solidification process restricts its shape to thin foils. A bulk sample prepared by normal solidification process can only produce a grain size of tens of microns, thus it is doubtable that whether this method can get a large channel with several hundreds of nanometer from a bulk sample.

- **Ternary alloy system** Another strategy to produce hierarchical nanoporous metals is by using a ternary alloy system. The introduction of a third element could establish the idea of dealloying step by step. That is to say, first one element is removed, then the nanoporous alloy is modulated by annealing to form the large pores, and finally the second element is removed by further dealloying while leaving the third element to form the small pores. The prerequisite for the ternary alloy system is that three elements must have different corrosion properties towards acid attacks or potential difference to dissolve the two LNEs step by step. Although several binary alloy system can form a solid solution
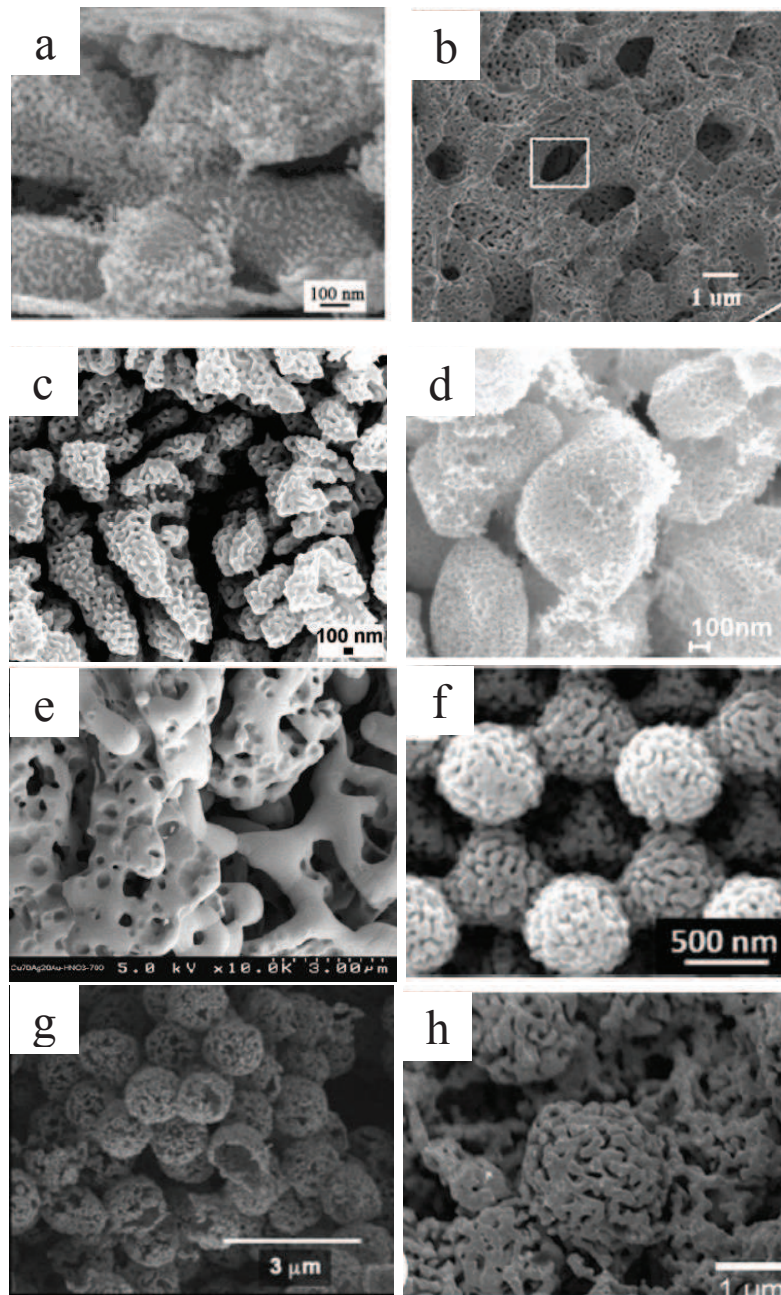
Figure 1.1: Hierarchical or bimodal nanoporous gold prepared by various methods: a), thin gold leaf by a dealloying-Ag deposition-dealloying process [3]; b), a dealloying-electrodepostion-dealloying process [8]; c), bimodal nanoporous gold by dealloying an intermetallic Al_2Au alloy [6]; d) bimodal nanoporous AuPd alloy by dealloying a ternary AlAuPd alloy[9]; e), ternary Cu-Ag-Au alloy by a dealloying-annealing-dealloying process, and note the small ligament size is more than 100 nm [4, 5]; f), an eletrodeposition and sputtering onto porous carbon template-dealloying process [10]; g) a silica or polystyrene (PS) template electrodeposited by a Ag-dealloying process [5] and h), Ag, Au and NaCl powders sintering with a compression-dealloying process [7]. Reprint with the following permissions [39].

system, as miscibility gaps tend to prevent homogenization, suitable ternary alloy systems that can be formed as uniform bulk solid solutions have yet to be identified [4, 5]. Figure 1.1 e shows the SEM image of hierarchical porous gold made from a ternary Cu-Ag-Au alloy. Note even the small ligament size is larger than 100 nm. This ligament size can not be strictly classified as nanoporous any more.

- **Template** Templates can be used to prepare hierarchical nanoporous gold. This approach requires filling the template with an alloy. Either by keeping the template after dealloying, or by reprinting the structure of the template. Reprinting means that by fully occupying the porous space of the template with the target alloy, the large pores are formed by removing the template. For the first case, the alloy is added onto the template which is kept after the hierarchical structure forms. For example, using a porous carbon as a backbone, an alloy with the target noble metal was sputtered onto the template [10]. This method can prepare a highly ordered structure distribution, as shown in Figure 1.1f. For the second case, the template is removed after the alloy formed. For instance, this approach is used to make nanoporous hollow balls, as shown in Figure 1.1g. A similar approach was reported where NaCl was mixed with Ag and Au powders, then processed by powder densification and sintering to form a bulk material [7]. When NaCl was dissolved by water, only Ag-Au alloy remained. The space where once NaCl occupied now became the large pores. The large pore distribution of this approach is, however, unpredictable because to have a homogenous mixture of the powder is not easy. Furthermore, Lee [11] used a new colloidal Bijels as the skeleton, then using nanocasting technique to fill this skeleton with Ag-Au alloys, and followed by removing the skeleton template and finally the additional Ag. The large pores in those hierarchical structures are a replica of the template. The microstructure of samples produced by templates is highly dependent on the shape of templates. To fully deposit an alloy into a bulk sample is difficult, especially, for the systems with complex porous structures.

The above mentioned methods to prepare hierarchical or bimodal nanoporous metals do not fulfill the preparation of those structures with a bulk size, namely all three dimensions should be at least larger than 1 mm. For fundamental science and practical applications, bulk materials with a nanostructure have more interesting properties can be explored than thin films. For instance, mechanical test of bulk nanoporous metal can be measured on a micron indentor compared with thin films where only nano indentor is available for this purpose [40]. In order to achieve the goal of precise control of the microstructure over a bulk sample with hierarchical structure, a new fabrication approach should be developed to meet this requirement.

1.2   Work scope and structure

The present work focuses on the fabrication of hierarchical nanoporous metallic structure with a self-similar structure by dealloying and characterizing the corresponding properties of those novel structures. A new two-step dealloying approach with two different alloy systems has been proposed in this thesis.

A brief introduction of fundamental electrochemistry is introduced in Chapter 2, since the fab-

rication and characterization are mainly using electrochemical methods. Fundamental issues about dealloying which are related to this thesis are introduced. Additionally, the background of small angle X-ray scattering is also introduced in this Chapter.

The experimental details are shown in Chapter 3 including sample preparation, characterization techniques and relevant brief introductions of those techniques.

In Chapter 4, a new strategy is developed to fabricate nested-network nanoporous gold (N^3PG) with two levels of self-similar ligaments via dealloying a dilute Ag-Au alloy from a bulk sample. Using scanning electron microscope (SEM) equipped with energy dispersive X-ray spectrum (EDS), the microstructures during different preparation stages were investigated. Cyclic voltammetry with different scan speeds was conducted in the double layer region and also gold oxidation reduction peaks were calculated to evaluate the surface area of N^3PG. Choronamperometry with step potential jump was used to study the charging kinetics in the hierarchical nanoporous gold. Nanoporous gold (NPG) with only one level pores made by $Ag_{75}Au_{25}$ alloy as reported in literature [41] was employed as a comparison to evaluate the effect of pore structure on transport in solution.

In Chapter 5, a N^3PG with ultrafine lower hierarchy level ligaments from a Pt doped Ag-Au alloy was successfully prepared by a similar two-step dealloying strategy. Normally, the residual Ag retention is less than 10 at.% in Ag-Au alloy when the Au composition is higher than 10 at.%, which is also verified in Chapter 4. Here, the results confirm that the Ag retention can be controlled to 46 at.% when only 1 at.% of Au is replaced by the Pt in the $Ag_{80}Au_{20}$ alloy. The master alloy composition was examined by energy dispersive X-ray spectroscopy (EDS) and wavelength dispersive spectroscopy (WDS) to ensure a homogenous elements distribution. Scanning electron microscope (SEM) was performed to investigate the microstructures during different preparation stages. X-ray diffraction was carried out to study the crystallographic information at each stage. Small angle X-ray scattering (SAXS) was performed to verify the existence of the ultrafine lower hierarchy level ligaments. Electron backscatter diffraction (EBSD) were used to study the crystal orientation and grain size.

Finally, the findings in the present thesis are summarized and a brief prospect on future work is given.

Chapter 2

Theoretical background

The fabrication protocols, most of characterization methods and the corrosion analysis are based on electrochemical methods. Therefore, the fundamental principles of electrochemistry will be introduced in this Chapter, which are mainly based on Bard *et al.*'s textbooks [42, 43]. Fundamental issues of dealloying that are related to the present thesis are introduced. Small angle X-ray scattering (SAXS) is used to evaluate the average lower hierarchy level ligament size, therefore basic principles of SAXS are also introduced based on literatures [44, 45].

The reuse of figures and text extracts from the textbooks [42, 43] are with Permissions of "Electrochemical Methods: Fundamentals and Applications, 2nd Edition" Copyright(2001) John Wiley and Sons and "Electrochemical Dictionary, 2nd Edition" Copyright (2012) Springer.

2.1 Fundamentals of electrochemistry

2.1.1 Standard electrode potential

The standard electrode potential, E°, stands for the equilibrium potential of an electrode under standard-state conditions, that is, in solutions with the relative activities of all components being unity and a pressure of 1 atm = 101 325 Pa at temperature T. It is measured with solutes concentration of 1 mol L^{-1}, a pressure of 1 bar = 10^5 Pa was recommended as the standard value to be used in place of standard atmosphere 1 atm. The temperature is normally at 25 °C. The hydrogen electrode is used as the reference in collections of tabulated standard potentials for aqueous solutions which is defined as 0 V. The standard electrode potential of metals that are used to prepare Ag-Au and Ag-Au-Pt alloys are listed in Table 2.1.

2.1.2 Faradaic and nonfaradaic processes

Two different types of processes can occur at electrodes. One of them is the faradaic process which involves reactions, in which charges (e.g., electrons) are transferred across the

Table 2.1: Standard electrode potential of metals used in the present thesis.

Half cell	E° [V]
$Ag^+ + e^- \rightleftharpoons Ag$	+0.7996
$Pt^{2+} + 2e^- \rightleftharpoons Pt$	+1.188
$Au^{3+} + 3e^- \rightleftharpoons Au$	+1.52

metal/solution interface where electron transfer causes oxidation or reduction happens. Such reactions are governed by Faraday's law:

$$I_F = \frac{dQ}{dt} = n_e F \frac{dN}{dt} = n_e F A v. \tag{2.1}$$

where I_F is the faradaic current, Q is the total charge, t is the time, N is the amount of reactant, n_e is the number of electrons exchanged, F is the Faraday constant, v is the reaction rate and A is the surface area.

On the contrary, these processes, with no current involved reaction occurred, are defined as non-faradaic processes. In these processes, the electrode/solution interface has no charge-transfer reactions within a range of potentials, because such reactions are thermodynamically or kinetically unfavorable. However, processes such as adsorption and desorption can occur, as a result, the structure of the electrode/solution interface can change accordingly with changing potential or solution composition.

2.1.3   Electrical double layer

When an electrode is immersed in an electrolyte solution, a specific interfacial region at the electrode/electrolyte interface is formed. To make it easier to visualize this, a solid is chosen as the electrode. At the double layer interface, charges are located between the solid and electrolyte: on the solid side, it is the surface charges (either positive or negative), which are balanced by an opposite excess of equal magnitude charges on the electrolyte side. The charges are not uniformly distributed in the electrolyte, but are expected to be concentrated at the solid interface.

The electrolyte side of the double layer is thought to be made up of three layers as shown in Figure 2.1. The closest layer to the electrode is the inner layer which contains solvent molecules and sometimes other species (ions or molecules) that are deemed to be specifically adsorbed. This inner layer is known as the compact Helmholtz, or Stern layer. The distance x_1 is the place of the electrical centers of the specifically adsorbed ions is referred to as the inner Helmholtz plane (IHP). The total charge density from specifically adsorbed ions in this inner layer is q^i (μ C cm^{-2}). The place of centers of these nearest solvated ions is called the outer Helmholtz plane (OHP) in which solvated ions can approach the surface only to a distance x_2. The diffuse layer also known as Gouy layer is a three-dimensional region of scattered ions which extends from the OHP into the bulk of the solution. The excess charge density in the diffuse layer is q^d, hence
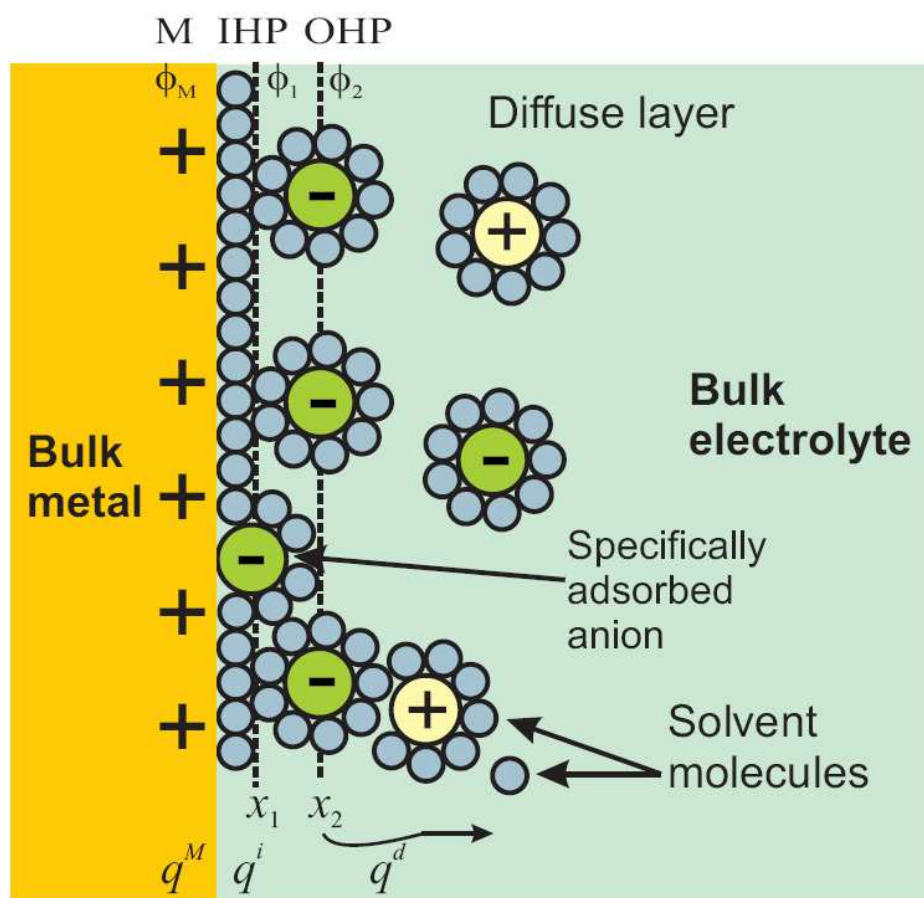
Figure 2.1: Schematic diagram of the electrical double layer region under conditions where anions are specifically adsorbed: compact and diffuse layers with solvated cations and anions in the electrolyte. M = metal surface; IHP = inner Helmholtz layer; OHP = outer Helmholtz layer. [43]

the total excess charge density on the electrolyte side of the double layer, q^S, is given by $q^S = q^i + q^d = -q^M$ where q^M is the total charge density at the metal surface.

2.1.4 Chronoamperometry method

Chronoamperometry is a technique where the current is measured as a function of time along with the application of a potential step perturbation. When a potential is applied on the sample, the faradaic current, caused by electron transfer, decays as described in the Cottrell equation:

$$I = \frac{nFAc_j^0\sqrt{D_j}}{\sqrt{\pi t}} \tag{2.2}$$

where, I = current, in unit A; n = number of electrons (to reduce/oxidize one molecule of analyte j, for example); F = Faraday constant, 96,485 C mol^{-1}; A = area of the (planar) electrode in
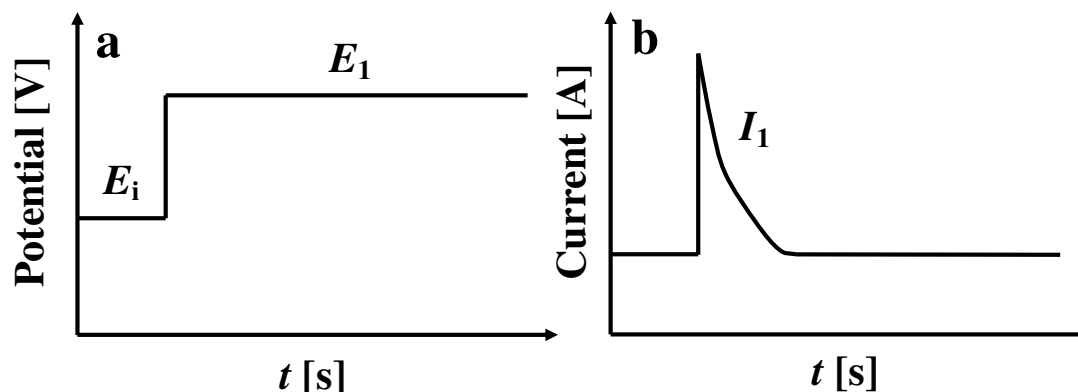
Figure 2.2: A typical waveform of the potential step (a) and the respective chronoamperometric response (b). E_i is initial value and E_1 is the potential where no reduction of O occurs or some other potential of interest.

cm^2; c_j^0 = initial concentration of the reducible analyte j in mol cm^{-3}; D_j = diffusion coefficient for species j in cm^2 s^{-1} t = time in s.

A typical step potential excitation waveform and the resulting current response *versus* time are presented in Figure 2.2. When the potential jumping from an initial state, E_i, to another value, E_1, the resulting current changes gradually and becomes stable after certain periods.

2.1.5 Cyclic voltammetry

Cyclic voltammetry (CV) is the most widely used technique for acquiring qualitative information to study electrochemical reactions. A schematic diagram of CV is shown in Figure 2.3. The voltammogram is capable of stating the potentials at which electrochemical processes occur. The working electrode is subjected to a potential sweep, where the potential varies from a start value E_i to a final value E_f then returns back to the start potential at a constant potential sweep rate. The sweep rate applied during those scans can vary from a few millivolts per second to a hundred volts per second. The current measured during this process is often normalized to the electrode surface area and referred to as the current density. The current density is then plotted against the applied potential, and the result is referred to as a cyclic voltammogram. A peak in the measured current is seen at a potential that is the characteristic of any electrode reaction taking place. The peak width and height for a particular process may depend on several parameters: the sweep rate, the electrolyte concentration and the electrode material.

The redox reaction taking place in the solution can be expressed as: $\mathbf{O}$ + ne$^-$ $\rightleftharpoons$ $\mathbf{R}$ where $\mathbf{O}$ and $\mathbf{R}$ are the oxidized and reduced forms of the redox couple, respectively. The corresponding peak positions of the redox reaction are shown in Figure 2.3.
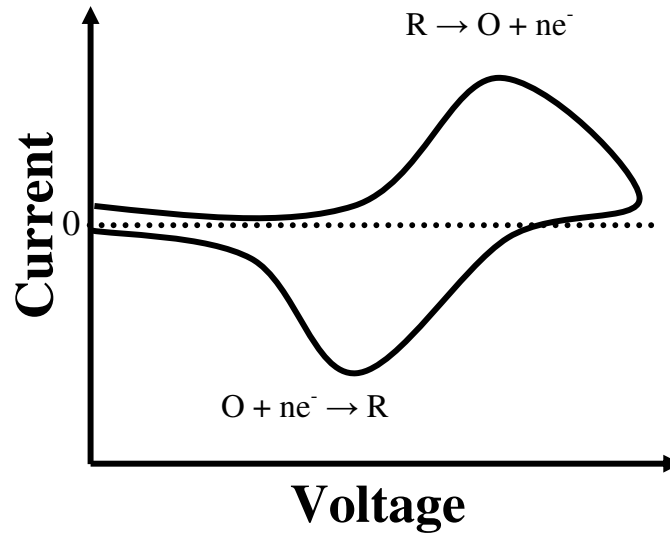
Figure 2.3: Schematic diagram of cyclic voltammetry for a reversible reaction. The positions of a redox reaction are also labeled in this Figure.

2.1.6 Tafel equation

The Tafel equation is an important equation in studies of electrode kinetics which describes the relationship between the overpotential and the faradaic current. Its empirical expression is shown in Eq.2.3:

$$\eta_{ct} = A + Blog\,|j_{ct}|$$ (2.3)

where η_{ct} is the charge transfer overpotential and j_{ct} is the charge transfer current density.

The Tafel equation is actually an approximation of the Butler-Volmer equation at sufficiently large overpotentials η. The Butler-Volmer equation under conditions where there is no effect of concentration gradient

$$j_{ct} = j_0 \left\{ exp\frac{\alpha nF}{RT}\eta_{ct} - exp - \frac{(1-\alpha)nF}{RT}\eta_{ct} \right\}$$ (2.4)

can be simplified if one of the two exponential terms becomes sufficiently small.

The dependence of the charge transfer overpotential η_{ct} on the charge transfer current density j_{ct} can be described in semilogarithmic form:
Anodic process:

$$\eta_{ct} = \frac{RT}{\alpha nF}2.3logj_0 - \frac{RT}{\alpha nF}2.3log\,|j_{ct}|$$ (2.5)

Cathodic process:

$$\eta_{ct} = \frac{RT}{(1-\alpha)nF}2.3logj_0 - \frac{RT}{(1-\alpha)nF}2.3log\,|j_{ct}| \qquad (2.6)$$

This form is equivalent to the Tafel equation. It closely resembles the general type of an Eq 2.3.

Figure 2.4 shows a schematic diagram of the Tafel plot. By measuring the linear sweep voltammetry of the electrode from cathodic to anodic direction, the current behavior dependent on the potential is obtained. Taking the logarithm of the absolute value of current density, a Tafel plot which obeys the Tafel equation is obtained.
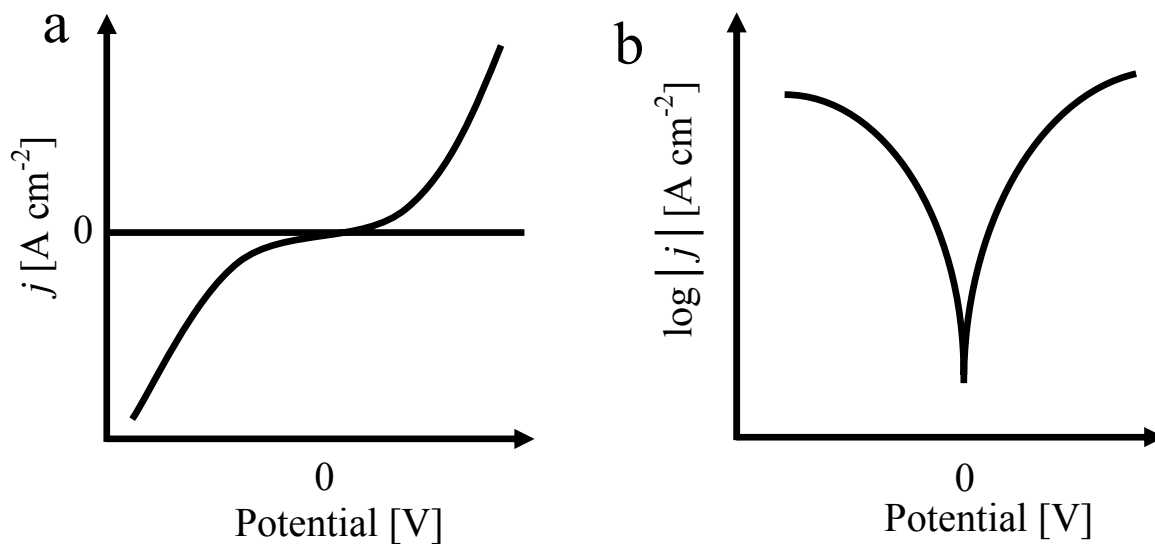
Figure 2.4: Illustration of schematic diagrams of a), linear sweep voltammetry from cathodic to anodic direction and b), the corresponding Tafel plot by log the absolute value of current density, j.

The Tafel plot is widely used in corrosion science to study the property of a sample. The Tafel plot is normally used to identify corrosion information, such as: rate of pitting, passivity and corrosion susceptibility.

2.1.7   Nernst equation

The Nernst equation describes the dependence of the equilibrium electrode potential on the composition of the contacting phases. The Nernst equation can be derived from the potential of the cell reaction $E_{cell} = \Delta G/nF$ where ΔG is the Gibbs energy change of the cell reaction, n is the charge number of the electrochemical cell reaction, and F is the Faraday constant. For the cell reaction $0 = \Sigma v_i A_i$, where A_i symbolizes the species taking part in the chemical reaction and v_i is for the respective stoichiometric numbers, the following equation can be written:

$$E_{cell} = E° - (RT/nF) \sum_i v_i ln a_i \qquad (2.7)$$

where $E° = \Delta G°/nF$ is the standard potential of the cell reaction, R is the gas constant, T is the temperature (in K), a_i is the chemical activity for the relevant species. Eq. 2.7 is also called Nernst equation. When the cell reaction is at equilibrium, i.e., $\Delta G = 0$, $E_{cell} = 0$: $E° = (RT = nF)/ln K$ where K is the equilibrium constant of the cell reaction.

For a solution containing the oxidized (O) and reduced form (R) of a redox couple $O + ne \rightleftharpoons R$ at activities a_O and a_R, respectively, the redox potential (E) is given by the Nernst equation, as follows:

$$E = E° + \frac{RT}{nF} ln \frac{a_O}{a_R} \approx E° + \frac{2.303 RT}{nF} log \frac{a_O}{a_R} \qquad (2.8)$$

where $E°$ is the standard potential of the redox couple.

2.1.8 Pourbaix diagram

Potential-pH diagrams are related to the electrochemical and corrosion behavior of any metal in water which are obtained from a compact summary of thermodynamic data. It is also known as Pourbaix diagrams and for most of the common metals those diagrams are in the database. They have the advantage of showing at specific conditions of potential and pH under which the metal either does not react (immunity) or can react to form specific oxides or complex ions; that is, Pourbaix diagrams indicate the potential-pH domain in which each species is stable.

In practice, Pourbaix diagrams are useful data for studies of corrosion, electroextraction, electroplating, hydrometallurgy, electrolysis, and electrical cells since they are electrochemical maps indicating the domain of stability of ions, oxides and hydroxides. This map provides the information of the regions measured as potential and the acidity and alkalinity of species measured as the relationship of pH. Thus, any reaction involving hydroxide OH^- ions should be written in terms of H^+ ion concentration, which in turn is converted into pH. Besides the possible reactions that may occur in an electrochemical system, a simplified Pourbaix diagram gives important areas for designing and analyzing electrochemical systems. These areas are known as corrosion, passivation, and immunity. However, the drawback of a Pourbaix diagram is that it does not include corrosion rate, which is essential in kinetic studies.

An example of a Pourbaix diagram is shown in Figure 2.5, as in this thesis Ag is the less noble element (LNE) that is dissolved during dealloying. In a Pourbaix diagram, three possible types of straight lines can be found as follows:
(1) Horizontal lines, which are for reactions involving only the electrode potential E (but not the pH),
(2) Vertical lines, which are for reactions involving only the pH (but not the electrode potential E),
(3) Slanted lines, which relate to reactions involving both the electrode potential E and the pH.

Dashed lines enclose the practical region of stability of the water solvent to oxidation or reduction.

Regions or fields between the various lines where specific chemical compounds or species are thermodynamically stable existing are also shown in Pourbaix diagrams. When the stable species are dissolved ions, the region on the Pourbaix diagram is labeled as a region of "corrosion". When the stable species are either solid oxides or solid hydroxides, the region on the Pourbaix diagram is labeled as a region of "passivity", in which the metal is protected by a surface film of an oxide or a hydroxide. When the stable species are the unreacted metal species themselves, the region is labeled as a region of "immunity". According to those classifications, the regions of Ag are listed in Table 2.2.
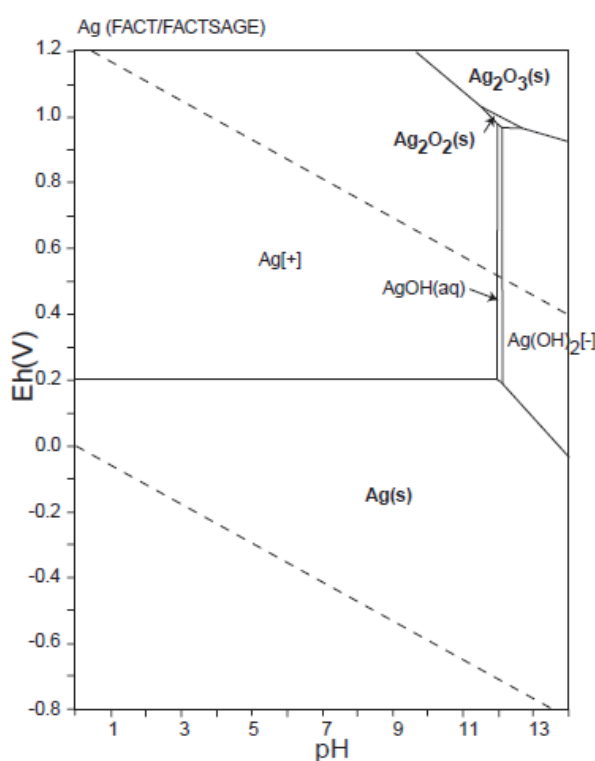

Figure 2.5: Pourbiax diagram of the system Ag-O-H. Ag = 10^{-10}, 298.15K, 10^5 Pa. Reprint with Author's permission (Dr. Naoto Takeno).

Table 2.2: Region classification based on Pourbaix diagram of Ag.

Region	Species
Corrosion	Ag^+, $Ag(OH)_2^-$
Passivity	$AgOH(aq)$, $Ag_2O_2[s]$, $Ag_2O_3[s]$
Immunity	$Ag(s)$

2.2 Fundamental issues on dealloying

2.2.1 Critical dealloying potential

Even though the fundamental issues of dealloying have been studied for years, there are still some unsolved issues, such as the ambiguity on determining the critical dealloying potential, E_C. The relationship between potential and current of a metal is determined as the polarization curve Figure 2.6a shows the scheme diagram of an alloy's polarization behavior. Figure 2.6b shows the polarization results of a series of Ag-Au alloy. It can be found that the initial dealloying potential increases with increasing Au content. When a sufficiently positive potential is applied on the alloy that can be dealloyed, the LNE dissolution occurs. The dissolution rates depend on the potential applied and also on the passivation behavior of the alloy in the solution. If the potential applied is sufficiently small, a current decay obeys the power law can be observed and a surface enrichment of noble element will passivate the surface from further dissolution. The potential value at which the passivation turns into dissolution is the E_C. Experimentally, two approaches have been discussed in literatures [46–49] on how to determine it. One approach rests on anodic polarization curves, identifying E_C with the potential at current density $j = 1$ mA cm^{-2}. The second approach uses chronoamperometry to identify the lowest potential that gives a steady corrosion current over extended periods of time. Eventually, a nanoporous structure forms all across the sample.
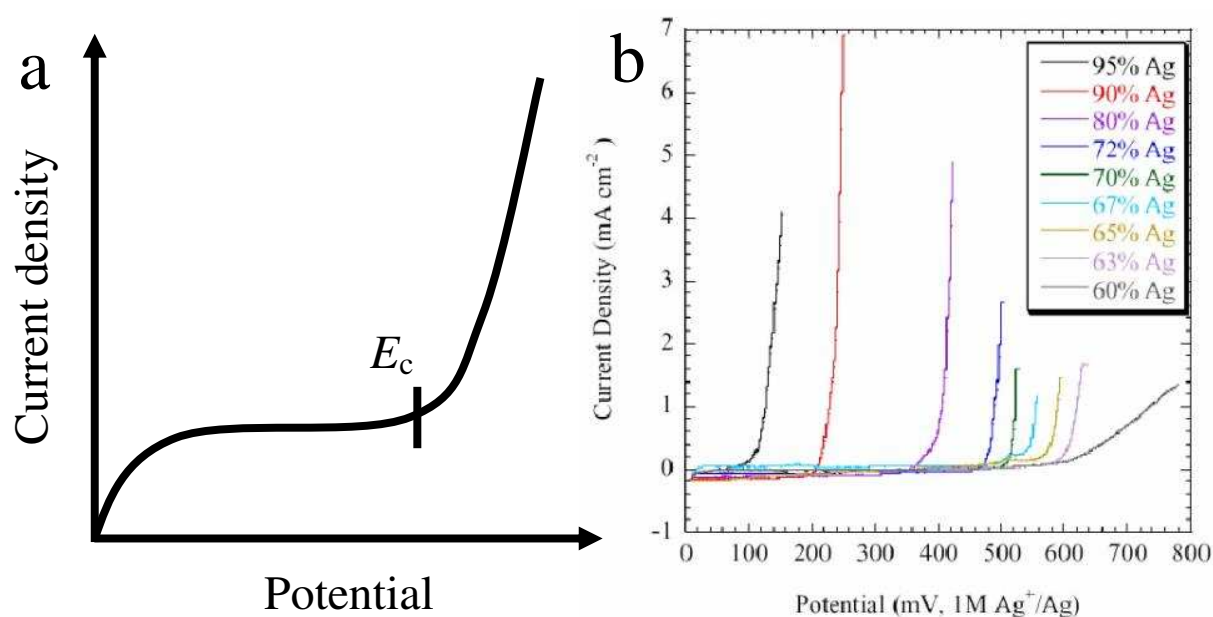
Figure 2.6: a), Schematic illustration of polarization behavior of a metal and the critical dealloying potential. b), A series of Ag-Au alloys anodic polarization curve in 1 M AgClO$_4$ + 0.1 M HClO$_4$ solution [46]. E_C is the critical dealloying potential. The Figure is adopted from Ref[46] with permissions of Copyright (2002) Electrochemical Society.

The potential difference between the two approaches may be only dozens of millivolts. From a practical point of view, the determination of E_C is not critical for making nanoporous metals by

potential-controlled dealloying, since normally several hundred millivolts overpotential above E_C is applied. Moreover, a higher overpotential equals to a fast dealloying rate which needs less dealloying time and produces a fine ligament size. There are some studies suggest that the cracks formed during dealloying are highly dependent on the dealloying potential [50]. Cracks are not desired by applications as actuators and mechanical test where a body with integrity is recommended. For other applications such as catalysts, the cracks may not be a vital issue as powder samples are preferred. However, the determination of E_C, a true dealloying potential, is of critical importance for the present thesis where the Ag retention, $x_{res,Ag}$, shows a strong dependence on E_C. As a high Ag retention is the prerequisite to perform a second dealloying. Therefore, the two methods are compared to determine E_C to decide which method reveals the true E_C.

2.2.2 Alloy composition selection for dealloying
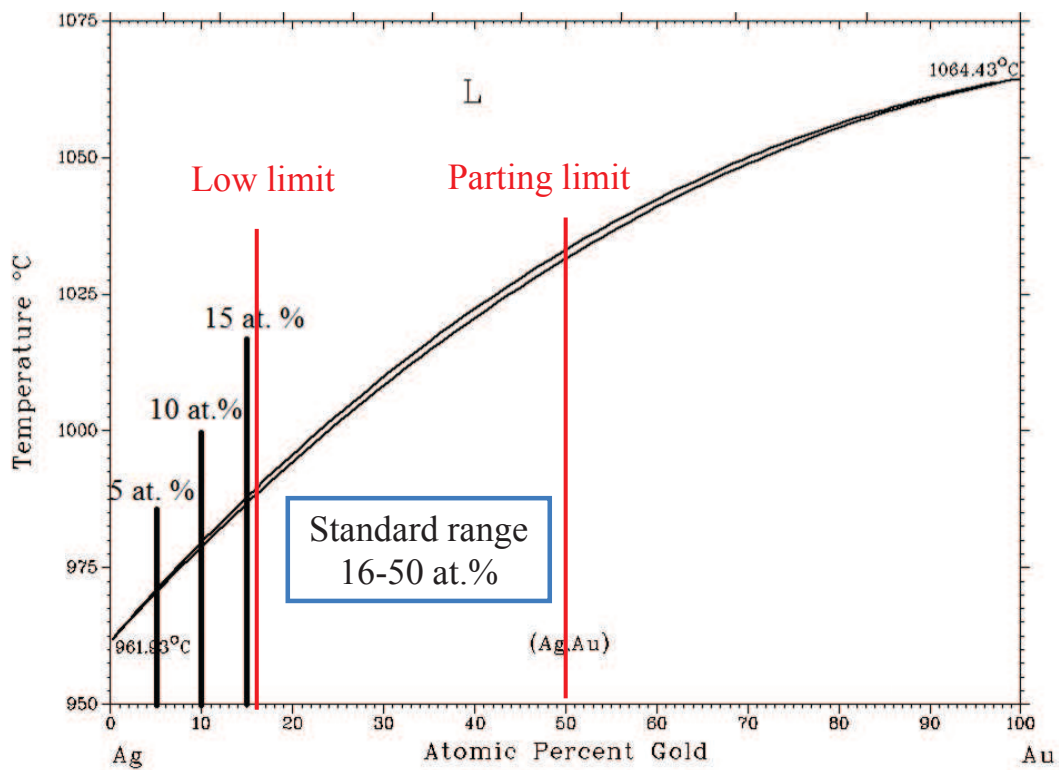
Figure 2.7: Phase diagram of the binary Ag-Au alloy. Three regions are classified based on the initial alloy composition to prepare nanoporous gold. [51, 52]. Reprinted with permission of ASM International. All rights reserved. www.asminternational.org.

Figure 2.7 shows the phase diagram of binary Ag-Au alloy, and it is divided into three different regions based on the alloy composition to prepare NPG by dealloying: dilute composition region, standard composition region, and parting limit region [48, 52].

For all the alloys that can be dealloyed, a parting limit can be observed. The parting limit is a boundary where dealloying stops at a certain depth due to the MNEs passivation when the composition of MNEs exceeds a certain value during dealloying. Typically, it is close to 50 at.% Au for Ag-Au alloy which is shown in Figure 2.7 as parting limit. The origin of parting limit is that the enrichment of MNEs will block the pathway which connects the electrolytes and LNEs. Therefore, the whole dealloying process is hindered by the passivation of MNE enriched surface and no more dissolution of LNEs. The parting limit determines the upper limit of content of MNEs that can be selected to prepare NPG by dealloying. When the Au content is higher than the parting limit, it is in the parting limit region.

The standard composition region refers to that a monolithic body of nanoporous structure can be prepared from this composition region with an empirical composition range of 16 - 50 at.% Au [52]. It is the composition region between parting limit and low limit. For Ag-Au solid solution system, crack-free NPG can be fabricated from this composition range which is an ideal candidate for mechanical test [40, 41, 53].

When the Au composition is lower than 16 at.%, the samples tend to fall into small pieces during dealloying, therefore, losing its integrity [52]. Here, this composition range is defined as the dilute composition region which is below the low limit showing in Figure 2.7. Normally, this composition range is not desirable in making NPG. Interestingly, Ateya *et al.* studied the corrosion of dilute noble metal alloys, focusing on the example of Cu-Au alloys [54, 55]. They found that an abnormal Cu retention up to 40 at.% was observed in those dilute Cu-Au alloys. If this is a universal evidence for the binary solid solution system, it is promising to control the LNE retention at a composition higher or close to the parting limit from the dilute Ag-Au alloys.

In Chapter 4, a series of Ag-Au alloys within the dilute composition range are used to examine whether a high Ag retention after dealloying can be maintained. The compositions of x_{Au} = 5, 10 and 15 are shown in Figure 2.7. If it is also working for the dilute Ag-Au alloys, it assures to maintain a high Ag retention which is a prerequisite to perform a second dealloying. The high Ag retention is the key to the successful preparation of hierarchical NPG.

In Chapter 5, a Pt doped Ag-Au alloy within the standard composition range is selected to obtain a high Ag retention. It is actually out of expectation that such a high Ag retention can be maintained starting with a Au content within the standard composition region. However, the results suggest that this Ag-Au-Pt alloy benefits from two different ways by replacing 1 at.% Au by Pt. First, starting out with a high initial Au content which means a small volume shrinkage; second, Pt has a slow surface diffusivity therefore ultrafine lower hierarchy level ligaments are created.

2.2.3   Structure control of nanoporous metals

One advantage of nanoporous metals is that their pore size can be modulated by several methods which can change the chemical/physical performances that are highly related to the surface area. Especially, chemical reaction and mass transport require different levels of porosity, namely,
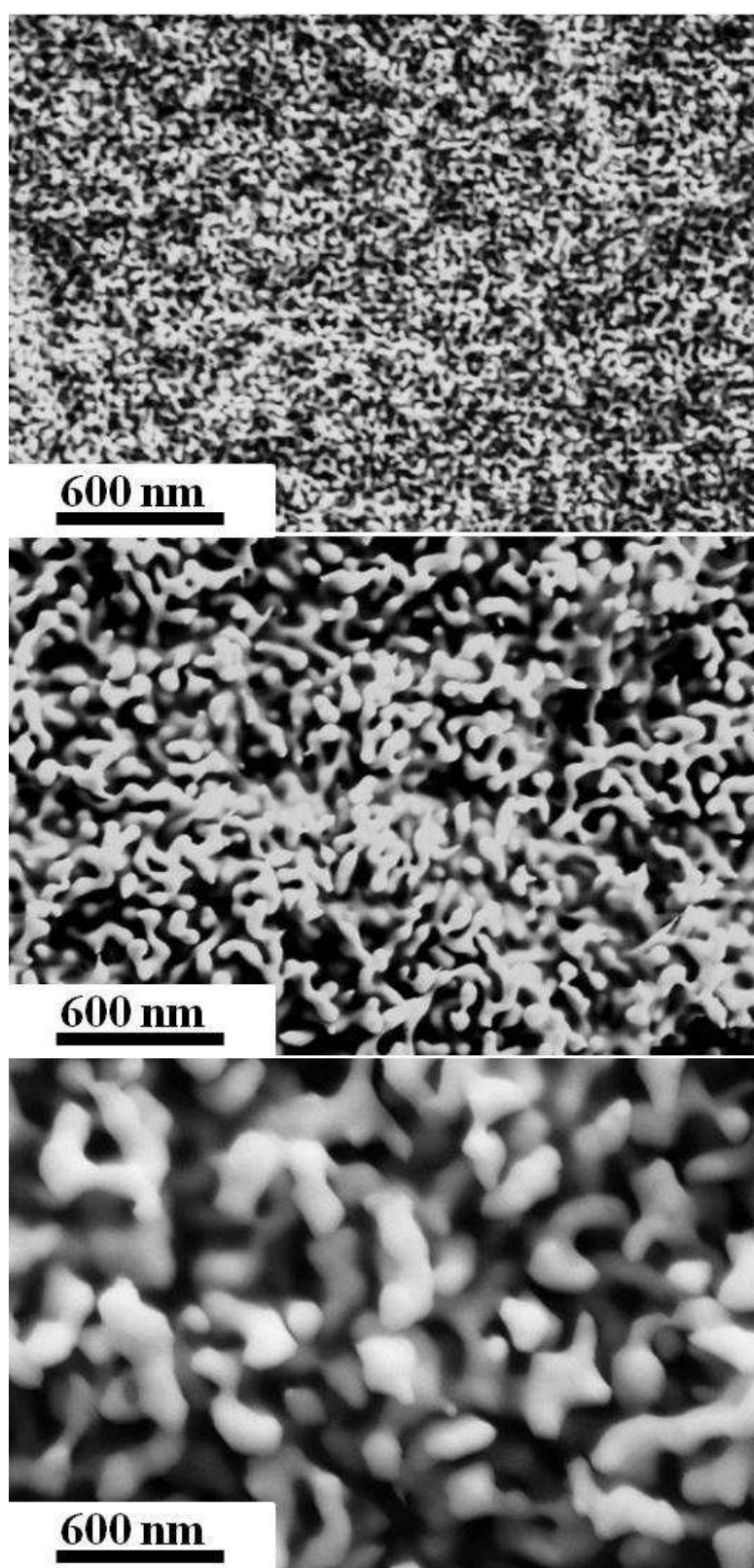
Figure 2.8: Porous size modulation by different annealing temperatures and time from top to bottom: as-dealloyed sample (15 nm), after annealing at 300 °C for 2 min (50 nm) and after annealing at 300 °C for 30 min (150 nm), respectively. Note the self-similar ligament structure after annealing process [56]. The Figure is adopted from [56] with permission of Copyright(2013) John Wiley and Sons.

small pores for functionality and large pores for mass transport. Therefore, many options can be selected to satisfy different application requirements by tailoring the pore size.

Those methods to modify the pore size can be categorized into the following five approaches:

- **Dealloying potential** Dealloying potential has a stong influence on the formation of ligaments, namely, a higher dealloying potential results in smaller ligaments and a lower dealloying potential corresponds to larger ligaments [41]. It can, however, only produce a ligament size with a length scale of less than 100 nm. Furthermore, the Ag retention after this process is normally lower than the amount that is needed to perform another dealloying process. Typically, less than 10 at.% Ag retention can be found for the standard composition range of Ag-Au alloy.

- **Post-dealloying coarsening** When the dealloying process finishes, the ligament size can be modified to a larger size by simply allowing the samples to be soaked in concentrated acid solution compared with newly formed ligaments. The reason accounts for this post-dealloying coarsening is that the diffusion at metal/electrolyte interface remains very high [35, 36]. Therefore, it has a high driving force towards a fast surface diffusion. As a result, the ligament size becomes coarsened. However, a high Ag retention cannot survive from a concentrated acid solution.

- **Temperature** Since the surface diffusion is highly related to the formation of ligaments and pores, temperature plays an important role in changing diffusivity of MNEs. Two types of methods based on temperature can be used to control the pore size: post-dealloying annealing and controlling the dealloying temperature.

  Post-dealloying means changing the pore size by annealing the samples at various temperatures after the nanoporous structure formed [56, 57]. It can increase the pore size from its initial size to microns until fully close the pores depending on the annealing temperature and time. A typical example of tuning the ligament size by annealing is shown in Figure 2.8.

  Dealloying temperature is another approach which can also affect the final ligament size. As in this approach temperature is also used to tune the ligament size while the ligament formation. It can reduce the ligament size by using a lower temperature to slow down the surface diffusivity of MNEs [21]. On the contrary, increasing the temperature during dealloying will definitely increase the ligament size, but not more than 100 nm [58]. The dealloying temperature has a similar effect as the postpone annealing process but at a relatively low temperature. For safety reasons, the temperature for dealloying should not be higher than 100 °C.

- **Effect of halogen ions** Dursun *et al.* [49] systematically studied the effect of halogen ions on the diffusivity of Au atoms during the formation of naonporous structure. Their results show that the diffusivity of Au in the presence of different halogen ions is in the following order: bare $HClO_4$ solution $<$ Cl^- $<$ Br^- $<$ I^-. The results of halogen ions suggest that the formation of nanoporous structure is strongly affected by the ions in the solution by changing the surface diffusivity. However, this method can only coarsen the ligament size to about 100 nm. Moreover, it is hard to remove the halogen ions after dealloying as a

result of strong absorption of halogen ions on Au surfaces. Therefore, it is critical for the next step applications where a clean sample surface is required.

- **Low-diffusion metal addition** The last possibility to control ligament size is to use some low-diffusion metal to partly replace the target noble metal. The low-diffusion metal will slow down the diffusivity of the target noble metal. For instance, Snyder *et al.* [59] investigated the addition of Pt to Ag-Au alloys and found that the ligament size can be as small as 5 nm. Jin *et al.* [27] also found out a similar small ligament size in their Ag-Au-Pt alloys. Furthermore, the Pt added nanoporous structure shows an excellent performance against thermal annealing which results in the ligament coarsening even at 673 K for 3 h where the ligament size is still as small as 10 nm.

It appears that the postpone annealing is the best option to control the ligament size of the upper level hierarchy structure in the present thesis. Typically, the upper level hierarchy structure can be modulated from its initial size to microns. This allows to modulate the properties of hierarchical NPG via its upper hierarchy level ligament size, for instance, different molecular sizes require different pore sizes for an optimized mass transport. The dealloying potential offers a possibility of tuning the lower hierarchy level ligament size.

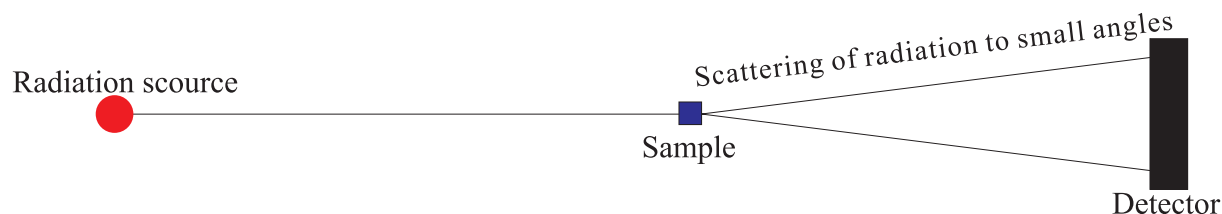## 2.3   Small angle X-ray scattering

Figure 2.9: A schematic diagram showing the scattering of radiation to small angles by a sample.

Small angle X-ray scattering (SAXS) is a powerful analytical technique to study the structure and interactions of systems with the size on the order of 10 to 1000 $\mathring{A}$ (Figure 2.9). In the diffraction experiment, the minimum size that can be measured is equivalent to $\lambda/2$, however, Bragg's law does not predict a maximum size. Bragg's Law predicts that information pertaining to nano-scale structures will be seen below 6° 2θ in the diffractometer trace ($\lambda \sim 1.0\ \mathring{A}$). By examining X-ray scattering between 0 and 6° 2θ, the information that is directly proportional to the size and shape of nanometer sized objects is measured. The characteristics of materials at these larger size scales are fundamentally different than those at atomic scales. Atomic scale structures are characterized by high degrees of order, i.e. crystals, and relatively simple and uniform building blocks, i.e. atoms. On the nanoscale, the building blocks of matter are rarely well organized and are composed of rather complex and non-uniform building blocks. The resulting features in X-ray scattering from diffraction are sharp peaks in the X-ray diffraction range and comparatively nondescript diffuse patterns in the SAXS range.

In X-ray diffraction, the atomic scattering factor, f^2, is equal to the square of the number of

electrons in an atom at low angles, n_e^2. Additionally, the intensity of scattering is known to be proportional to the number of scattering elements in the irradiated volume, N_p.

$$I \cong N_p n_e^2 \tag{2.9}$$

In small angle scattering, one can consider a generalized rule that describes the behavior of scattered intensity as a function of Bragg size "r" that is observed at a given scattering angle 2θ, where $r = 1/q$ and where q is $4\pi \sin(\theta)/\lambda$. All scattering patterns in the small angle regime reflect a decay of intensity in q and can be described by considering that the decreasing size reduces the number of electrons in a particle in a given volume, while the number of particles increases with 1/volume. The scattered intensity (Eq. 2.9) is proportional to the decay of the particle volume with size. This analysis implies that the definition of a particle (r) does not necessarily reflect a real domain, but reflects the size, r, of a scattering element that could be a component of a physical domain.

2.3.1 Porod's law

Porod's law is concerned with wave numbers q that are small compared to the scale of the usual Bragg diffraction; typically $q \lesssim 1$ nm^{-1}. In this range, the sample must not be described at an atomistic level; one rather uses a continuum description in terms of an electron density or a neutron scattering length density. In a system composed of distinct mesoscopic particles, all small angle scattering can be understood as arising from surfaces or interfaces.

If the interface is flat, then Porod's law predicts the scattering intensity

$$I(q) \sim S q^{-4} \tag{2.10}$$

where S is the surface area of the particles, which can be experimentally determined in this way. The power law q^{-4} corresponds to the factor $1/sin^4\theta$ in Fresnel equations of reflection [45].

2.3.2 q-range

A schematic diagram of three different q-range includes high q domain, intermediary zone and low q domain is shown in Figure 2.10. q is called length of the scattering vector or momentum transfer. The dimension of q is one over length (e.g. [1/nm]) and this explains that a scattering pattern is usually called "the structure in reciprocal space", and the corresponding particles have a structure in real space which can be measured in units of length (e.g. [nm]).

High q domain: The window is very small: there is a contrast only at the interface between the two media. This domain, called the Porod's region, gives information about the surfaces.

Intermediary zone: The window is of the order of the elementary bricks in the systems. The form factor *P(q)* can be measured (size, shape and internal structure of one particle).

Low q domain: When the observation window is very large, the structural order can be obtained: it is the so-called structure factor *S(q)*, which allows to calculate the interactions in the system.
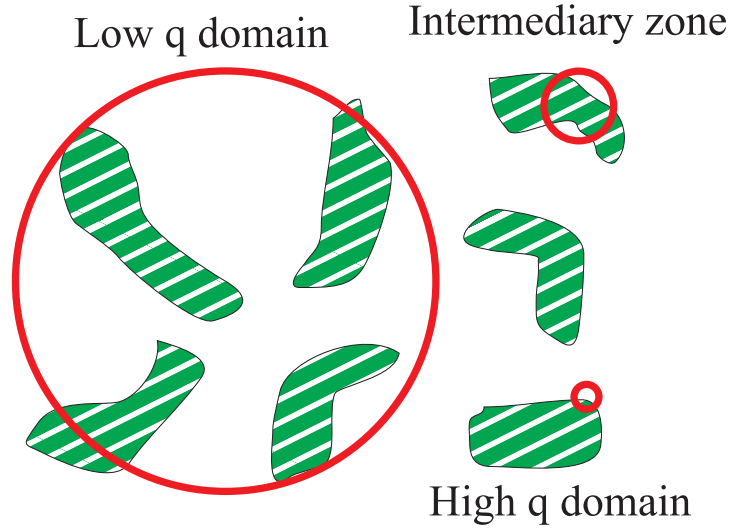
Figure 2.10: A schematic diagram showing the high q domain, intermediary zone and low q domain, respectively.

2.3.3   Debye formula

The Debye formula is:

$$I(q) = \int \int \int dV \cdot \widetilde{\rho}^2(r) \cdot e^{-iqr} \tag{2.11}$$

where I is the scattered intensity, V is the volume, r is the distance between volume elements of average scattering density ρ while the scattering vector q.

The well-defined structural length scale of nanoscale network structures made by dealloying is known to give rise to an interference peak in small angle scattering [60, 61] that is reminiscent of interference in spinodally decomposed fluids [62]. A simple estimate for the characteristic spacing between ligaments in the network may be obtained from the Debye formula for the interference between randomly oriented pairs of scatterers with a characteristic distance d. The formula links d to the value, $q_{\max}$, of q at the maximum of the interference peak via [63]

$$q_{\max} \approx 1.23\frac{2\pi}{d} \,. \tag{2.12}$$

The q-range thus translates into a resolution of structure sizes in the order of 4 - 100 nm. X-ray transparent samples were obtained by crushing the nanoporous bodies through gentle grinding in a mortar, followed by spreading of the powder on adhesive tape. The nonuniform thickness of the samples prevented a meaningful reduction of the scattering intensities to absolute units.

Chapter 3

Experimental procedures

3.1 Dealloying setup

The dealloying setup used in the present thesis is illustrated by a schematic diagram as shown in Figure 3.1. A typical three electrode system was employed to perform dealloying. The working electrode (WE) was the sample, an inert Pt plate with a larger surface area than WE served as the counter electrode (CE), and a home-made Ag/AgCl reference electrode (RE) as illustrated later was isolated by a Luggin capillary to ensure a stable potential output. Other electrochemical measurements were performed in a similar three electrode system but with different cells.

3.1.1 Reference electrode

The homemade RE was used for the electrochemical dealloying experiment. It is called pseudo Ag/AgCl RE. The pseudo Ag/AgCl RE was prepared by oxidizing a Ag wire (0.5 mm diameter, Ag 99.99%, ChemPUR) at 0.9 V for about 120 s in 1 M (mol L^{-1}) aqueous HCl (ACS grade, Merck) solution until a layer of AgCl formed on the Ag surface. Another Ag wire was served as both RE and CE while making those REs. The potential of this pseudo Ag/AgCl RE with respect to the standard Ag/AgCl in saturated KCl solution is 0.33 V measured in 1 M HClO$_4$, and, therefore, its potential *versus* Standard Hydrogen Electrode (SHE) is 0.53 V positive. Table 3.1 shows the comparison of commercial REs and this home-made RE compared relative to SHE [42].

Table 3.1: Equilibrium potentials (E) of the commercial reference electrodes and the homemade Ag/AgCl reference electrode compared relative to Standard Hydrogen Electrode (SHE).

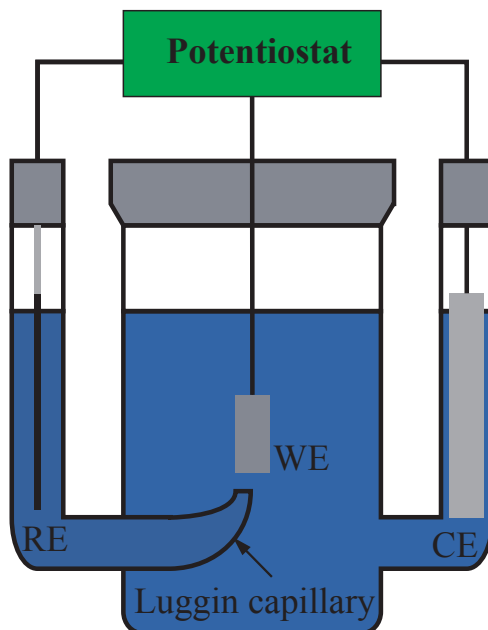| Reference electrode	E *vs.* SHE [V]
Ag/AgCl, KCl (sat'd)	0.197
Hg/Hg$_2$Cl$_2$, KCl (sat'd) (SCE)	0.241
Ag/AgCl, 1 M HClO$_4$	0.53

Figure 3.1: Scheme diagram of a typical three-electrode dealloying setup through potential controlled dealloying process. The working electrode (WE) is the sample, an inert Pt plate serves as the counter electrode (CE), and the home-made Ag/AgCl is used as the reference electrode (RE).

3.1.2   Luggin capillary for dealloying process

Due to the electrical resistance of the electrolyte, an ohmic voltage drop occurs between the working and reference electrodes, and the shorter the distance between the two electrodes the smaller the voltage drop is. To keep the distance between the WE and RE as small as possible, the RE is connected to the WE via a Luggin capillary. This is of great importance for all measurements under current flow. Another advantage of this Luggin capillary is that the RE potential is well guaranteed by separating the RE and working electrolytes where the dissolved metal ions cannot affect the RE potential with Luggin capillary. Especially, in the present thesis, the dealloying potential shows a huge impact on controlling Ag retention during dealloying process. Thus, a steady potential output is of vital importance in the present thesis. The Luggin capillary is shown in schematic diagram Figure 3.1.

The tip of the Luggin capillary near the WE is open to the test solution. RE senses the solution potential at this open tip. Note that the Luggin tip is significantly smaller than the RE itself.

3.2   Sample preparation

For the dilute Ag-Au alloys, master alloys of the following composition $Ag_{(100-x)}Au_x$ with $x =$ 5, 10 and 15 were arc melted (Compact arc melter MAM-1, Edmund Bühler, as shown in Figure

Figure 3.2: Mini arc melter used to prepare alloys in present thesis.

3.2) from Ag (99.95%, ChemPUR) and Au (99.995%, ChemPUR) under argon atmosphere (with a purity of 99.9995%) for 3-5 times to ensure the alloy was fully melted. Afterwards the alloy was homogenized at 850 °C for more than 100 h in evacuated and sealed quartz tubes in a resistance furnace. The whole chamber was evacuated for 5 min and then filled with argon. The above process was repeated at least 3-5 times in order to have a clean atmosphere before igniting the arc. A titanium ball, used as a getter to remove oxygen during alloy preparation, was in the chamber. Before melting the metals, the titanium ball was melted at least for 5 s in order to remove the residual oxygen as the vacuum pump only offers a medium vacuum condition ($\sim 10^{-2}$ mbar). The samples were cooled down spontaneously on a water flowed copper plate when the arc was turned off. The ingots were then rolled to 1 mm in thickness by a rolling machine, and subsequently cut into cuboids with a dimension of $1 \times 1 \times 2$ mm^3 using a diamond wire saw (Well diamond saw, Model 3032) and annealed for recovery in vacuum furnace (MILA-5000, ULVAC) at 650 °C for 3 h to remove the residual stress during the rolling and cutting process. The vacuum condition of this vacuum furnace is $\sim 10^{-6}$ mbar. The vacuum condition for the following experiments using this vacuum furnace is the same.

Samples for anodic polarization measurements were rolled into a sheet form with a thickness of 0.2 mm. After that, the sheet was punched on a home-made stamping machine to form a disc shape with a diameter of 3 mm. All the disc samples were grinded on one side with a sequence of 800, 1000, 2500 and 4000 mesh abrasive grinding papers, respectively. Then, the sample was annealed at 650 °C for 3 h to remove the effect of residual stress introduced by grinding. A copper wire was connected with the ungrinded surface by conductive silver paint. A nail painting (Lacomit, Agar Scientific), which is normally used for insulating the metal from electrolytes, was employed to cover the ungrinded surface and the part of copper wire which will

be immersed into the electrolytes, leaving only the grinded surface exposes to the electrolytes. Therefore, the surface area that is exposed to electrolytes is fixed during measurements.

Master alloys of the following composition $Ag_{80}Au_{19}Pt_1$ were prepared from pure Ag (99.995%, ChemPUR), Au (99.995%, ChemPUR) and Pt (99.95%, ChemPUR) with the same melting apparatus as the dilute Ag-Au alloys. In order to ensure a homogenous elements distribution, the alloy was prepared as the following sequences: first Au and Pt were melted as an intermediate alloy during which the Au was gradually added to Pt, followed by mixing this intermediate alloy with Ag. After each melting process, the samples were flipped over, and this process was repeated for 5-8 times to ensure the alloy was fully melted and homogenized at 950 ^{o}C for more than 100 h in evacuated and sealed quartz tubes. When the annealing process was completed, the ingots were directly quenched in water to prevent phase segregation. After that, the ingots were directly cut into cuboids $1 \times 1 \times 2$ mm^3 in size using a diamond wire saw.

The sample for wavelength dispersive X-Ray spectroscopy (WDS) measurement was cut from the ingot and then was supported with epoxy. The epoxy was hardened for one day in order to let the epoxy gives the best mechanical support. The sample was polished by abrasive grinding papers with the following sequence 800, 1000, 2500 and 4000 meshes. Each step was performed at least 20 s until the last grinding trace was removed. After each step, the sample was cleaned with flushing distilled water and immersed in water in an ultrasonic bath for 2 min to remove the particles from the abrasive grinding paper and make sure that no large particle residuals from this step which may damage the surface can be transferred to the next step. The sample was examined under a light microscopy (Lecia) after each grinding process in order to examine the grinding results. The grinding machine was also cleaned with flushing water and clean paper every time when changing the abrasive grinding paper.

3.3   Dealloying protocol and structure modulation

All the electrolytes were prepared by ultrapure water (18 M Ω cm, Arium 611, Sartorius). In order to ensure accurate measurements, in some cases a standard cleaning solution (5 volume parts concentrated 98 % H_2SO_4 (ACS grade, Merck) + 1 part 30% H_2O_2 (ACS grade, Merck)) was used to clean the glassware by immersing it for 24 hours and then rinsed thoroughly with ultrapure water to remove adsorbed ions.

For the dilute Ag-Au alloy, cuboid samples were dealloyed at room temperature (~ 20 ^{o}C) under potential control in 1 M $HClO_4$ (Superpur, Merck). Dealloying experiments were performed through a typical three electrode system via a potentiostat (Autolab, PGSTAT100N). The Pt plate CE with sufficient surface area shared the cell (volume 300 ml) with the WE. Potentials were measured relative to Ag/AgCl RE in the same solution. All potentials in this thesis are specified relative to the home-made Ag/AgCl RE. In order to find out the relationship between the Ag retention and the dealloying potential, the disc samples with a thickness of 0.2 mm and a diameter of 3 mm were dealloyed at 300, 400, 500 and 600 mV, respectively. The critical dealloying potential (see Chapter 2) was determined by potential holding experiments based on the results obtained from the anodic polarization measurements. Samples used to prepare hierarchical nanoporous gold (NPG) were dealloyed at 300 mV for the first dealloying step.

Samples after dealloying were rinsed in ultrapure water for several times, then with alcohol and finally dried in a glove box. The dealloying process was carried out until the current decays to a value of less than 10 μA. Coarsening treatments used a vacuum furnace at 300 °C for 3 h with 10^{-6} mbar. The second dealloying process was performed with the same setup at 750 mV until the current decays to a value of less than 10 μA. The resulting hierarchical nanoporous gold is designated as nested-network nanoporous gold (N^3PG). Reference samples of conventional NPG used a master alloy of $Ag_{75}Au_{25}$ were prepared as in Ref [64], dealloying potential of 750 mV for the single dealloying step, and otherwise identical procedures as above.

For Ag-Au-Pt alloys, other dealloying setups were identical as the dilute Ag-Au alloys. Based on the results of the dilute Ag-Au alloys, the critical dealloying potential of the Ag-Au-Pt alloys was determined directly by potential holding experiments. Dealloying potential of 650 mV was performed at the first dealloying step until the current value reaches less than 10 μA.

The nanoporous Ag-Au-Pt alloy samples were annealed at 400, 500 and 600 °C for 0.5 h with the same vacuum furnace which generates the upper hierarchy level ligaments with different sizes. After the annealing process, a second dealloying step was performed at 1000 mV until the current decays to a value of less than 10 μA to create the lower hierarchy level ligaments.

Both the sample preparation steps of the dilute Ag-Au and Ag-Au-Pt alloys are shown in Table 3.2.

Table 3.2: Sample preparation protocols.

Sample	First step dealloying	Annealing parameter	Second step dealloying
$Ag_{95}Au_5$	300 mV	300 °C, 3 h	750 mV
$Ag_{80}Au_{19}Pt_1$	650 mV	400 or 500 °C, 0.5 h	1000 mV

3.4 Electrochemical measurements

Anodic polarization curves are normally measured to evaluate the corrosion behavior of metals in electrolytes. This method was used to determine the critical dealloying potential when the value of current density reaches 1 mA cm^{-2}. One research work [46] has shown that the scanning rate shows a strong dependence on scan rate. Faster scanning rate will shift the anodic polarization curve to more negative potentials. Normally, a low scan rate less than 5 mV s^{-1} was employed in several studies in determining the critical dealloying potential[49, 65–67]. In this thesis, anodic polarization curves were measured by positive-going potential sweeps at a slow scan rate of $\dot{E}$ = 1 mV s^{-1}. Those measurements were performed in the dealloying solution consistently.

In order to evaluate the specific surface area, CV was performed in the double layer region starts from 0 to 0.6 V at a series of scan rates from 10 to 100 mV s^{-1} with an increment of 10 mV in 1 M $HClO_4$. The double layer region is recognized by the CVs of NPG and N^3PG which will be introduced later.

The specific surface area was characterized by the capacitance ratio method [68], using 1 M $HClO_4$ as the electrolyte and a NPG sample as the counter electrode. The capacitance value, c, of Au in the double-layer region of the voltammogram was taken as $c_{dl} = 40 \ \mu F \ cm^{-2}$ [69]. With m the sample mass, the current, I, was taken to obey $I = c_{dl}\alpha_m m\dot{E}$ which, all other quantities being known, can be solved for the mass-specific surface area, α_m.

As a comparison, the electrochemically active surface area is also evaluated by calculation of the reduction peak of Au oxides. The specific charge equivalent of 220 mC cm^{-2} [70] was used for converting the charge passed during the gold oxide reduction to a total surface area, which was then divided by the mass of the NPG electrode in order to obtain a specific surface area per unit mass. CVs of NPG and N^3PG which start from 0 to 1 V with a scan rate of 1 mV s^{-1} were measured.

In orders to evaluate the charge transport within NPG and N^3PG, chronoamperometry studies of electrochemical charging kinetics were performed. It started with a 600 s hold at the initial potential, E_0, here 0 V, before the jump to the final potential, E_f. E_f starts from 0 V with an increment of 50 mV to 1 V.

3.5   Structure characterization

3.5.1   X-ray diffraction

X-ray diffraction is a relatively fast and indestructive technique to study the material's structure information. X-ray diffraction can also be used to determine strain, preferred orientation, crystallographic structure, and grain size of crystalline materials.

The relationship between X-ray and crystal can be described by the famous simple equation known as Bragg's law:

$$n\lambda = 2d\sin\theta \tag{3.1}$$

where n is an integer (whole number), λ is the wavelength of the incident beam, d is the spacing between the planes in the atomic lattice, and θ is the angle between the incident ray and the scattering planes.

The present X-ray diffraction experiments were performed on a powder diffractometer with $CuK\alpha$ radiation, $\lambda = 0.15406$ nm, 40 kV, 40 mA (Detector: LYNXEYE XE, Bruker) using a convergent beam. The scan range was from 2θ 30 to 80° with a scan time period of 4 h using a θ-θ mode. The sample after each process was directly measured without crush it into powders.

3.5.2   Small angle X-ray scattering

Small angle X-ray scattering (SAXS) used a Bruker NanoStar setup with a sealed Cu microanode ($I\mu S$, wavelength $\lambda = 0.1542$ nm) and an area detector (performed by Dr. Ulla Vainio,

DESY). With the magnitude of the scattering vector defined as $q = 4\pi sin\theta/\lambda$, where θ is half of the scattering angle, the resolved q-range was $0.07 \text{ nm}^{-1} \leq q \leq 2 \text{ nm}^{-1}$. Scattering angles were calibrated by means of a silver behenate standard.

3.5.3 Scanning electron microscopy

The scanning electron microscopy (SEM) is a powerful tool that is used to image the sample surface by scanning it with a high-energy beam of electrons in a raster scan pattern. The electrons interact with the atoms that make up the sample producing signals that contain information about the sample's surface topography and composition.

Several types of signals produced by electron beams include secondary electrons, back scattered electrons, characteristic X-rays, and transmitted electrons. In principle, the SEM can achieve a high resolution of 1 to 5 nm, certainly operational parameters play an important part on getting a high resolution image. SEM images also offers a very large depth of field which yields a characteristic three-dimensional appearance that is helpful for understanding the surface structure of a sample.

In this thesis, structural characterization used scanning electron microscopes (SEM, Zeiss, Supra55 and Leo 1530) at an accelerating voltage of 10-20 kV for the morphologies of different stages. The working distance was 4-8 mm which is depending on the image mode that is used. For the SEM used in the present thesis, the theoretical resolution is 1 nm. In order to get a high resolution image, the in-lens detector was preferred in the present thesis. For high resolution SEM images of Pt doped samples, it was performed on a Leo 1550 (performed by Mr. Andreas Kornowski, Hamburg University) at an accelerating voltage of 20 kV. Similarly, a in-lens detector was used. The samples were broken from the middle then they were transferred onto the Al stub covered with carbon tape. In order to increase the electron conductivity, silver paint was used to cover the edges of the nanoporous samples. Before each measurement, the samples for SEM was placed in a glove box for at least one overnight to remove the absorbed species from the nanoporous structure.

3.5.4 Energy dispersive X-ray spectroscopy

The fundamental principle of energy dispersive X-ray spectroscopy (EDS) is that each element has a unique atomic structure which excites independent characteristic X-rays of an individual element. Those characteristic X-rays contain different energies which are used to identify the corresponding elements.

EDS is capable of distinguishing elements from atomic number (Z) 4 (Be) to 92 (U), though it is difficult for some instruments to detect 'light' elements (Z < 10). Qualitative analysis is fairly straightforward due to the simplicity of X-ray spectra. Quantitative analysis (determination of the concentrations of the elements present in the sample) is based on the integration of characteristic peaks with respect to the calibrated standards.

The composition analysis was performed in the SEM (Leo 1530 and Zeiss Supra VP55) using energy dispersive X-ray spectroscopy (EDS, Oxford INCA, Aztec) to determine the residual Ag retention in each stage. The working distance was 8 mm with an accelerating voltage of 20 kV. Before performing measurements, a standard reference sample was measured to calibrate the system, here a cobalt reference was used. The accuracy of quantitative EDS analysis in theory could reach a value of ~ 0.1 %.

3.5.5   Wavelength dispersive X-Ray spectroscopy

Wavelength dispersive X-Ray spectroscopy (WDS) also uses the characteristic X-rays generated by elements to enable quantitative analysis (down to trace element levels) to be measured at spot sizes as small as a few micrometers. Unlike EDS which produces a broad spectrum of wavelengths or energies simultaneously, WDS reads or counts only the X-rays of a single wavelength at a time with respect to a special crystal. WDS is extremely good in distinguish the nearby elements where characteristic energies are overlapped which makes the result of quantitative analysis is deviated from its true values [71].

In order to check the master alloy composition of the $Ag_{80}Au_{19}Pt_1$ alloy, a WDS measurement was performed on the Zeiss VP 55 SEM, due to the reason that Au and Pt are neighboring elements which cause a overlap peak at $L\alpha$ thus hard to distinguish one from the other. Moreover, the Pt content is relatively low compared with the other two elements. The working distance was 8.5 mm with an accelerating voltage of 20 kV. Before performing the WDS measurements, the system was calibrated with pure Ag, Au and Pt elements standards.

3.5.6   Electron backscatter diffraction

Electron backscatter diffraction (EBSD) is a useful technique to study crystal structure, crystal orientation and grain boundary. The electron beam from the SEM gun hits the tilted sample by 70° which generates diffracted electrons. The diffracted electrons which form Kikuchi pattern (also known as electron backscatter patterns, EBSP) are collected on a fluorescent screen. A software is used to process and index those EBSPs.

The inverse pole figure map is an orientation imaging map filled with pixels color-coded according to the orientation illustrated in the unit triangle of the inverse pole figure. An inverse pole figure of a certain direction describes the position of this sample direction with respect to the crystal reference frame.

In the present thesis, N^3PG obtained by dealloying the Pt doped Ag-Au alloy was examined by the EBSD technique to study whether the grain size remains the same as in the master alloy. The EBSD system is attached to a SEM (Zeiss, VP55). The working software is Aztec, Oxford. The EBSD measurements were carried out by Dr. Martin Ritter (TUHH). The measurements were conducted with a working distance of 15 mm and an accelerating voltage of 20 kV. The sample for EBSD measurements was imbedded in an epoxy resin. Using a Ultramicrotome (EM UC7, Leica), the sample was first trimmed to a size of ~ 0.4 × 0.3 mm^2 and then cut until the

sample surface was exposed. After that the sample was cut with the following cutting step size of 500, 100, and 20 nm, respectively. Several cuts were made for one cutting step until at least two times distance of last step was removed. After all the cutting process, the bulk block was used for EBSD measurements.

Chapter 4

Nested-network nanoporous gold from dilute Ag-Au alloy

The results of this Chapter have been partly published in the following article "Z. Qi, J. Weissmüller, ACS Nano, 2013, 7, 5948-5954". The reuse of figure and text is from Ref. [72] with permission of Copyright (2013) American Chemical Society.

In this chapter, a dilute Ag-Au alloy is used to fabricate nanoporous gold (NPG) with two levels of self-similar hierarchical nanoporous structures. As stated in the Chapter 2, the Ag-Au alloy composition can be divided into three categories based on the fabrication of NPG: the dilute composition, the standard composition and the parting limit. Inspired by the dilute Cu-Au alloy where a high Cu retention was found after dealloying [54], the dilute Ag-Au alloy was investigated in this Chapter to clarify whether a high Ag retention can be maintained after dealloying, as Ag-Au alloys also form a solid solution. The results suggest that a high Ag retention can be kept in the dealloyed NPG, therefore, it is promising that a hierarchical structure can be generated from this special master alloy. Subsequently, the strategy of annealing was adopted to coarsen the structure to form the first level of ligaments and pores (large). Thereafter, dealloying again to form the second level of ligaments and pores (small). The specific surface area of nested-network nanoporous gold (N^3PG) was estimated by two electrochemical methods. A simple charging experiment was carried out in the double layer region to evaluate the charging kinetics of N^3PG. As a comparison, NPG with similar ligament size as lower hierarchy level ligament was also prepared.

4.1 Experimental results

4.1.1 Determination of critical dealloying potential

In order to determine a proper method to measure the critical dealloying potential (see Chapter 2), E_C, the existing methods were examined as there is still a controversy on determining E_C. Furthermore, when the dealloying potential is close to the true E_C it is expected to control more

Ag retention. Two approaches towards E_C have been discussed in the literature [46–49]. One approach rests on the anodic polarization curves, identifying E_C with the potential at current density $j = 1$ mA cm^{-2}. The second approach uses chronoamperometry to identify the lowest potential that gives a steady corrosion current over extended periods of time. That potential marks the transition from passivation to the formation of a bicontinuous porous structure. For ease of distinction the first measure for E_C is designated as the "massive dealloying potential" (MDP) and the second as "loss of passivation potential" (LPP) in the present thesis.
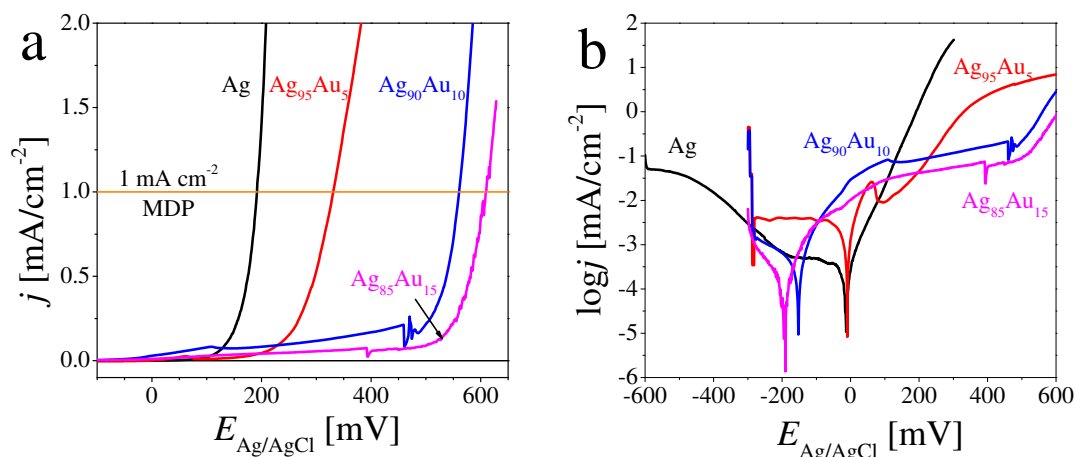

Figure 4.1: Signatures of the corrosion behavior of pure Ag and of the master alloys Ag$_{95}$Au$_5$, Ag$_{90}$Au$_{10}$ and Ag$_{85}$Au$_{15}$ in 1 M HClO$_4$. a), Current/potential graphs at a scan rate of 1 mV s^{-1}. and b), the corresponding Tafel plots.

First, the corrosion behavior of the master alloys Ag$_{1-x}$Au$_x$ with the Au fraction extending from a more concentrated alloy with $x_{Au} = 0.25$ down to the dilute $x_{Au} = 0.05$, focusing first on E_C, is inspected. Figure 4.1a shows the linear sweep voltammetry measurement for all three alloy compositions and pure Ag in 1 M HClO$_4$ solution at a slow scan speed 1 mV s^{-1}. It can be found that the dealloying potential increases with increasing Au content which is consistent with previous study [46]. The corresponding Tafel plots are shown in Figure 4.1b. From those Tafel plots, the Nernst potential can be clearly observed as the turning points in the curves. The Nernst potential shifts to the negative direction. When x_{Au} is higher than 10 at.%, a passivation region started from the Nernst potential to the dealloying potential is well distinguished. On the contrary, pure Ag and Ag$_{95}$Au$_5$ alloy show a nearly similar corrosion behavior in which no passivation behavior can be found. This is in good agreement with Ateya's observations that the dilute Cu-Au alloys show a similar corrosion behavior as pure Cu [54, 55].

Figure 4.2a shows the two measures of E_C for the master alloys with $x_{Au} = 5$, 10 and 15%. The scan rate has an important influence on the linear sweep voltammetry curve [46]. The results are relative to the Nernst potential of pure Ag measured from the Tafel plot in Figure 4.1. A fast scan rate will shift the corresponding anodic polarization curves towards the negative direction. Even though a quite slow scan rate was chosen for recording the linear sweep voltammetry curves of those alloys, it is apparent that the two definitions yield considerably different values of E_C. This applies especially to the alloys with more Au, where the difference exceeds 100
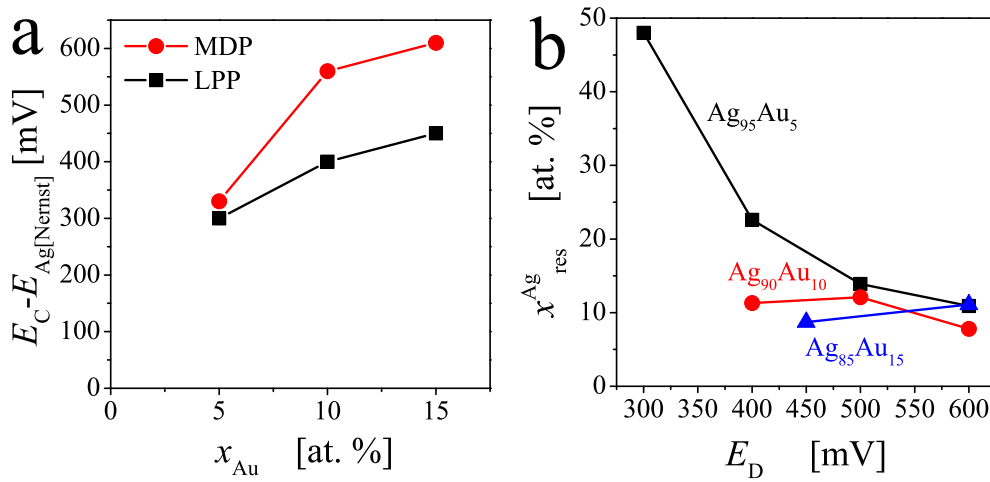
Figure 4.2: a), Overpotential (relative to the Nernst potential, E_{Nernst} of pure Ag) at the loss of passivation (LPP) and at the massive dealloying (MDP) *versus* the Au fraction, x_{Au}, in the master alloy. b), Residual Ag content, $x_{\text{Ag,res}}$, *versus* dealloying potential, E_{D}, for dealloyed material made from the master alloys alloys indicated.

mV. Clearly, the LPP is much close to the true E_{C}. Therefore, the present E_{C} is determined by LPP.

Samples were dealloyed at various potentials, E_{D}, above their LPP, and Figure 4.2b shows the resulting Ag retention, $x_{\text{Ag,res}}$ plotted *versus* E_{D}. The master alloys with 10 and 15 at.% Au yield $x_{\text{Ag,res}} \approx 10$ at.%, similar to previous reports for Cu-Au [73] and too small for the intended two-step dealloying strategy. By contrast, $x_{\text{Ag,res}}$ in the $Ag_{95}Au_5$ increases from 11 to 48 at.% when E_{D} is decreased from 600 to 300 mV. This brings the composition of the nanoporous Au-Ag alloy close to the parting limit. The other conditions of the samples have a very small silver content, below the parting limit, and therefore it is doubtable that whether they can be dealloyed again. Additionally, this again suggests that the LPP is a better method to determine the true E_{C} as the LNE content is highly dependent on E_{D} where 100 mV difference will make the two-step dealloying strategy become impossible.

4.1.2 Current decay of the $Ag_{95}Au_5$ alloy at different potentials

The current decay results of the $Ag_{95}Au_5$ alloy at E_{D} of 300, 400, 500, and 600 mV, respectively, are shown in Figure 4.3a. It can be found that the initial dealloying current value increases with increasing deallloying potential, which is in good agreement with the linear sweep voltammetry curve of $Ag_{95}Au_5$ alloy (Figure 4.1a) where a higher potential represents a higher current value. The current maintains a steady decay from the initial dealloying stage, then a knee of the curve can be observed where a rapid current decay happens. Samples dealloyed at 300 mV have the lowest dealloying current and thus the longest time period which is 10 times more than that is needed for samples dealloyed at 400 mV to finish the whole dealloying process. It should be noted that samples dealloyed at 400 mV have already fallen into several pieces. The higher the
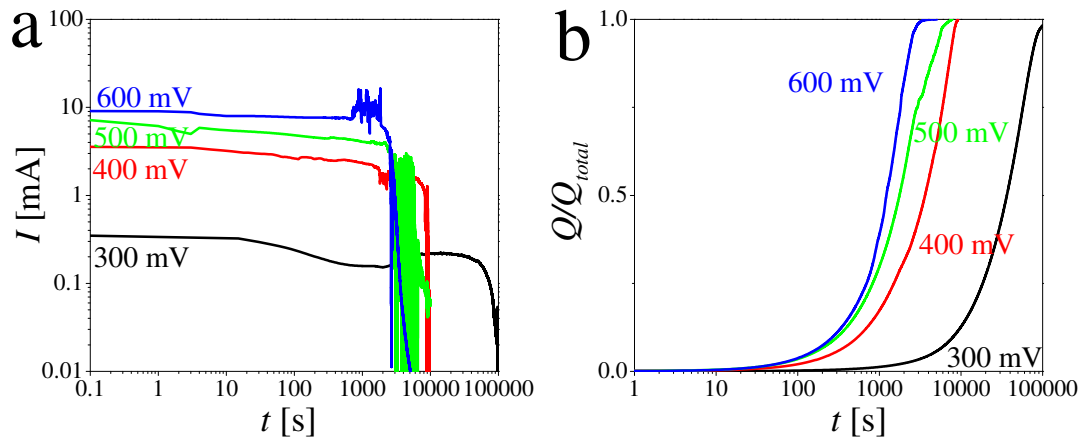
Figure 4.3: a), Current decay experiments of $Ag_{95}Au_5$ alloy at various potentials (300, 400, 500 and 600 mV) and b), the corresponding charge accumulation during this experiment by integration of current *versus* time.

E_D is the more pieces will form. This is consistent with previous study [52] where the dilute Ag-Au alloys cannot form a monolithic sample after dealloying. Artymowicz *et al.* [74] argue that dealloying a $Ag_{95}Au_5$ alloy will lead to a well-adhered, albeit highly cracked structure. This is true for samples dealloyed at above 400 mV. However, the sample dealloyed at 300 mV maintains its integrity as shown in the inset of Figure 4.4b.

Based on the current decay curves, the total charge transferred during dealloying can be calculated by the current decay results. The charge accumulated compared with total charge that is transferred during Ag dissolution at different potentials of $Ag_{95}Au_5$ alloy is shown in Figure 4.3b. Using these total charge results, they can be converted into the amount of Ag atoms that is dissolved during the dealloying process. By dividing the amount of Ag atoms by total time, an estimated mean Ag dissolution rate (average) can be obtained. The corresponding results are listed in Table 4.1. Ag dissolution rates of samples dealloyed at above 400 mV are two orders of magnitude than that of samples dealloyed at 300 mV. A similar finding is found in dealloying of the Ag-Au alloy from the standard composition range [41]. That is a higher E_D will result in a finer ligament size albeit more cracks formed and *vice versa*.

Table 4.1: Mean Ag dissolution rate based on current decay experiments. N_{Ag} represents the mean Ag dissolution rate.

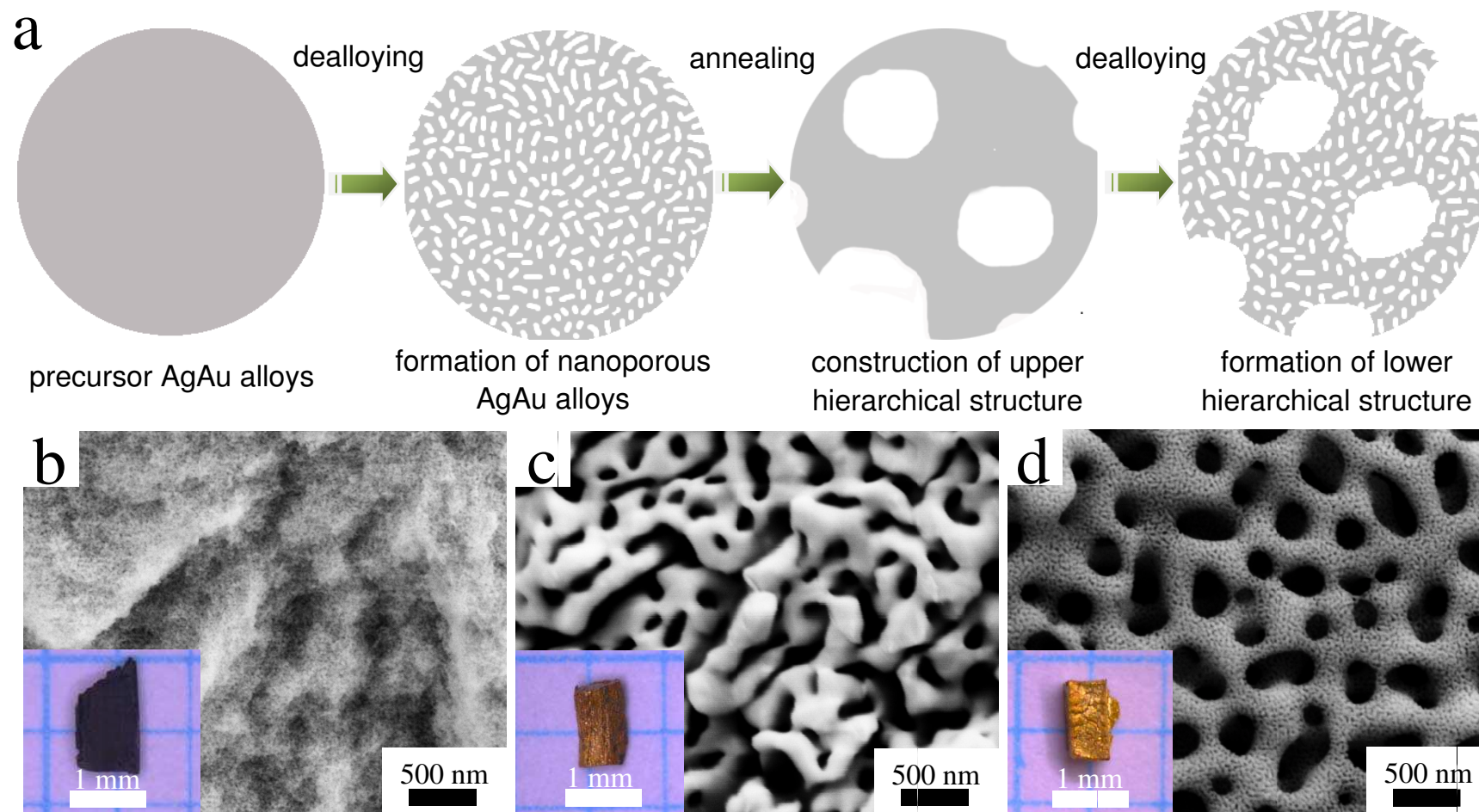| Dealloying potential [mV]	Ag dissolution rate [N_{Ag} s^{-1}]
300	7.8×10^{14}
400	1.0×10^{16}
500	1.2×10^{16}
600	2.6×10^{16}

Figure 4.4: Top: a), Schematic diagram illustrating the strategy towards the hierarchical nanoporous gold. Bottom: exemplary scanning electron micrographs showing the microstructure evolution after each consecutive step, starting out with a $Ag_{95}Au_5$ master alloy dealloyed at 300 mV vs Ag/AgCl. b), Fracture surface of the as-dealloyed nanoporous $Au_{52}Ag_{48}$ sample after first step. c), Fracture surface of the annealed sample showing coarsening. d), Hierarchical structure formed after the second dealloying step.

4.1.3   Formation of nested-network nanoporous gold

The schematic diagram of the present strategy to fabricate hierarchical NPG with self-similar structure is shown in Figure 4.4a. The central issue regarding the present strategy is to obtain a high Ag retention in NPG after the first dealloying step. Once it is possible to get this intermediate nanoporous Ag-Au alloy, the ligaments of the upper hierarchy level can be tuned by annealing. Thereafter, a second dealloying will create the ligaments of the lower hierarchy level within the ligaments of the upper hierarchy level. Figures 4.4 b)-d) display the overview SEM images of the microstructure in the corresponding stages of preparation with same magnification. The as-dealloyed material (Figure 4.4b) is a nanoporous $Au_{52}Ag_{48}$ alloy with a ligament size of ~ 16 nm which is clearly shown in Figure 4.5. Upon annealing at 300 °C for 3 h, this microstructure coarsens to reach a ligament size of 200 nm. Figure 4.4c) displays this state, in which the upper hierarchy level is already expressed. In order to form the lower hierarchy level, the coarsened porous Ag-Au alloy is subjected to the second dealloying step. Here E_D = 750 mV was chosen which is similar to what is typically used for dealloying massive Ag-Au. Figure 4.4d) shows the resulting, final microstructure. As can be seen in Figure 4.4d, the microstructure after the second corrosion step consists of a fine network of nanoscale ligaments nested within each ligament of the coarser network structure.
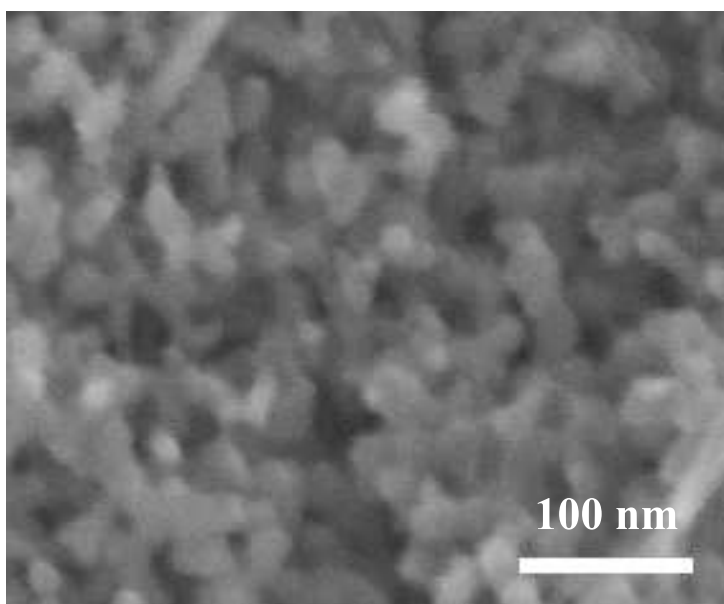

Figure 4.5: SEM image showing the cross section view of the nanoporous $Au_{52}Ag_{48}$ alloy at a higher magnification.

Figure 4.6a shows details of the final microstructure. The two hierarchy levels of the nested-network structure of the solid are reflected in a complementary and geometrically similar pore-channel structure, with ~ 200 nm size upper hierarchy channels and ~ 15 nm size lower hierarchy channels.

The reference to the nested-network structure as 'hierarchical' is suggested by the presence of the two well-defined length scales. As is visible in Figure 4.6, the sizes of the two levels are
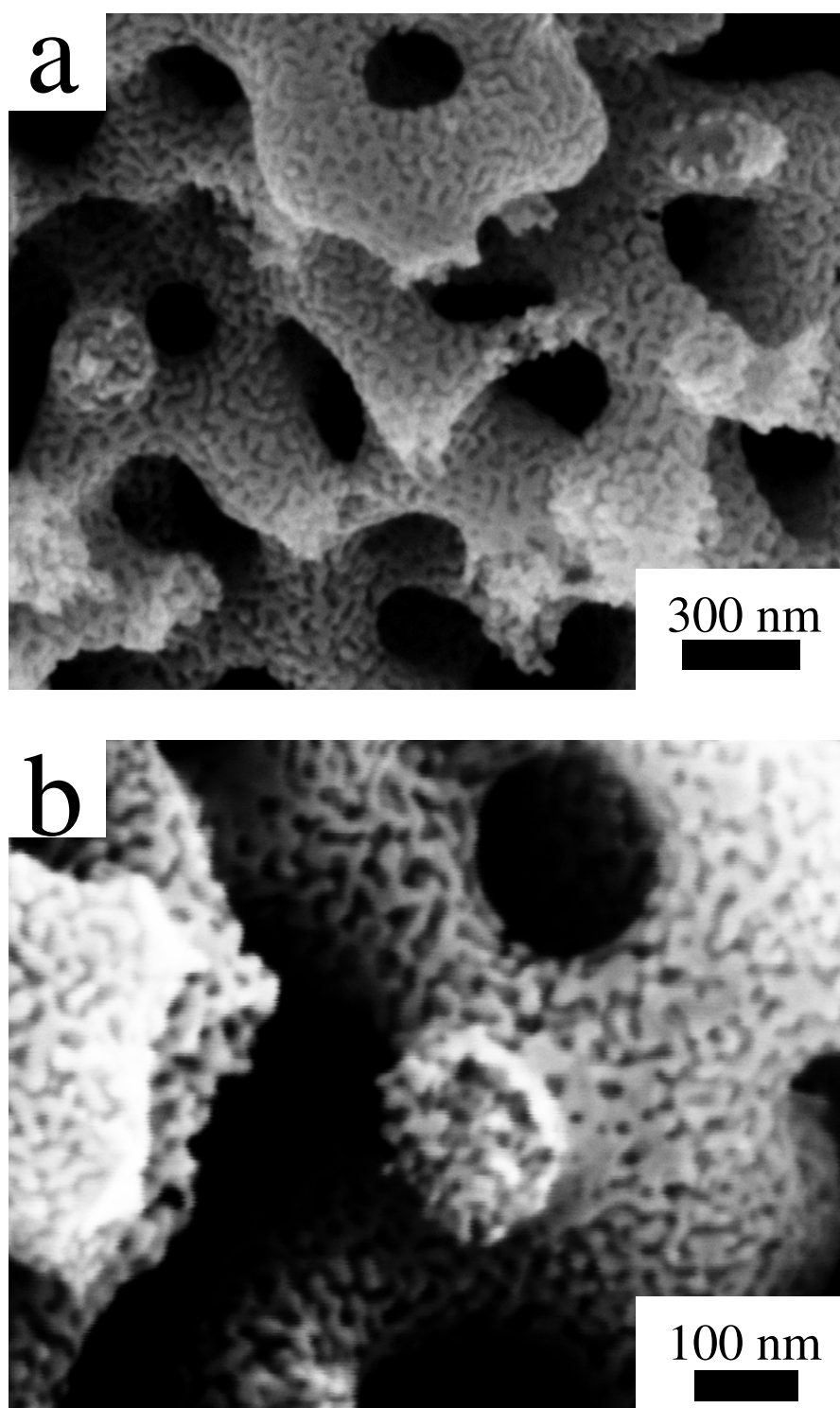
Figure 4.6: Scanning electron micrographs showing the microstructure of hierarchical nanoporous gold. Graph b) highlights the cross section of an upper hierarchy level ligament.

not only well separated, but the topology on each of the two levels is geometrically similar to that on the other. A cross section view of an upper hierarchy level ligament is highlighted in Figure 4.6b. The micrograph confirms that the entire ligament is porous and composed of lower hierarchy level ligaments.
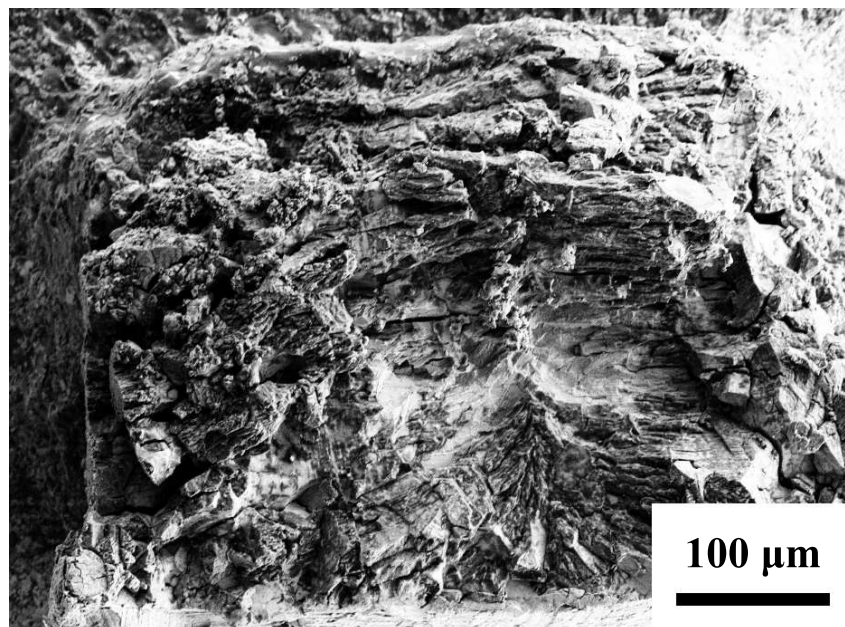

Figure 4.7: SEM image showing the cross section view of an overview of the nanoporous $Au_{52}Ag_{48}$ alloy.

Optical micrographs of the macroscopic sample geometry in different preparation stages are shown in the insets of Figure 4.4b-d. A large volume shrinkage which leads to a considerable stress while dealloying is found. The initial dimension of the sample is $1 \times 1 \times 2$ mm^3. Comparing sample dimensions before and after the corrosion, a volume contraction to ~ 39 % of the original size and the development of cracks at the scale of 20-100 μm during the first dealloying step are found. Figure 4.7 shows the overview of a sample after the first dealloying process. Cracks are already formed during this process, especially, at the outer part of the sample. More clear cracks formed when this sample was treated after annealing process as shown in Figure 4.8. A granular structure can be found with a size of tens of microns after annealing. The following dealloying preparation step does not give rise to noticeable extra shrinkage or cracking. As can be seen in Figure 4.4d, the final nested-network structure takes the form of a monolithic bulk sample.

The advantage of the present strategy is to modulate the size of the upper hierarchy level ligaments by annealing. Here, another annealing temperature at 500 °C was chosen to produce a larger upper hierarchy level ligament size. The corresponding SEM images are shown in Figure 4.9. It can be seen that the sample after annealing at 500 °C for 3 h, the upper hierarchy level ligament size increases to ~ 400 nm, which is in good agreement with that a higher annealing temperature means a more coarsened ligament size [56, 57]. Similar to the sample annealed at 300 °C, two well distinguished levels of structures can be clearly observed. The present results suggest that the upper hierarchy level ligament size can be modulated by tuning annealing
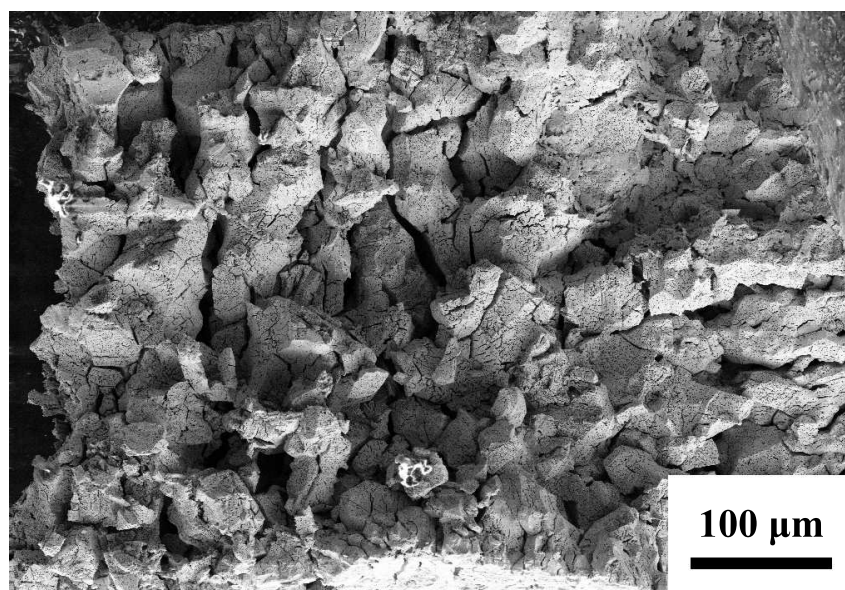
Figure 4.8: SEM image showing the cross section view of an overview of the nanoporous $Au_{52}Ag_{48}$ alloy after annealing at 300 °C for 0.5 h. Note the cracks along the granular structure.

temperature.

4.1.4 Surface area evaluation of nanoporous structure

In recent studies on evaluating surface area of NPG [70, 75, 76], the reduction peak of gold oxidation was employed to calculate electrochemically active surface area (EASA). As a comparison for the capacitance measurement, a CV study on both NPG and N³PG was performed as shown in Figure 4.10. Two regions can be identified from those CVs: the double layer region (from 0 to 0.6 V) and gold oxidation/reduction region (from 0.6 to 1 V). According to the gold reduction peak, EASAs are $S_{NPG} = 6.0 \pm 0.1\,m^2\,g^{-1}$ and $S_{N^3PG} = 3.9 \pm 0.1\,m^2\,g^{-1}$. The EASA in the present work is comparable to above studies [70, 75, 76].

The net surface area of the N³PG samples can be measured by means of the electrochemical capacitance ratio method [68]. Figure 4.11a and b show cyclic voltammograms (CVs) in the double layer region at different scan rates. The corresponding averages of the capacitive currents, I_c, at the center of the CVs are shown in Figure 4.11 c and d. The current values scale with the potential scan rate, implying that the mass-specific surface area, α_m, may be determined as introduced in Chapter 3. For N³PG $\alpha_m = 3.0 \pm 0.1\,m^2\,g^{-1}$ is found. By means of comparison, a NPG sample made by conventional one step dealloying was selected. This sample is nanoporous, but lacks the upper hierarchy level. Figure 4 shows the results, here implying $\alpha_m = 4.0 \pm 0.1\,m^2\,g^{-1}$.

The results of capacitance measurements are quite consistent with the EASA results. They have a similar magnitude, except the value of EASA is about 1.5 times larger than that of capacitance measurements.
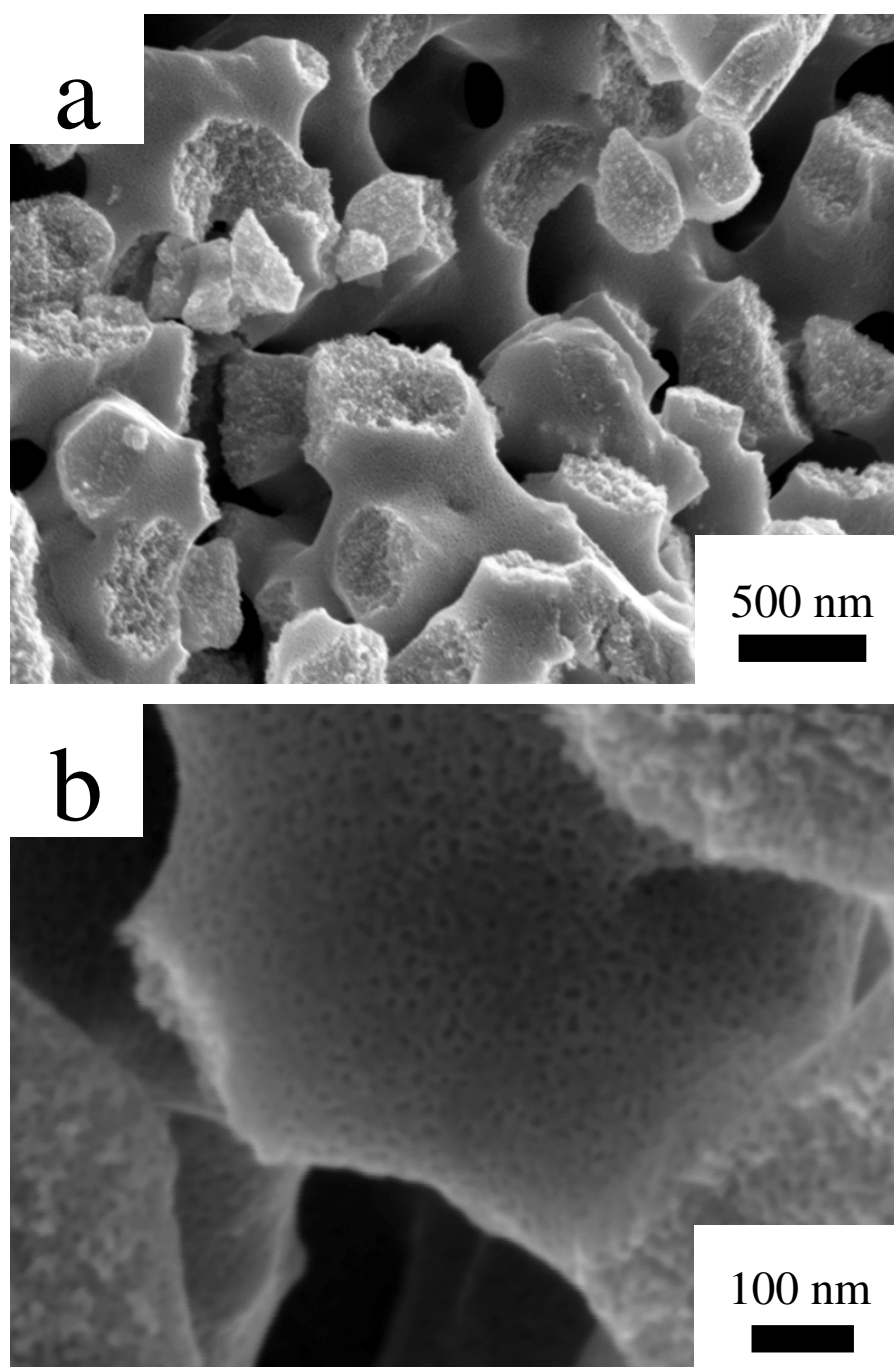
Figure 4.9: Scanning electron micrographs showing the microstructure of hierarchical nanoporous gold annealed at 500 °C for 3 h then dealloyed at 750 mV. Graphs in a), at a low magnification and b), at a high magnification.
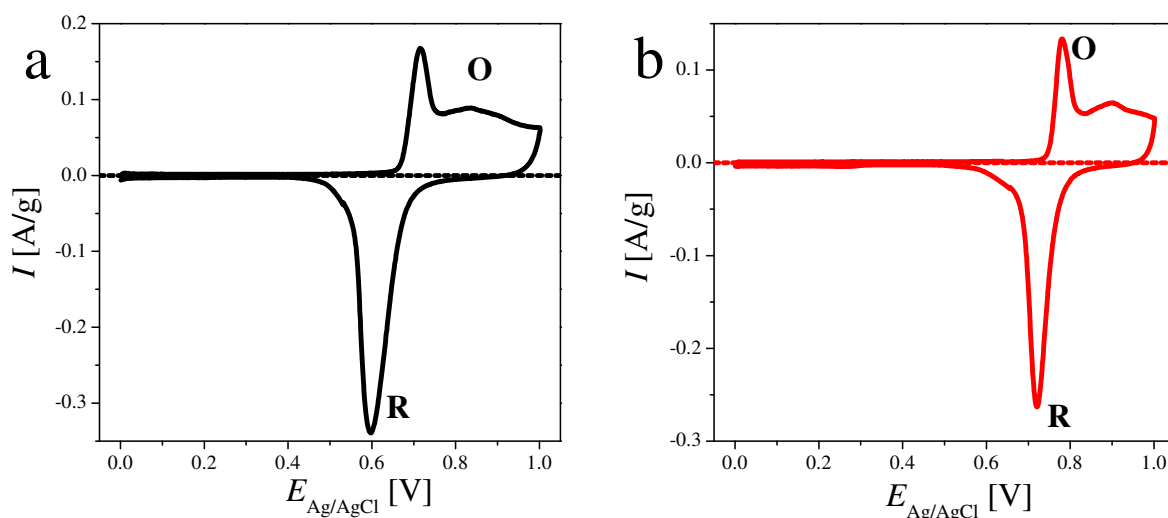
Figure 4.10: Cyclic voltammetry of a), NPG and b), N^3PG measured from 0 to 1 V at a scan rate of 1 mV s^{-1}. The peak **O** represents the Au oxidation peak and peak **R** represents the Au reduction peak. The Au oxidation region starts from ~ 0.6 V and below that potential is the double layer region.

4.1.5 Charging kinetics comparison

As a test for the impact of the structural hierarchy on the ion transport kinetics in the pore space a series of step potential measurements were performed, comparing the kinetics of double layer charging in N^3PG and in a NPG reference sample. The capacitance ratio data show that these samples had comparable specific surface area values and, therefore, comparable ligament size (at the lower hierarchy level in the case of N^3PG). The sample size of N^3PG in this experiment was $0.7 \times 0.7 \times 1.6$ mm^3, while that of NPG was $0.9 \times 0.9 \times 1.8$ mm^3. Figures 4.12a and b show current transients after potential steps. On the log-linear scale of the figures, the graphs of current *versus* time exhibit points of inflection. Studies of transport kinetics of planar gold electrode surfaces show closely similar behavior (yet with much shorter time constants); the inflection points there separate regimes in which the diffusion of different ions controls the kinetics [77]. Irrespective of these details, the data show that under all conditions the current decay in N^3PG is strongly accelerated as compared to that in NPG. For instance, when the potential is stepped within the double layer region, the current in N^3PG has decayed to half of its initial value in less than 2 ms. By contrast, NPG reaches the same state after about 0.3 s. In the oxygen adsorption region, N^3PG needs ~ 1 s for the current to reach its final inflection point, while NPG needs ~ 100 s. In other words, the charging kinetics in N^3PG is faster, by factors of 150 in the double layer region and 100 in the oxygen species adsorption region, compared with NPG. The double layer region and oxygen adsorption region can be seen in Figure 4.10. Before the rise of an oxidation peak it is double layer region. On the contrary, it is oxygen adsorption region. As a particularly simple process, Figure 4.12c inspects a potential jump from 0.1 to 0.2 V, within the double layer region, in detail. The graphs represent chronoamperometry results of current *versus* time for N^3PG and NPG. The time, $t_{\frac{1}{2}}$, for I to decay to 50 % of its initial value is a measure for the transport kinetics, and for the switching rate in applications as an
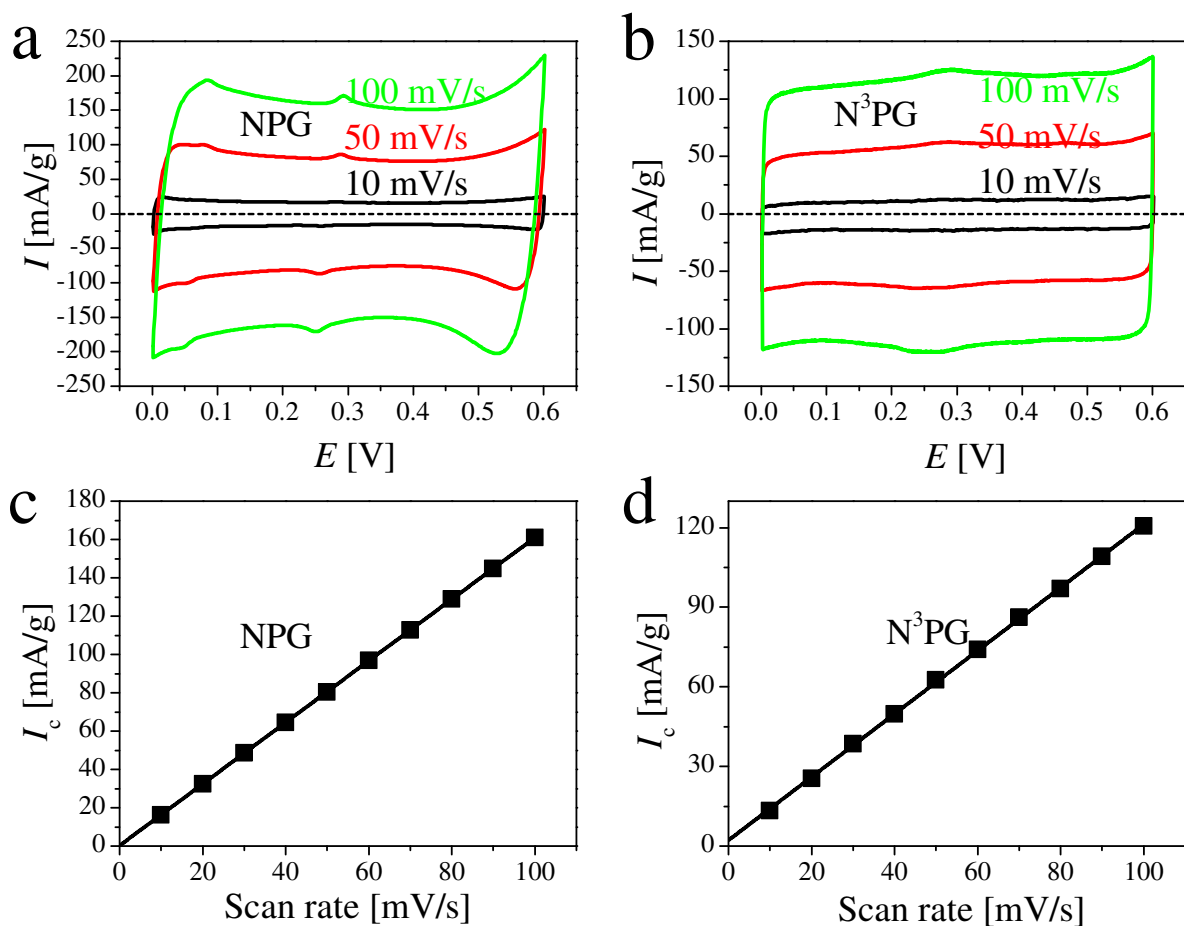
Figure 4.11: Electrochemical characterization of nanoporous gold (NPG) and nested-network nanoporous gold (N³PG). a), cyclic voltammograms of current *I versus* electrode potential *E* in the nominally capacitive regime using different scan rates as labeled in the figures. Solid lines, NPG, dashed lines, N³PG. b) mean current magnitude, I_C, at $E = 0.3$ V *versus* the scan rate. The data allow estimates of the mass-specific surface area.
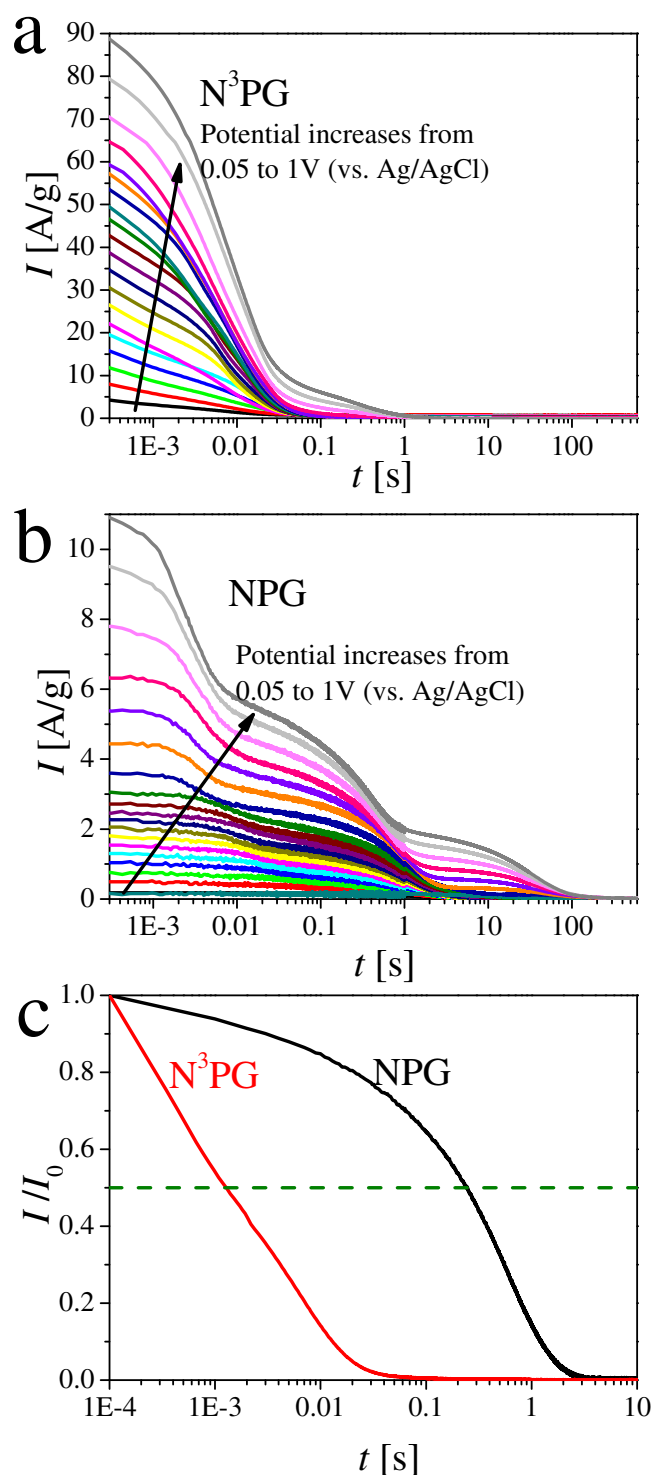
Figure 4.12: Charging kinetics of the porous materials. Transients of current, I, versus time, t, following potential steps from the starting electrode potential $E_0 = 0$ V to the final potential E_F. Graphs in a) and b) show experiments with E_F increasing from 0.05 to 1 V with an increment of 0.05 V Note the different charging kinetics in capacitive versus oxygen species electrosorption regimes. Graphs in c) compare current transients after jumping form $E_0 = 0.1$ V to $E_F = 0.2$ V for the two materials. Charging kinetics may be measured by time, $t_{\frac{1}{2}}$, required for charging current I to decay to 50 % of the initial current, I_0. Dashed line indicates $I/I_0 = 0.5$.

electrochemically functionalized material. The $t_{\frac{1}{2}}$ = 1.3 ms for N^3PG, which is nearly 200 times faster than the 250 ms in NPG, is found.

4.2 Discussion

4.2.1 Less noble element retention

The present findings for the LNE retention during dealloying of the dilute solid solutions at low overpotential connect to the underlying mechanisms and driving forces of dealloying. As a prerequisite for enabling the second dealloying step which is inherent to the present strategy, sufficient LNE retention is also the key to the synthesis strategy. This motivates the focus, in this discussion, on the LNE retention.

Ateya *et al.* have studied the corrosion of dilute noble metal alloys, focusing on the example of Cu-Au alloys [54, 55]. These authors observed a critical dealloying potential only for $x_{\text{Au}} > 0.1$. Yet, in their study of Ag-Au alloys, Sieradzki *et al.* [46] reported that the critical dealloying potentials for x_{Au} as low as 0.05, in agreement with the present findings. The results by Ateya *et al.* [54, 55] do agree with the present findings inasmuch as the retention of a considerable LNE fraction is found after dealloying of dilute solutions, including $Cu_{95}Au_5$ alloy. The observations are discussed in terms of pore walls which are Au-rich rather than pure Au [54]. Recently, the dilute $Ag_{95}Au_5$ alloy dealloying was studied by Artymowicz *et al.* [74] motivated by Pickering's work on $Cu_{90}Au_{10}$ alloy. Unlike the $Ag_{95}Au_5$ alloy fully dealloyed in the present thesis, they only dealloyed a certain thickness of the sample and find a high LNE retention within those layers which decreases with increasing dealloying potential. In that respect it is noteworthy that dilute solutions can be dealloyed at low overpotential. In acidic solution they are then likely free of oxygen adsorbate layers so that surface diffusion and, hence, coarsening behind the dealloying front are fast. This in turn implies the exposure of LNE atoms from the native alloy in the interior of the original ligaments to further dissolution. The high LNE retention in the experiment is therefore remarkable.

The LNE retention is more readily reconciled with the established observations when one adopts a phenomenological point of view. As the alloy becomes more concentrated in Au, the Nernst potential, E_{Nernst}, of the LNE will increase and the driving force for dissolution decrease. For any given value of E_{D}, the LNE dissolution must therefore stop at a finite LNE concentration. It is then instructive to inspect the variation of E_{Nernst} with composition, here for the example of Ag-Au alloy. Since solid solutions of Ag and Au have practically no misfit strain energy, their molar enthalpy of mixing, Δh_{mix}, may be approximated by that of the molten alloy. Drop calorimetry data in Ref. [78] imply a nearly parabolic variation, Δh_{mix} = $-17.3\ \text{kJmol}^{-1}\,x(1-x)$, for the melt. When this term is adopted in a regular solution equation of state for solid Ag-Au, one obtains for the Ag chemical potential

$$\mu_{\text{Ag}} = \mu_{\text{Ag}}^0 + \Delta h_{mix}x_{\text{Au}}^2 + RT\ln(1 - x_{\text{Au}}) \tag{4.1}$$

and, consequently, for the Ag Nernst potential

$$E_{\text{Nernst}} = E_{\text{Nernst}}^0 - [\Delta h_{mix}x_{\text{Au}}^2 + RT\ln(1 - x_{\text{Au}})]/F \tag{4.2}$$

where the superscript "0" denotes values for pure Ag. R, T, and F denote, respectively, the gas constant, temperature, and Faraday constant. The equation yields an increase in E_{Nernst} by 63 mV between pure Ag and the equiatomic solution. Since the critical dealloying potentials are at $E_{\text{D}} \gtrsim E_{\text{Nernst}}^0 + 300$ mV, equilibrium thermodynamics cannot explain the observed LNE retention under the acting corrosion conditions. Yet, the increase of E_{Nernst} implies a reduction in overpotential which is significant if one accounts for kinetics of corrosion, and specifically for the steep variation in the corrosion flux with the overpotential.

The above argument is consistent with the well-established variation of E_{C} with the alloy composition, see, for instance, Ref. [79] and the present results in Figure 4.1. The experimental observation here applies to corrosion which propagates throughout the material, in other words, to a macroscopic phenomenon. Nonetheless, it has been shown [14] that the empirical variation of E_{C} with the composition is consistent with results of an analysis of the *local* atomic rearrangements in the corrosion surface. This analysis considers the competition between dissolution on the one hand and passivation by lateral rearrangement of the MNE on the other [14]. It then seems natural to assume that, as Ag dissolution enriches the outermost layer at the corrosion surface in Au, the potential required for maintaining dissolution at a significant rate will rise. Eventually, the corrosion process will become so slow as to effectively stop even before all less noble metal is dissolved.

Snyder and Erlebacher [47] have analyzed the kinetics of corrosion from a different atomistic perspective, taking the nucleation of vacancy islands on crystal terraces as the rate-limiting step. Their atomistic model implies that the overpotential required to maintain a given nucleation rate increases with the noble metal content, in agreement with the composition- and overpotential-dependence of the dissolution flux in their experiments in nonaqueous solution. The steady-state dissolution flux, J_{SS}, was found to vary with the composition as [47]

$$J_{\text{SS}} \propto \exp - \frac{E_{\text{T}}}{k_{\text{B}} T} \qquad (4.3)$$

with the nucleation energy

$$E_{\text{T}} = 2.25\text{eV} x_{\text{Au}} + 0.53\text{eV} (1 - x_{\text{Au}}). \qquad (4.4)$$

When applied to the temperature, 300 K, of the present experiment, Eqs (4.3) and (4.4) imply that J_{SS} decreases by the factor ~ 1000 whenever x_{Au} is increased by 10 at.%. This is again consistent with the kinetic stabilization of a significant LNE content when dealloying uses the low dealloying potentials that are feasible in dilute alloys. Note, however, that the reasoning is based on a *de facto* phenomenological application of a rate equation that, being based on vacancy island nucleation on a given alloy, contains in its derivation no mechanism to arrest the dissolution at final LNE content. The argument is therefore not strictly self-consistent.

In summary, the discussion focuses on the finding of considerable LNE retention during the dealloying of dilute solid solutions of the MN element at low overpotential. This finding is qualitatively consistent with previous empirical data for the reduction of the corrosion rate and of the critical dealloying potential with reduced LNE content. The atomistic models of those latter findings are also compatible with a trend for corrosion to slow down when the LNE content drops, preventing full LNE removal during finite time. Yet, while those same models connect

to the removal of LNE on crystal terraces as the elemental corrosion step, they appear not to expose an atomic-scale process that would arrest the corrosion of any given terrace at a finite and substantial LNE-content. In fact, the available theory does not afford a prediction of the amount of LNE retention at a given value of the dealloying potential and master alloy composition. Dedicated numerical studies of the phenomenon, along with detailed experiments on dilute alloy corrosion would seem to be required for a clearer understanding of the factors that control LNE retention.

4.2.2   Nanosized ligament dealloying

Another issue that will be discussed here is the effect of nanosized ligaments on the dealloying of nanoporous Ag-Au alloys. According to the parting limit of bulk Ag-Au alloys, nanoporous $Au_{52}Ag_{48}$ alloy is already within the range of the upper range of parting limit which might cause a passivation and thus hinder the formation of the lower hierarchy level. However, based on recent studies on Ag-Au alloy nanoparticle dealloying [80, 81], a remarkable feature between nanoparticle and its bulk counterpart is that no parting limit is observed. That is to say, the nanoparticles with the composition above the parting limit can also be dealloyed. The two observations are quite analogous, and the present findings for ligaments are consistent with those of the nanoparticles.

The stability of nanoparticles is a crucial issue during their applications as electrocatalyst especially under an applied potential which might be sufficient to dissolve the nanoparticle. It is generally believed that nanoparticles normally have a negative shift of oxidation or dissolution potential compared with their bulk counterparts which have been verified in many studies [82–84]. The present nanoporous alloys also show a negative shift of dealloying potential. In pioneering works [85–88], Henglein and Plieth first explored the electrochemical properties of metal nanoparticles. The Gibbs-Thomson effect predicts that nanoparticles of radius r dissolve at lower electrochemical potentials than bulk materials. Based on the Gibbs-Thomson effect, nanoscale particles show a negative shift towards oxidation.

$$E = \bar{E} - \frac{\gamma\Omega}{nq}k \tag{4.5}$$

Here $\bar{E}$ is the reversible potential for the flat surface, γ is the isotropic solid/electrolyte interfacial free energy, Ω is the atomic volume, n is the number of exchanged electrons, and k ($k = \frac{2}{r}$) is the curvature of nanoparticles.

Dimitrov *et al.* [81] systematically studied the impact of shape and composition on the dealloying behavior of $Au_xAg_{(1-x)}$ alloys with different shapes which include nanoparticle, polycrystalline and well ordered (111) oriented Ag-Au alloys. According to their results, the relationship between alloy composition and E_C with different shapes is plotted to show the shape effect on the dealloying potential. It should be noted that their methods to determine E_C seem not so precise as E_C is determined by the MDP method. It can be found that nanoparticle shape Ag-Au alloys exhibit an obvious decrease of E_C of about 300-450 mV depending on the composition, and well ordered Ag-Au alloys show a slight increase of E_C of around 30-40 mV as shown in
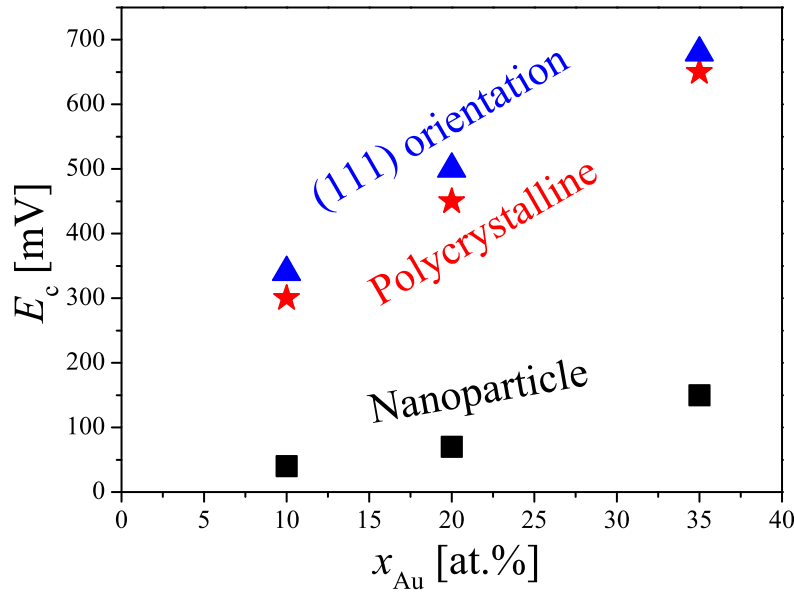
Figure 4.13: The relationship between the critical dealloying potential, E_C and the composition of nanoparticle, ploycrystalline, and (111) orientated Ag-Au alloys based on Dimitrov's results [81]. E_C shows the following trend for the same composition: (111) orientated > ploycrystalline > nanoparticle.

Figure4.13. This suggests that the shape factor plays an crucial role on E_C of the same alloy composition. E_C for the same shape Ag-Au alloys increases with increasing Au content. Using the values γ = 1.0 to 1.6 J m^{-2}, Ω = 1.6 × 10^{29} m^3, n = 1, and q = 1.6 × 10^{19} C to Equation 4.5, one calculates negative potential shifts on the order of 50 to 60 mV when the particle size is 10 nm for the redox potentials of metal nanoparticles. The curvature of nanoparticles only plays a part on the reduction of E_C compared with 300-450 mV. Therefore, factors that are beyond the curvature also contribute to the negative shift of E_C. One factor might be used to explain the negative shift of nanoparticle refers to their much larger surface area which results in more atoms expose to the electrolyte during dissolution.

It is particularly interesting to compare E_C of the present nanoporous Ag-Au alloys with E_Cs from Dimitrov's [81] findings of nanoparticle Ag-Au alloys and Sieradzki's results on the bulk Ag-Au alloys [46]. E_C of the present nanoporous Ag-Au alloys is used the data of Ag$_{95}$Au$_5$ alloy with differen dealloying potentials as shown in Figure 4.2b. For Dimitrov's [81] and Sieradzki's [46] results, E_Cs are extracted using the MDP definition. A Ag/AgCl reference electrode is used in this thesis and they used a Ag/Ag$^+$ reference electrode. The Nernst potential of pure Ag should be nearly the same, thus the reference potential can be deemed as nearly the same. The size of their nanoparticles in Ref [81] is about 10-15 nm which is very close to the ligament size after the first dealloying. The corresponding results are shown in Figure 4.14. The E_C values of bulk, nanoparticle and nanoporous shape Ag-Au alloys follow a linear relationship depending on the Au content. It also predicts that E_C of pure Ag nanoparticles shows a negative shift in comparison to the corresponding bulk alloys which has been verified
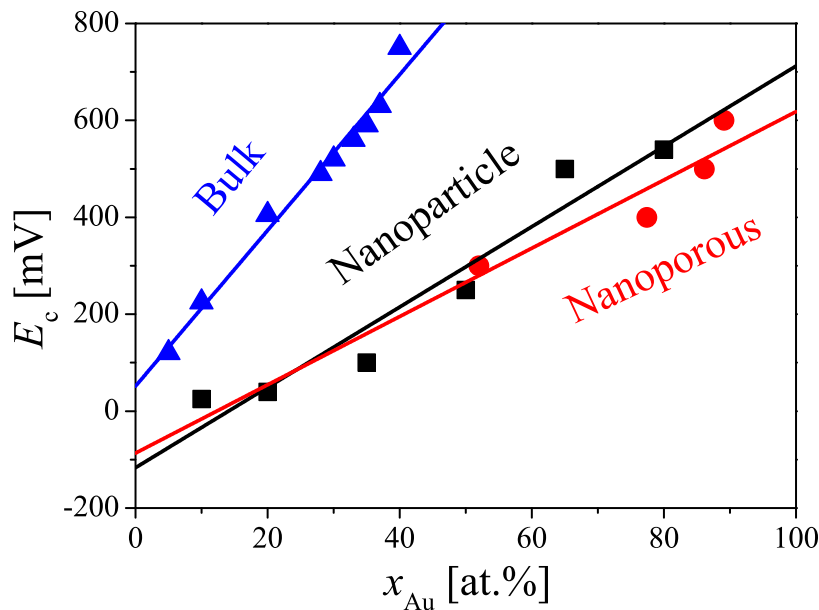
Figure 4.14: The critical dealloying potential, E_C comparison between different forms of Ag-Au alloys. The data of bulk Ag-Au alloys are obtained from Ref [46], the data of nanoparticle Ag-Au alloys are obtained from Ref [81] and the data of nanoporous Ag-Au alloys are from the present thesis. The lines showing there are fitting curves.

by Ivanova [83]. For the nanoporous Ag-Au alloys, it is shown that the E_C is exhibiting the same negative shifting trend as nanoparticle shape. The E_C of bulk $Ag_{48}Au_{52}$ alloy can be deduced based on Sieradzki's results [46] where they show the relationship between the Au content and E_C as $E_C(x) = E_C + x_{Au} \times 20$ mV where x_{Au} represent the Au content. The hereby estimated E_C for bulk $Ag_{48}Au_{52}$ alloys is more than 1000 mV (*vs.* Ag/AgCl). This value is 700 mV higher than that of the corresponding nanoporous shape alloys. Therefore, it can be concluded that nanoporous shape alloys also show a remarkable negative E_C shift compared with bulk shape samples. It should be noted that the slope of bulk sample E_C is much more pronounced compared with that of the nanoparticle and the nanoporous shapes. The values of E_C of nanoparticle and nanoporous shapes show a similar linear relationship.

In summary, nanosized Ag-Au alloy dealloying leads to a similar behavior as nanoparticle Ag-Au alloy dealloying, that is, a negative shift of E_C from the bulk Ag-Au alloy. The Gibbs-Thomson effect only accounts for part of E_C negative shift. Owing to the present theoretical and experimental constraints, further work should be carried out to examine which is the possible reason to the negative shift of E_C.

4.3 Conclusion

This Chapter demonstrates that dilute alloys of Au in Ag can be dealloyed at low overpotential so as to produce a massive nanoporous alloy in which roughly 50 % of Ag is retained. It is shown that the microstructure of the alloy can be made to coarsen by annealing, and that the material can subsequently be subjected to a second dealloying step which removes the LNE almost completely, producing a nanoporous noble metal structure that consists of self-similar, nested networks on two quite distinct length scales.

By control of the annealing and second dealloying conditions, both length scales can be independently tuned. N^{3}PG shows a faster charge transport rate than NPG, suggesting a faster switching in applications as a material with electrochemically tuneable properties. The two-step dealloying strategy has potential in fabrication of hierarchical porous structure in bulk form with precise control over two levels of pore size.

It is shown that the nested-network microstructure of the material accelerates the signal transport into the pore space by more than two orders of magnitude, as compared to conventional NPG with comparable mass-specific surface area. Nested-network porous solids may therefore open the way to electrochemically functionalized materials that have a greatly improved response time and switching frequency.

Chapter 5

Nested-network nanoporous gold with an ultrafine ligament size

In this chapter, a Pt doped Ag-Au alloy is chosen to fabricate nested-network nanoporous gold (N^{3}PG) which has a self-similar hierarchical structure with an ultrafine (less than 10 nm) lower hierarchy level ligament size. The strategy is the same as the dilute Ag-Au alloy which is also a two-step dealloying strategy. The purpose of using this Pt doped Ag-Au alloy is that Pt addition can stabilize a high Ag retention after the first dealloying. This guarantees an enough Ag amount for the second dealloying process. Both energy dispersive X-ray spectroscopy (EDS) and wavelength dispersive X-Ray spectroscopy (WDS) were preformed due to the overlap of characteristic peaks of Au and Pt and only 1 at.% Pt is present in the master alloy. Starting out with a Pt doped Ag-Au alloy, the initial Au content can increase to the standard composition range, here 20 at.% Au. Therefore, a less volume shrinkage compared with the dilute Ag-Au alloy in Chapter 4 is expected. The upper hierarchy level ligament size is tuned by annealing. A second dealloying will generate the lower hierarchy level ligaments within the upper hierarchy level ligaments. The advantage of Pt addition is that an ultrafine lower hierarchy level ligament size formed as a result of the slow surface diffusivity nature of Pt. X-ray diffraction was performed on the samples at each stage. Electron backscattering diffraction (EBSD) was carried out on the samples after the second dealloying process to study the crystal orientation. Using small angle X-ray scattering (SAXS), the lower hierarchy level ligament size was verified to be 6 nm which is in good agreement with scanning electron micrograph observations. The Pt effect on stabilizing the Ag retention is discussed.

5.1 Inspiration

Snyder *et al.* [59] found a remarkable Ag retention for their Ag-Au-Pt alloys after dealloying in a neutral solution where Ag oxides form to assist pinning Ag from dissolution. Vega and Newman [89, 90] systematically studied the electrochemical dealloying of Ag-Au-Pt alloys with a variation of the Au:Pt ratio and the Pt segregation effect upon annealing. A high Ag retention was found in the dealloyed layer which is up to 50 at.%. They attributed this phenomenon to

Pt segregation to the ligament surface which forms a passivation layer together with Au and Ag, leaving a Ag enriched layer underneath. Recently, Jin *et al.* [91] systemically investigated the relationship between the dealloying potential and the residual Ag content in a series of $Ag_{1-p}(Au_{95}Pt_5)_p$ alloys where p= 0.05, 0.1, 0.15, 0.20, and 0.25. The corresponding results are shown in Figure 5.1. It can be found that a high Ag retention is well preserved after dealloying. For Au content (x_{Au}) less than 10 at.%, a remarkable Ag retention which contains almost 60 at.% Ag was found. Furthermore, a useful finding which is helpful in making hierarchical nanoporous gold (NPG) is that a high Ag-content nanoporous alloy with x_{Au} higher than 10 at.% can be maintained. While for Ag-Au alloys without Pt doping where only 10 at.% Ag retention was found when x_{Au} is higher than 10 at.% from the results of dilute Ag-Au alloys in Chapter 4. Those Pt doped Ag-Au alloys also show that the decrease of Ag retention with increasing dealloying potential is similar to that of the dilute Ag-Au alloy. From those findings, the $Ag_{80}Au_{19}Pt_1$ alloy is identified as a suitable candidate to get a high Ag retention nanoporous Ag-Au-Pt alloy. The reasons to choose this alloy composition lie in that it has a high Ag retention which is close to the parting limit (enough to perform a second dealloying) and a high initial Au content (small volume shrinkage).
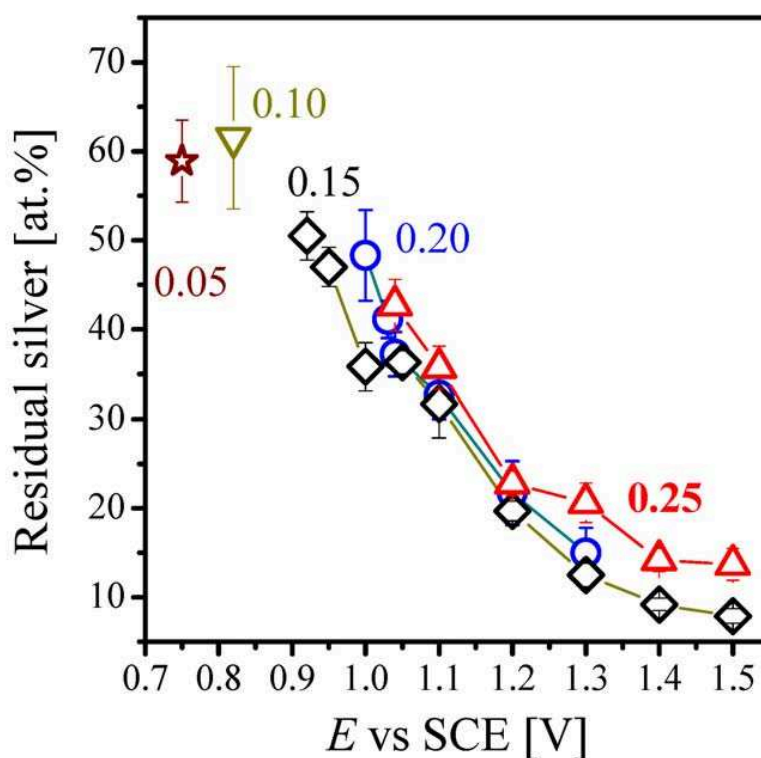

Figure 5.1: Residual Ag content *versus* dealloying potential of $Ag_{1-p}(Au_{95}Pt_5)_p$ alloys in 1 M $HClO_4$ soluton *versus* a saturated calomel electrode (SCE) reference electrode. Here $p = 0.05$, 0.10, 0.15, 0.20 and 0.25. Data extracted from Ref [91].

5.2 Experimental results
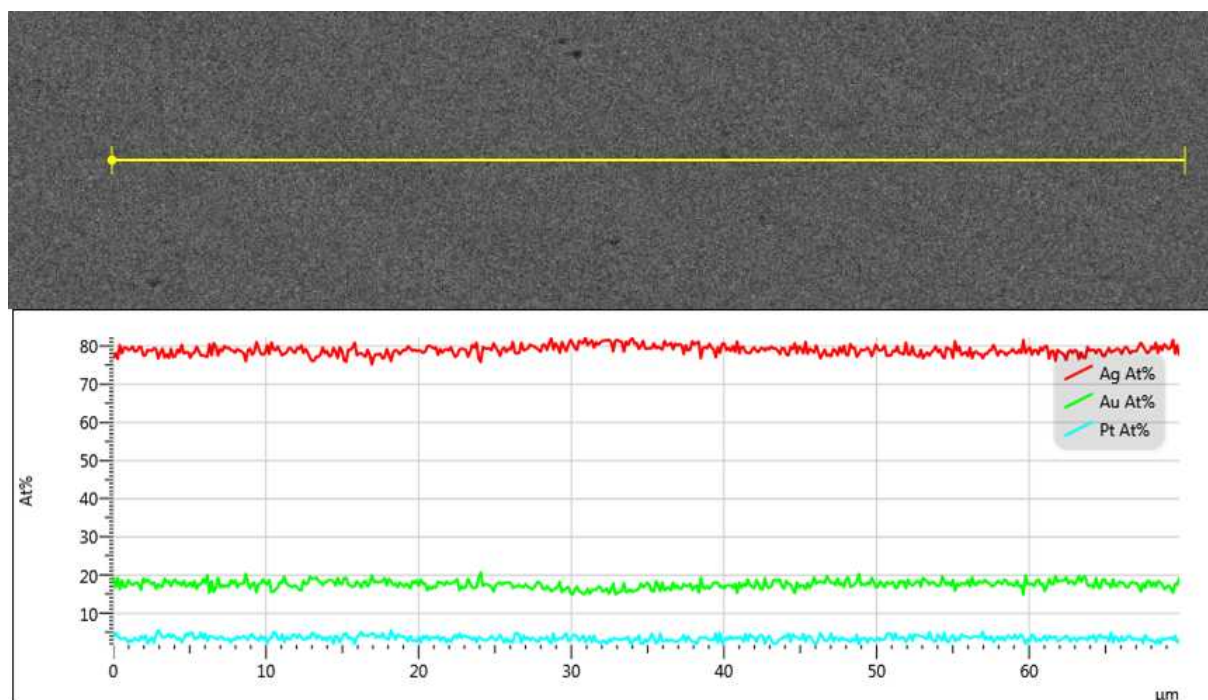
5.2.1 Master alloy composition distribution

Figure 5.2: Upper part: scanning electron micrograph of the $Ag_{80}Au_{19}Pt_1$ alloy before dealloying. Yellow line shows the linear scanned area. Lower part: the corresponding energy dispersive X-ray spectroscopy linear scan showing the composition of Ag (red), Au (green) and Pt (light blue) with atomic percent (At%), respectively.

Due to the fact that Pt has a high melting temperature of about 1768.3 °C whereas Ag is 961.78 °C and Au is 1064.18 °C, one should be cautious about inhomogeneous element distribution during Ag-Au-Pt alloy sample preparation, especially, for very low Pt constituent. In fact, during the experiments, an inhomogeneous elements distribution among some of the samples was observed. The inhomogeneous elements distribution will lead to an inhomogeneous ligaments distribution, especially, during annealing process. Also the less noble element (LNE) content in some regions may be too low to perform a second dealloying process. Therefore, the inhomogeneous element distribution will lead to a direct failure of the present two-step dealloying strategy as a high Ag-content nanoporous Ag-Au alloy is the prerequisite to perform another dealloying. Therefore, a step by step alloy preparation process as described in Chapter 3 was used to prepare a homogenous alloy. Still it is necessary to examine the master alloy composition distribution before performing the next step dealloying experiments. Due to the fact that only 1 at.% Pt is in the master Ag-Au-Pt alloy and Pt and Au have a very close characteristic X-ray at both L and M shells which are overlapped, energy dispersive X-ray spectroscopy (EDS) may not be a suitable technique to acquire the correct composition. Wavelength dispersive X-Ray spectroscopy (WDS) has a significantly higher spectral resolution and enhanced quantitative po-

tential compared with EDS, as it measures or counts only the X-rays of a single wavelength at a time. WDS offers a better resolution to distinguish the two close elements which have similar characteristic X-rays. Therefore, WDS was also selected to examine the element distribution in the master $Ag_{80}Au_{19}Pt_1$ alloy. A comparison between the results of those two techniques for the $Ag_{80}Au_{19}Pt_1$ alloys is shown in Figure 5.2 and 5.3.

EDS measurement was carried out on the $Ag_{80}Au_{19}Pt_1$ alloy first. Figure 5.2 shows a linear EDS scan with a range of approximate 80 μm scanned on a random position at the sample. It can be found that the Ag, Au and Pt distributions are homogenous along the scanned region. Little composition fluctuation can be found. The Ag, Au and Pt compositions in the master alloy are 78 ± 2, 18 ± 2, and 4 ± 1 at.%, respectively. The results were calculated based on at least 5 random spots from the same sample. Ag and Au compositions are consistent with the master alloy composition, while Pt composition exceeds the expected value, since only 1 at.% Pt is in the alloy. It is not true that an amount of Pt around 4 at.% can be found in the present $Ag_{80}Au_{19}Pt_1$ alloy. Clearly, there is an error on reading the correct Pt content by EDS. From the EDS spectrum of a selected area as shown in Figure 5.3, the characteristic peaks of Au and Pt are overlapped due to the fact that they have very close characteristic X-ray energy range, especially, at low energy range. That is because the spectral resolution for EDS is 150 eV while that of WDS is 5 eV. Pt characteristic peaks are overlapped by Au peaks as their characteristic peaks are close to each other during EDS measurements and therefore the determined Pt content is not correct.

After calibrated with the standard reference targets of pure Ag, Au and Pt, the WDS measurements with the same sample at standard working parameters were performed, see details in Chapter 3. Using WDS, the composition of $Ag_{80}Au_{19}Pt_1$ alloy was measured and the result shows a composition of $Ag_{79.3}Au_{19.9}Pt_{0.8}$. From the WDS spectrum, the Au and Pt characteristic peaks are well recognized at less than 1.5 Å which is highlighted in the inset of Figure 5.3 and they are well distinguished from each other. The EDS and WDS measurements confirm that the master $Ag_{80}Au_{19}Pt_1$ alloy composition is homogenous and accurate.

5.2.2   Structure evolution

Now a homogenous master $Ag_{80}Au_{19}Pt_1$ alloy is obtained. The next step is to decide the dealloying potential for this $Ag_{80}Au_{19}Pt_1$ alloy. As stated and verified in Chapter 4, loss of passivation potential (LPP) offers a much more accurate method to measure the true E_C. Therefore, the determination of E_C is performed directly by using the LPP method. In this way, the appropriate dealloying potential for the first dealloying step was determined as 650 mV (*vs.* Ag/AgCl reference electrode).

Figure 5.4 shows the SEM images of the $Ag_{80}Au_{19}Pt_1$ alloy after dealloying at 650 mV. After removing part of Ag content from the master alloy by dealloying, a typical nanoporous structure can be found as shown in Figure 5.4a. The ligaments are uniformly distributed all over the sample. The corresponding ligament size is ~ 22 nm from Figure 5.4b at a higher magnification. An EDS analysis was performed on this sample, and the EDS results suggest a composition of $Ag_{46.5}Au_{46.9}Pt_{6.6}$ at this stage. Here, only the Ag retention is the main interest, therefore, EDS

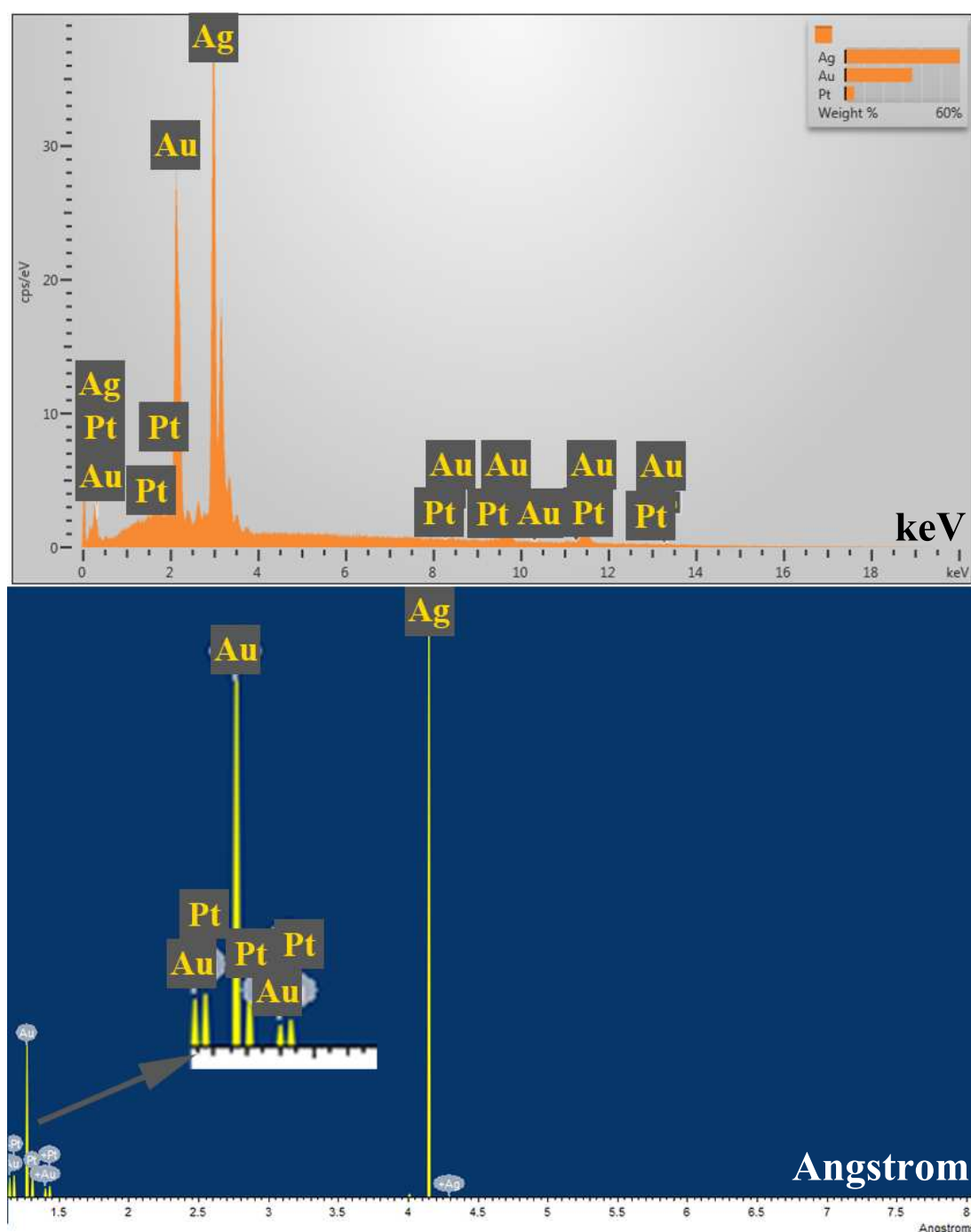Figure 5.3: Upper part: a typical energy dispersive X-ray spectroscopy spectrum of the master $Ag_{80}Au_{19}Pt_1$ alloys. Lower part: a typical wavelength dispersive X-Ray spectroscopy (WDS) spectrum of the master $Ag_{80}Au_{19}Pt_1$ alloys. The low wave length part is enlarged in the WDS spectrum to clearly show the well resolved Au and Pt peaks.

is sufficient to quantify the Ag content. Now, a high Ag retention nanoporous Ag-Au-Pt alloy is obtained. It is, therefore, promising to first tune the upper hierarchy level ligament size by annealing and followed by performing a second dealloying to create the lower hierarchy level ligaments.
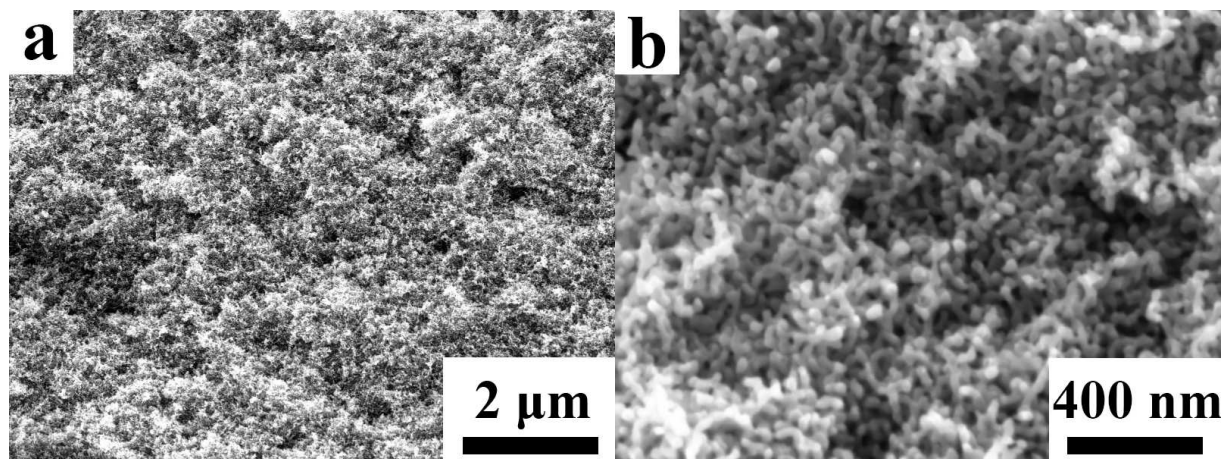

Figure 5.4: Scanning electron micrographs showing the cross section view of the $Ag_{80}Au_{19}Pt_1$ alloys dealloyed at 650 mV. a), an overview and b), at a higher magnification.

The samples after the first dealloying were annealed to generate different sizes of the upper hierarchy level ligaments. Figure 5.5 shows the samples first dealloyed at 650 mV and after that annealed at different temperatures with the same time period. The ligament size increases with increasing annealing temperature as shown in Figure 5.5 a, c and e. The ligament size is ~ 110 nm after annealing at 400 °C for 0.5 h as shown in Figure 5.5b. When the sample was annealed at 500 °C for 0.5 h, the ligament size is ~ 200 nm (Figure 5.5d). For the samples annealed at 600 °C for 0.5 h, the ligament size is coarsened to ~ 300 nm (Figure 5.5f). It should be noted that a densification of the pores is observed at samples annealed at 600 °C for 0.5 h. Therefore, the second dealloying process is only carried out on the samples annealed at 400 and 500 °C.

After the annealing process, the samples were dealloyed again at 1000 mV to further remove the Ag retention, resulting in the formation of the lower hierarchy level ligaments. Figure 5.6 shows the SEM image of the N³PG annealed at 400 °C. It can be found that the upper hierarchy level ligament feature is well preserved and the lower hierarchy level ligament size is quite small (Figure 5.6a). From the cross section view, the lower hierarchy level ligaments are only visible at fracture surfaces while no obvious fine pores can be found on the surface of upper hierarchy level ligaments.

SEM image at a higher magnification is shown in Figure 5.6b to reveal the lower hierarchy level ligament size. The lower hierarchy level ligaments are contained within the upper hierarchy level ligaments. It shows that the lower hierarchy level ligament size is ~ 6 nm. This is in good agreement with previous studies on single NPG doped by Pt where the ligament size varied from 4-6 nm depending on the Pt content [27]. Considering only 5% Au is replaced by Pt, Pt addition seems to highly affect on slowing down the fast Au solid diffusion compared with NPG without doping, for instance N³PG obtained from the dilute Ag-Au alloy only has a lower hierarchy level ligament size of about 15 nm [72]. To date, the finest ligament size reported from a bulk
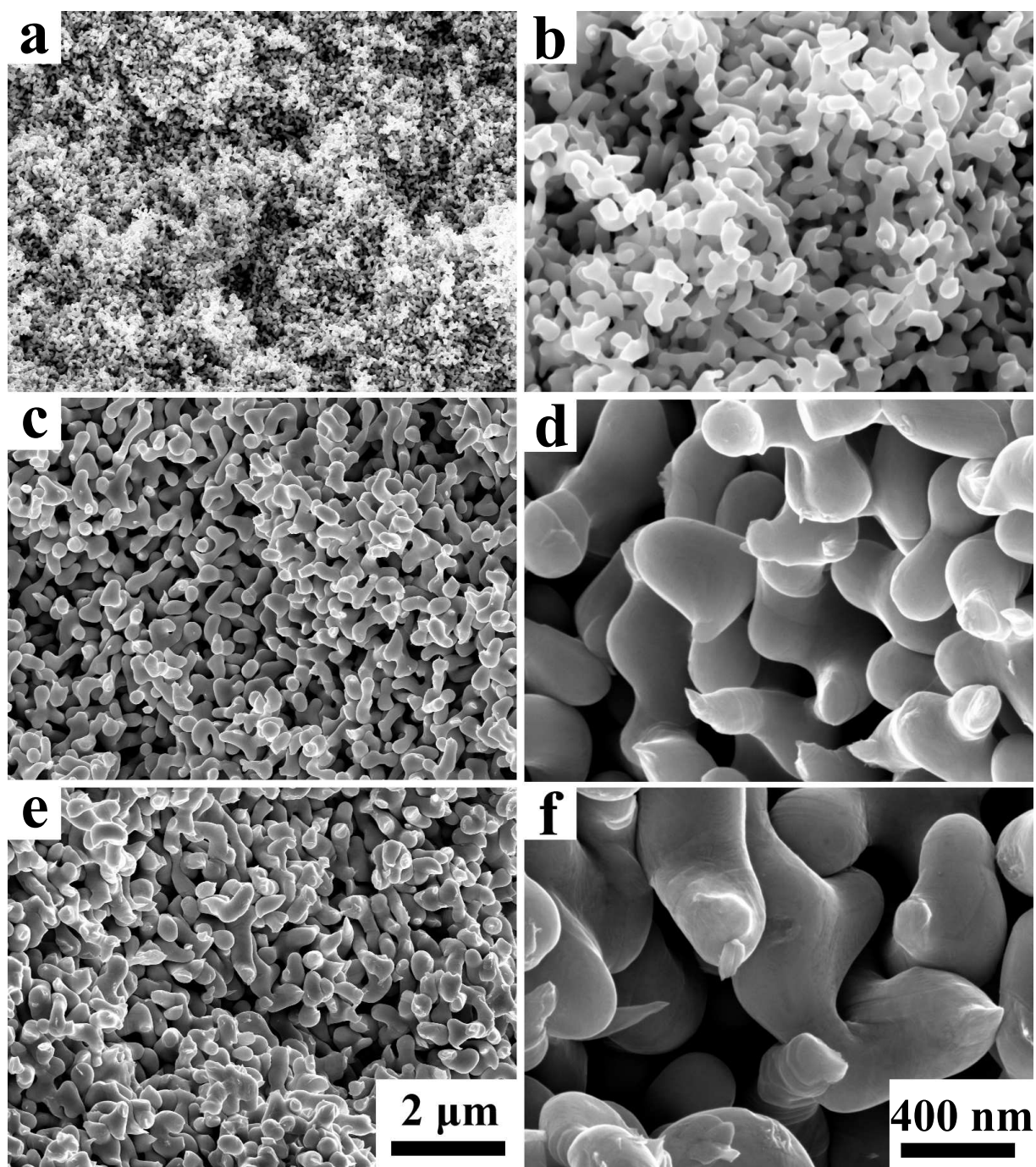
Figure 5.5: Scanning electron micrographs showing the cross section view of the as-dealloyed $Ag_{80}Au_{19}Pt_1$ alloys with different annealing temperatures. a and b), 400 °C for 0.5 h. c and d), 500 °C for 0.5 h. e and f), 600 °C for 0.5 h. The ligament size is a highly dependent on the annealing temperature.
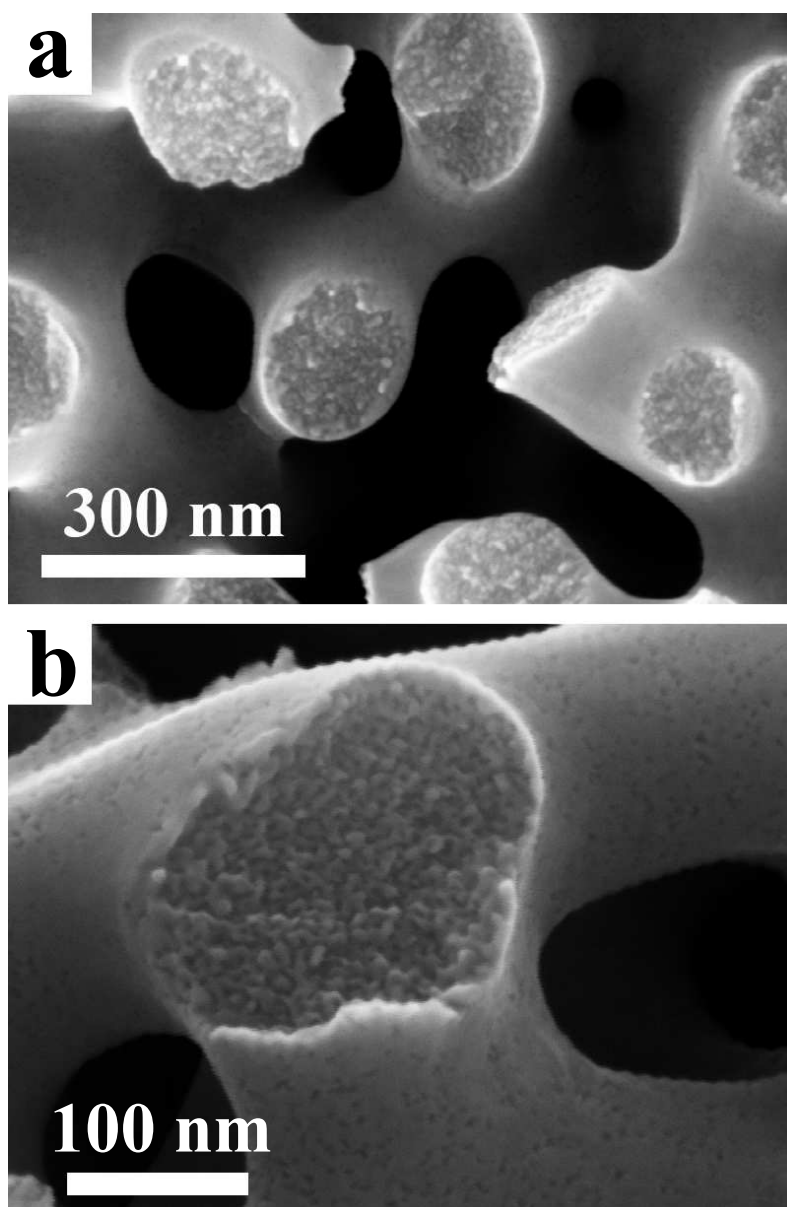
Figure 5.6: Scanning electron micrographs showing the microstructure of hierarchical nanoporous gold which is obtained by annealing at 400 °C for 0.5 h. a), hierarchical structure with two distinguished ligament structures is revealed. b), highlights the cross section of an upper hierarchy level ligament in which the lower hierarchy level size is recognized as ~ 6 nm.

precursor alloy without Pt is 9 nm [50]. For NPG with hierarchical or bimodal structure, to date no ligament size less than 10 nm has been reported.

Figure 5.7 shows the SEM images of the N^{3}PG annealed at 500 °C. The upper hierarchy level ligaments are also well preserved after the second dealloying process. The lower hierarchy level ligaments size is similar to the samples annealed at 400 °C after dealloying which is ~ 6 nm. This suggests that the upper hierarchy level ligament size can be modulated via selecting annealing temperature and time which is a typical method to create different ligament size [56]. Moreover, the lower hierarchy level ligaments are observed on the surface of upper hierarchy level ligaments as shown in Figure 5.7b.

Figure 5.8 shows the cross section overview of N3PG with ultrafine ligaments. Compared with N^{3}PG as shown in Figure 4.8, no granular structure with a size of tens of microns compared with the dilute Ag-Au alloys can be found in this sample. Only some large cracks can be found which might be caused during cutting the sample. This suggests that the present sample has a good integrity when the hierarchical structure formed.

Figure 5.9 shows the macroscopic view of the samples at each stage. It can be found that the samples at each stage do not show an obvious volume shrinkage compared with the dilute Ag-Au alloys where 80 wt.% weight is removed during the first dealloying process which results in a volume shrinkage of 60 % [72]. Here, the weight loss is only 50 wt.% during the first dealloying process which is equivalent to the weight loss observed during dealloying the standard composition Ag-Au alloys used to prepare NPG. After the first dealloying, stage I, the volume shrinkage is only 20 % for the present Pt doped Ag-Au alloys. After annealing, stage II, the sample show no obvious change. Also, the samples keep their integrity and no volume shrinkage can be found after the second dealloying process, stage III, as shown in Figure 5.9.

5.2.3 X-ray diffraction study

X-ray diffraction was carried out on the samples at each stage. Figure 5.10 shows the X-ray diffraction pattern of the master $Ag_{80}Au_{19}Pt_1$ alloy. The observed peaks can be indexed according to the crystallographic structure data of the solid-solution Ag-Au crystals. This alloy shows no preferred crystal orientation since the corresponding peak intensities agree with the ones given in the X-ray diffraction PDF database. There are some small peaks can be found in this pattern. Considering Pt and Ag do form intermetallic compounds, there may be some precipitations formed if there is an inhomogeneous elements distribution. Another possibility that can cause the present small peaks is tungsten oxide may be introduced to the alloy during melting process as the electrode is tungsten which may be oxidized during melting process. However, none of them can be identified to the known phase from the X-ray diffraction PDF database.

X-ray diffraction patterns of the samples at all three stages are shown in Figure 5.11. The characteristic peaks at 2θ 38, 44, 64 and 77° can be easily recognized as the 100, 111, 200 and 220 crystal planes. The crystal orientation is well kept after each step. The sample at stage I shows broaden peaks which can be attributed to the formation of nano-sized ligaments. The pores modulate the radial distribution function in such a way as to selectively reduce the number
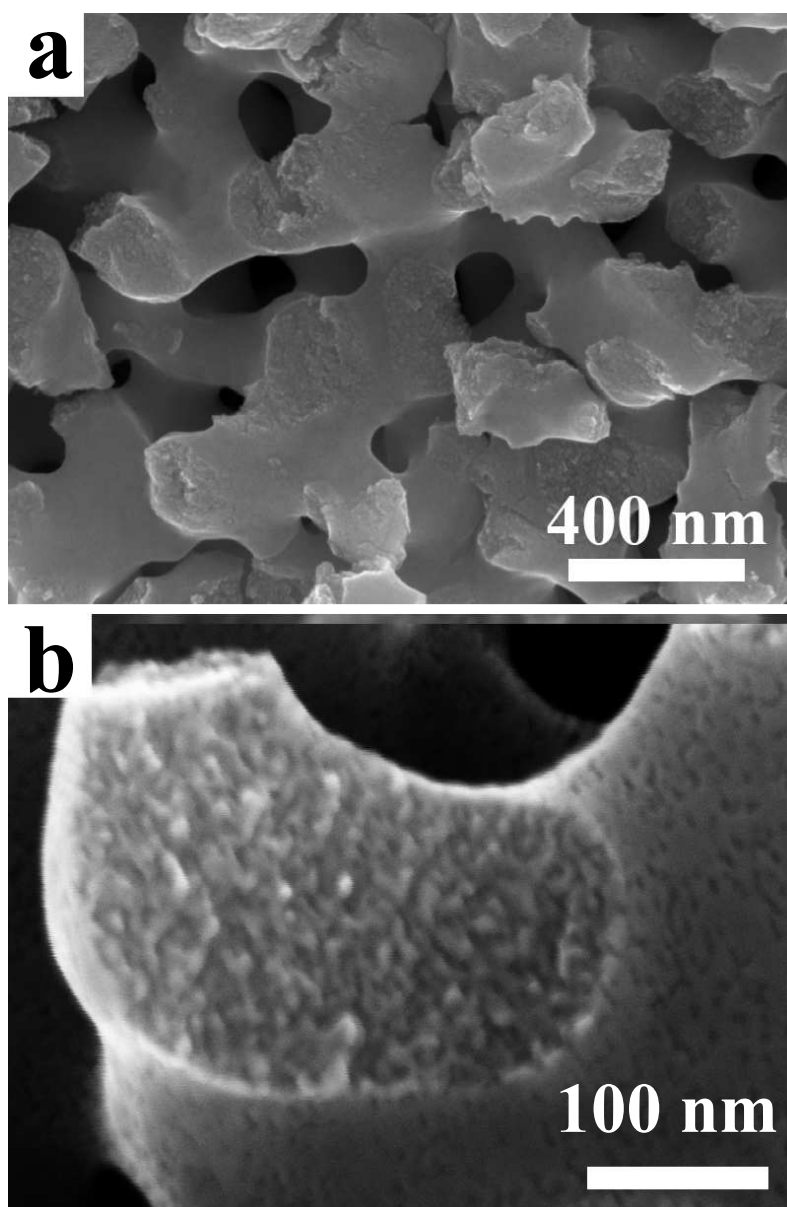
Figure 5.7: Scanning electron micrographs showing the microstructure of hierarchical nanoporous gold which is obtained by annealing at 500 °C for 0.5 h. a), the cross section view of the hierarchical nanoporous gold. b), highlights the cross section of an upper hierarchy level ligament in which the lower hierarchy level size is recognized.
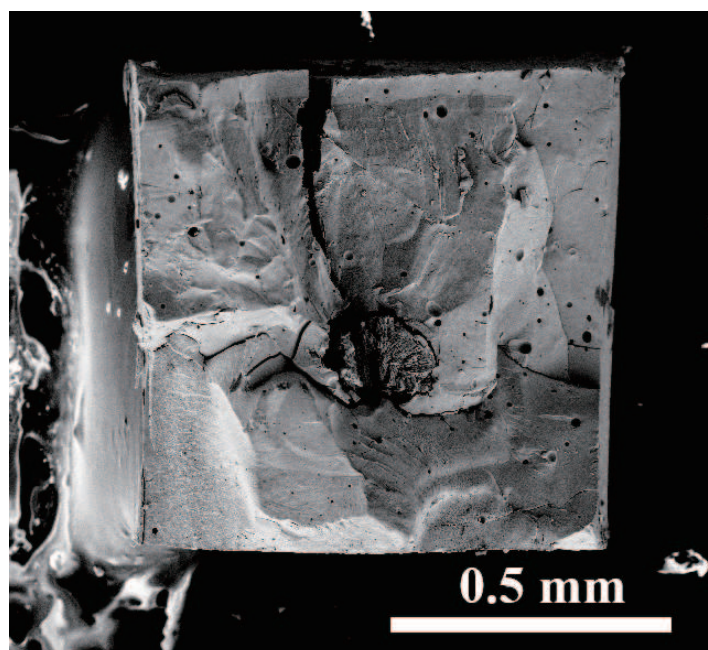
Figure 5.8: Scanning electron micrographs image showing the cross section overview of hierarchical nanoporous gold doped by Pt.

Figure 5.9: Macroscopic view of the $Ag_{80}Au_{19}Pt_1$ alloys at different stages from left to right which are: the master alloy (alloy), dealloyed at 650 mV (stage I), followed by annealing at 400 °C for 0.5 h (stage II) and finally dealloyed at 1000 mV (stage III) to create the lower hierarchy level ligaments. The scale bar in the image is 1 mm.

Figure 5.10: A typical X-ray diffraction pattern of $Ag_{80}Au_{19}Pt_1$ alloy before dealloying.

of nearest neighbors at intermediate and long distances from a central atom. That contributes to the peak broadening.
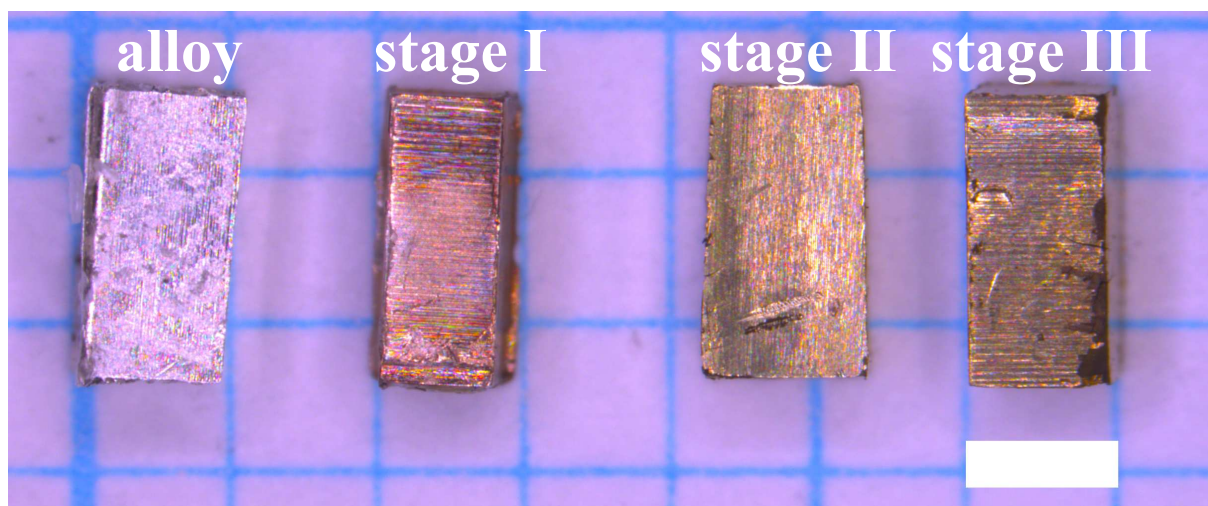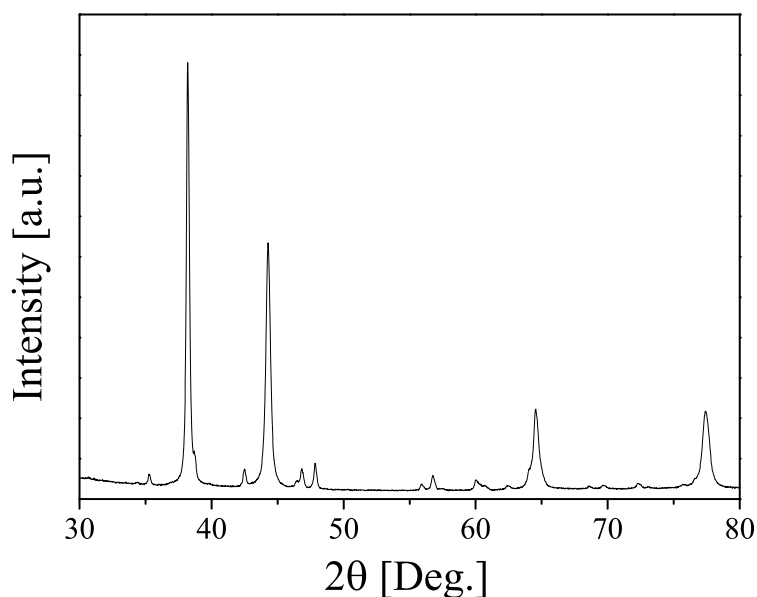
After annealing, the peak width of sample at stage II becomes narrow due to the formation of large sized ligaments. The X-ray diffraction peak shapes of sample at stage III remain the same as stage II. The extremely sharp reflections in stages II and III indicates that pores only make a moderate contribution to the peak broadening. It then appears natural to assume that microstrain makes a major contribution to the broadening. However, whether this is true or not comes from the fact that the higher order diffraction peaks do not look that much broader than the 111. That observation is more consistent with a size induced broadening (loss of coherency) than that with microstrain. The issue of X-ray diffraction line profiles of porous single crystals may not be adequately treated and understood in the existing literature [92, 93].

5.2.4 Grain size study by electron backscattering diffraction

Figure 5.12a shows the overview SEM image of the hierarchical NPG doped with Pt samples with the upper hierarchy level ligament size of 110 nm for EBSD measurements. An obvious feature is that the integrity of the sample is well kept. The sample is of high quality which is entirely free of cracks. Figure 5.12b exhibits a clear view of grain boundary junctions. Several grains meet at those junctions and they have different orientations as indicated by the color differences. It can also be found that the grain size is in the order of tens of microns. The detail explanation of the color interpretation is introduced in Chapter 3. Considering the sample preparation for the master alloy is similar to Jin's work [40], in which the original alloy's grain size is in the same range. Therefore, the present results is consistent with their results.
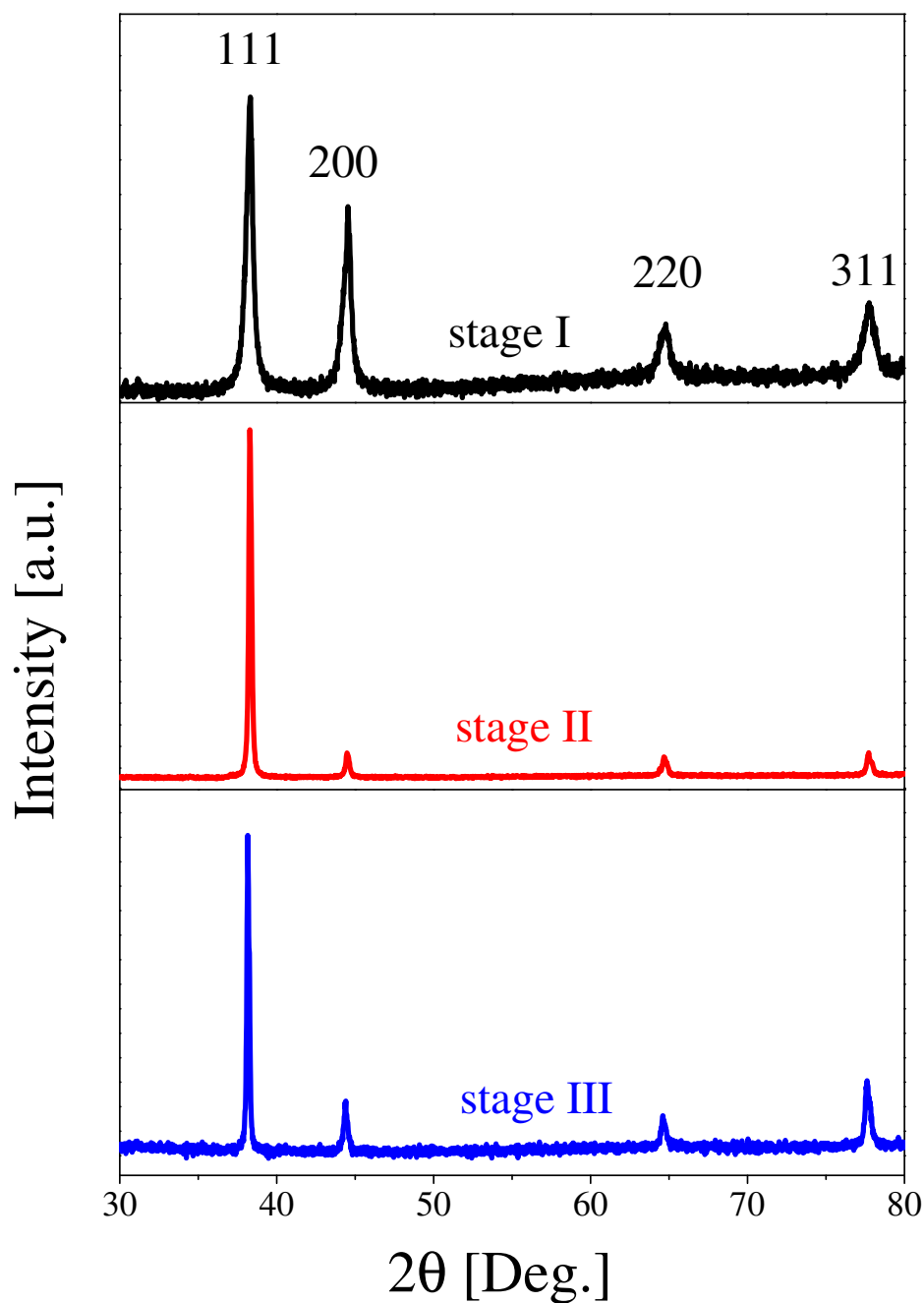
Figure 5.11: X-ray diffraction patterns of the $Ag_{80}Au_{19}Pt_1$ alloys at each stage during the formation of hierarchical structure. Stage I is the sample dealloyed at 650 mV, followed by annealing at 400 °C for 0.5 h to coarsen the structure marked as stage II, and finally a second dealloying of the sample at 1000 mV to form the lower hierarchy level ligaments marked as stage III.
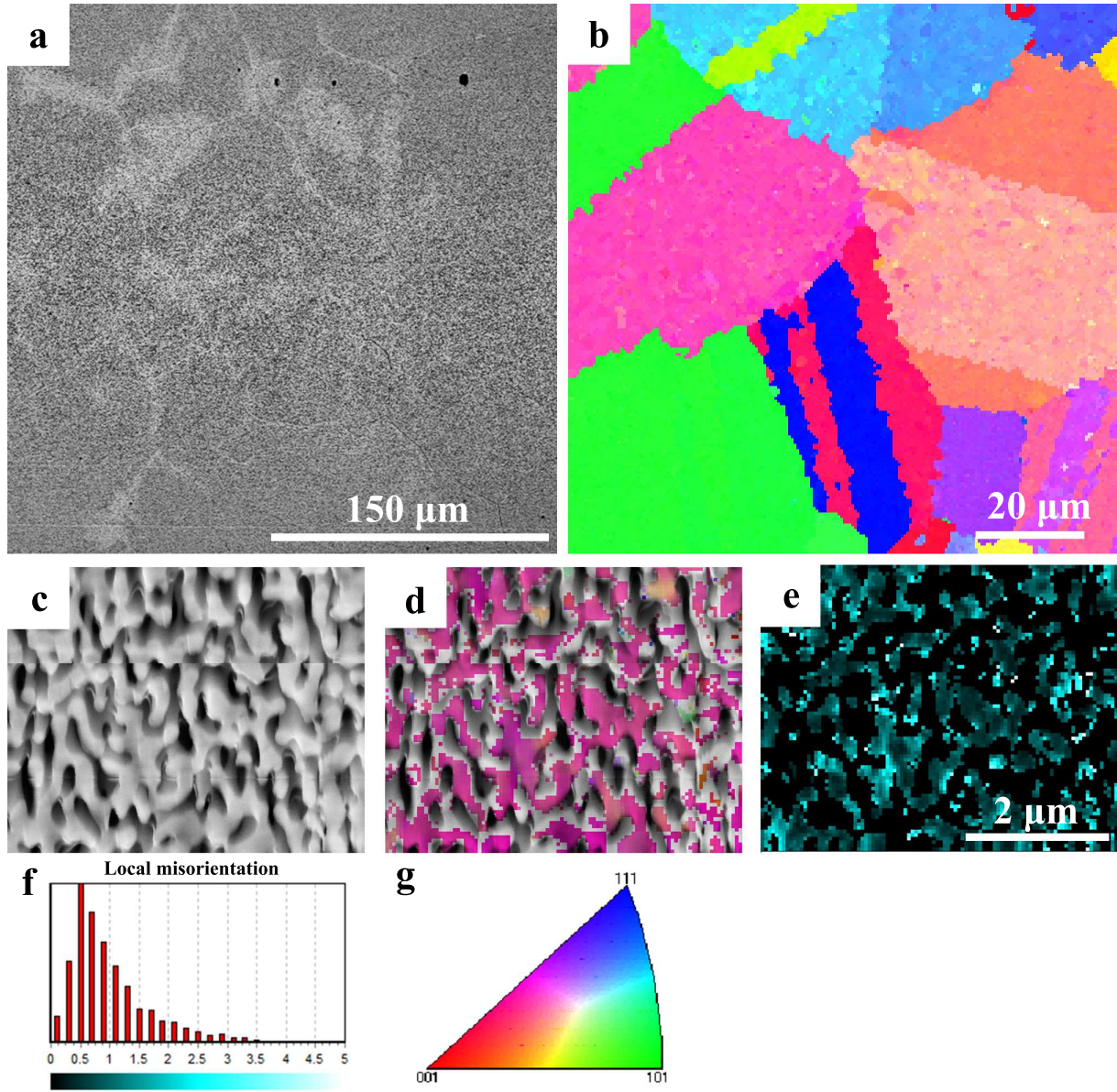
Figure 5.12: Scanning electron micrographs and electron backscattering diffraction (EBSD) measurements of the hierarchical nanoporous gold which was first dealloyed at 650 mV, followed by annealing at 400 °C for 0.5 h and finally dealloyed at 1000 mV. a), the overview of the scanning electron micrograph. b), EBSD orientation map with a scanned area of $100 \times 100 \ \mu m^2$ at a step size of 0.5 μm which clearly shows a grain size of 20-100 μm and the grain boundaries. c), scanning electron micrograph showing the corresponding EBSD measurement scanned area of $5 \times 4 \ \mu m^2$ within one single grain. d), the corresponding EBSD orientation map at a step size of 0.05 μm. e), the corresponding local misorientation map. f), the corresponding local misorientation distribution histogram to e). The local misorientation is smaller than 5°. and g), the inverse pole figure color code.

The grain orientation of the present sample is well preserved after the hierarchical structure has formed. Figure 5.12c shows the SEM image for which the EBSD measurement was performed with a scanned area of 5×4 μm^2 within one single grain. Figure 5.12d shows the corresponding EBSD orientation map scanned with a step size 0.05 μm. The nanoporous feature of the sample is resolved by EBSD as the pixels cannot be indexed which represent the large pores (upper hierarchy level). Figure 5.12e is the local misorientation map which indicates a very small misorientation within one single grain. Figure 5.12f shows the corresponding histogram showing the local misorientation which is less than 5°.

5.2.5 Small angle X-ray scattering study on lower hierarchy level pore size

During preparing this Pt doped Ag-Au alloy, the lower hierarchy level ligaments were hard to be characterized with SEM as their size is only ~ 6 nm which is close to the resolution limit of SEM. Also the low contrast between solid ligaments and pores leads to a low quality image which cannot resolve the fine structure. Therefore, in order to confirm the existence of lower hierarchy level ligaments, small angle X-ray scattering (SAXS) which is normally used to evaluate porous materials, was performed to determine the pore size.

Figure 5.13 shows the results of a SAXS experiment on a sample prepared under identical conditions as above mentioned three stages. A representation in a log-log plot of Iq^2 versus q is adopted, which emphasizes both interference phenomena and the high-q power-law behavior. The reason to use this expression is to emphasize the small peaks to make them much more obvious. In stage I, the $Ag_{80}Au_{19}Pt_1$ master alloy has been dealloyed at 650 mV. The SAXS graphs exhibit a clear maximum around $q = 0.29$ 1/nm. Equation 2.12 links this to an inter-ligament spacing $d = 27$ nm. This is slightly larger than the ligament diameter, $L = 22$ nm inferred from the SEM images. The finding $d \gtrsim L$ is not unexpected, as the solid fraction is less than unity. The SAXS data are thus in good agreement with the ligament size determined via SEM. Beyond the interference peak, the intensity decays as $I \propto q^{-4}$, consistent with the notion of a uniform electron density in the ligaments and discontinuous surfaces. The SAXS graphs labeled "stage II" refer to the structure after annealing, where the SEM analysis indicates L = 110 nm. This ligaments size it outside the resolution of the present SAXS experiment, and indeed the scattering data show a Porod behavior throughout the entire q-range of Figure 5.13. However, the signature does again change after the second dealloying process ("stage III"). Figure 5.13 shows the emergence of an interference signature in the form of a hump well above the extrapolated Porod part, near the upper q-limit of the experiment. The position of the hump, near $q = 1.2$ nm^{-1}, suggests $d \sim 6.5$ nm. This is again compatible with the ligament size of ~ 6 nm observed from SEM images. The good agreement with Porod's law at the lower q indicates that the structure of the nanoporous network with each upper-hierarchy-level ligament is uniform.
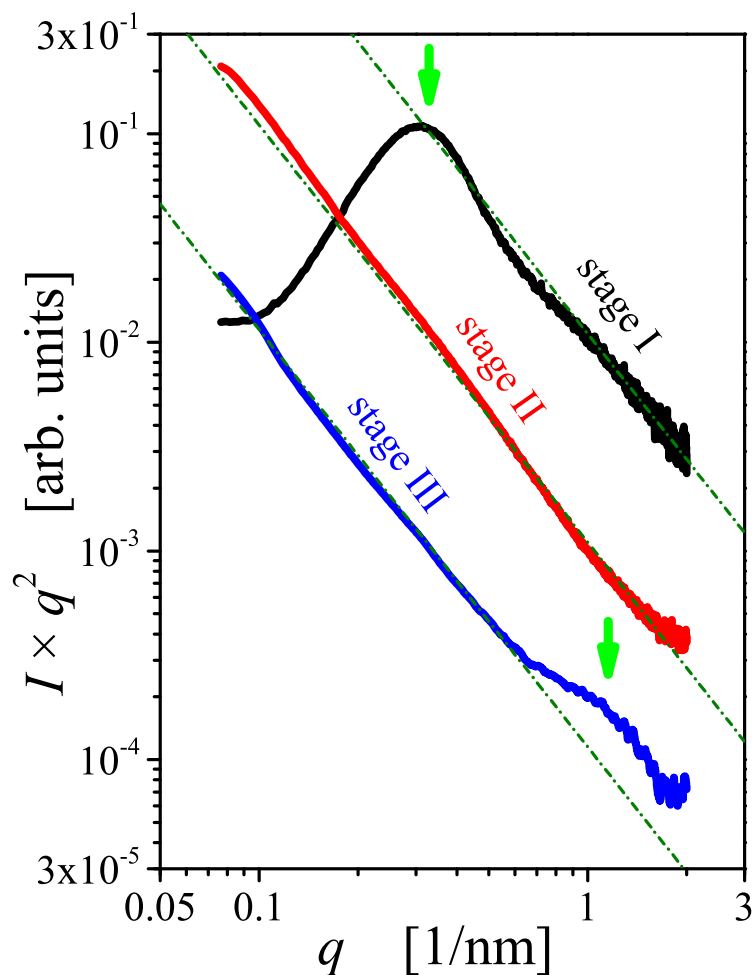
Figure 5.13: Display of small angle X-ray scattering data, showing the intensity I multiplied by the square of scattering vector magnitude q versus q on a log-log scale. Graphs refer to successive stages of synthesis, after initial dealloying (stage I), after subsequent coarsening (stage II), and after the conclusive second dealloying step (stage III). Dash-dotted lines have slope -2 on the scale of the graph, illustrating the Porod-behavior. Arrows denote interference maxima from the initial ligament structure (stage I) and from the lower hierarchy level of final nested network structure (stage III). Coarser structures in stages II and III, forming the upper hierarchy level, are not resolved. Parameters: master alloy $Ag_{80}Au_{19}Pt_1$, first dealloying step at 650 mV, annealing at 400 °C for 0.5 h, second dealloying step at 1000 mV.

5.3 Discussion

5.3.1 Less noble element retention by Pt

The high Ag retention is attributed to Ag buried in the ligaments like a core-shell structure, here Ag in the core, thus Au passivates the surface [89, 90]. Although only a certain layer thickness was dealloyed and characterized, a remarkable finding is that a high Ag retention is found after dealloying. It was also proposed that the composition gradient is less pronounced due to the Pt addition compared with binary Ag-Au alloys which is good for composition control over a large range. Experimentally, this result proved that a high Ag retention can be obtained from the Ag-Au-Pt alloys in acid solutions using a potentiostat to control the dealloying process.

A constant current density output in the above studies was conducted which means a higher dealloying potential compared with the present case which is a constant potential output. In order to maintain a constant current density, the potential needs to be increased to compensate the current loss during the dissolution process. As proved by the dilute Ag-Au alloy and the Ag-Au-Pt alloy, the Ag retention is highly sensitive to the dealloying potential. It is expected that more Ag retention is maintained by selecting the dealloying potential much more closer to E_C and a constant potential output. It is confirmed in the present Chapter that the dealloying of Ag-Au-Pt alloys leads to a high Ag retention which is able to control the LNE retention not only in a certain layer thickness but also throughout the bulk sample.

Pt segregation onto the surface is discussed as the reason for the high Ag retention in Ag-Au-Pt alloys after dealloying [59]. This phenomenon might be explained by the anodic segregation such as P during dissolution of austenitic stainless steel [94]. In Jin's work [27], a pronounced Pt reduction peak compared with Au was observed from cyclic voltammetry measurements which indicates a Pt enrichment on the surface. The Pt reduction peak and Au reduction peak are well resolved. The possible explanation for the pronounced Pt reduction peak is also attributed to the formation of the Pt surface segregation. A similar dealloying protocol was used in the present study. Therefore, it is reasonable to use the same explanation to explain the present high Ag retention in the Ag-Au-Pt alloy after dealloying. This suggests that the present high Ag retention in Ag-Au-Pt alloy lies in the Pt addition which benefits from Pt segregation and its slow diffusivity. The Pt addition will slow down the surface diffusion of Au, therefore, preventing a postpone coarsening where more Ag atoms tend to be exposed to the electrolytes and dissolve which in return stabilizes the Ag retention.

5.3.2 Critical ligament size to form nanoporosity

The ligament size after the first dealloying is ~ 22 nm as shown in Figure 5.4. The lower hierarchy level ligament size is about 6 nm. Could it be possible to create the lower hierarchy level ligament within the ligaments of 22 nm in size? That is to say, direct dealloy the newly form nanoporous Ag-Au-Pt alloy without annealing process to tune the ligament size. To test this, two samples of $Ag_{80}Au_{19}Pt_1$ alloy were made to study the critical ligament size to form a nanoporous structure on a nanosized ligament. One $Ag_{80}Au_{19}Pt_1$ alloy was directly dealloyed

at 1000 mV which is designated as Condition I and another sample was first dealloyed at 650 mV and after the first dealloying an additional dealloying at 1000 mV was performed to further remove Ag which is designated as Condition II.

Figure 5.14 shows the cross section view of Condition I. It can be found that the ligament size is quite small which is also about 6 nm. SEM image of the cross section view of Condition II is shown in Figure 5.15 as a comparison. No lower hierarchy level ligaments can be observed from the present SEM image. In order to verify the presence of the lower hierarchy level ligaments, the SAXS measurement was performed to examine the porous structure in the sample of Condition II.
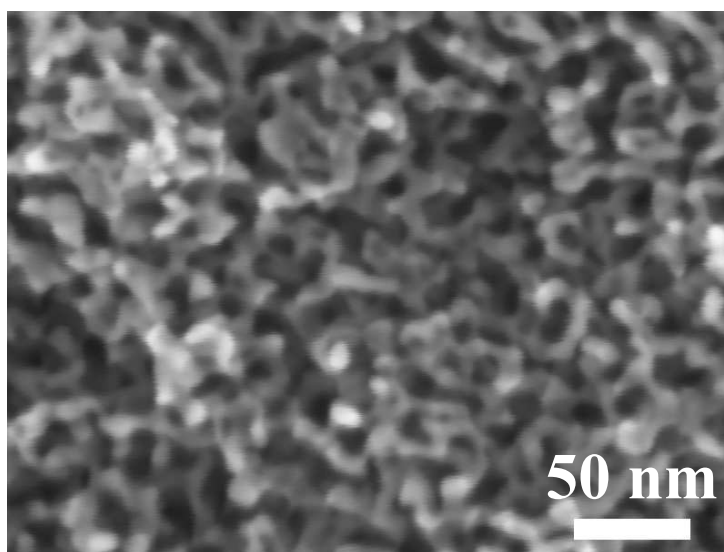

Figure 5.14: Scanning electron micrograph showing the cross section view of a $Ag_{80}Au_{19}Pt_1$ alloy dealloyed directly at 1000 mV.

The corresponding SAXS result is shown in Figure 5.16. As a comparison the data of the sample dealloyed at 650 mV is also shown in the same figure. It is seen that only one peak appears at the region close to the sample dealloyed at 650 mV and no hump can be found at the low q range which indicates that no fine structure below 10 nm can be found in the present sample. The ligament size estimated from the present SAXS results is ~ 27 nm which is the same ligament size as the sample dealloyed at 650 mV. The SAXS results are consistent with the SEM observation. Thus, no lower hierarchy level ligament was created during the second dealloying for the sample without the annealing step. Therefore, it is suggested that a critical upper hierarchy level ligament size exists as a threshold above which the lower hierarchy level ligaments can be created. Similar findings were reported in Jin's work [91]. The nanoporous Ag-Au and Ag-Au-Pt alloys were obtained by controlled dealloying. The results suggest that no porosity can be found after dealloying of those nanoporous alloys.

Recently, Li *et al.* [95] investigated the formation of nanoporous structures from the different sizes of nanoparticles. An interesting finding is that the formation of a nanoporous structure within a nanoparticle shows a strong dependence on the nanoparticle size. Nanoporous structure forms when the nanoparticle size is larger than 25 nm, whereas only Ag dissolution is found
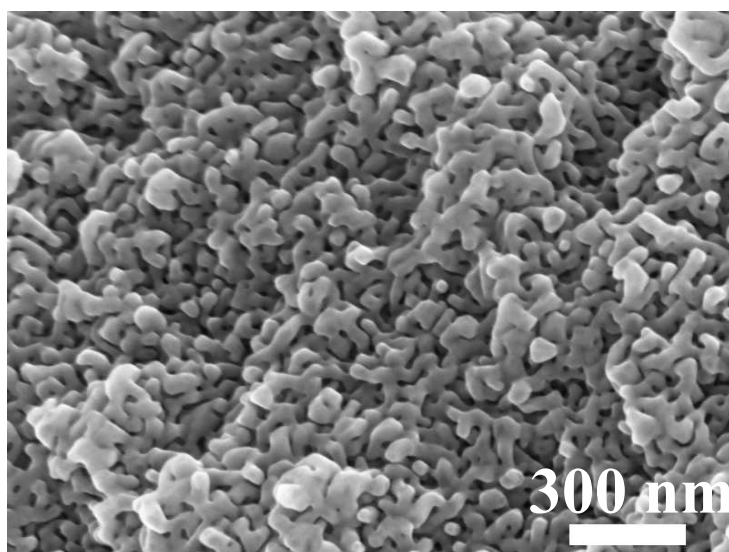
Figure 5.15: Scanning electron micrograph showing the cross section view of $Ag_{80}Au_{19}Pt_1$ alloy first dealloyed at 650 mV and after the first dealloying an additional dealloying was performed at 1000 mV to further remove the Ag retention.

with nanoparticles who have smaller size. Kinetic Monte Carlo simulations were applied to the Ag-Au alloy nanoparticles to understand their dealloying behaviors [96]. An increase of the dealloying potential towards the formation of nanoporous structure in a nanoparticle with small size was found. Here, they mean that at least 50 % of porosity should form in the nanoparticle, otherwise, it is just dissolution of Ag without a pore formation. Based on the facts of those nanoparticle dealloying experiments and simulations, the initial ligament size of nanoporous Ag-Au-Pt alloy is ~ 22 nm which is below the size for nanoparticles to form a nanoporous structure. Additionally, Pt will passivate the surface due to its slow diffusion nature and segregate to the surface which forms a Pt enriched layer hindering the Ag dissolution. Therefore, it is expected that no nanoporous structure could be created from its initial ligament size. By annealing to coarsen the ligaments to a larger size, nanoporosity forms on those coarsened ligaments after dealloying.
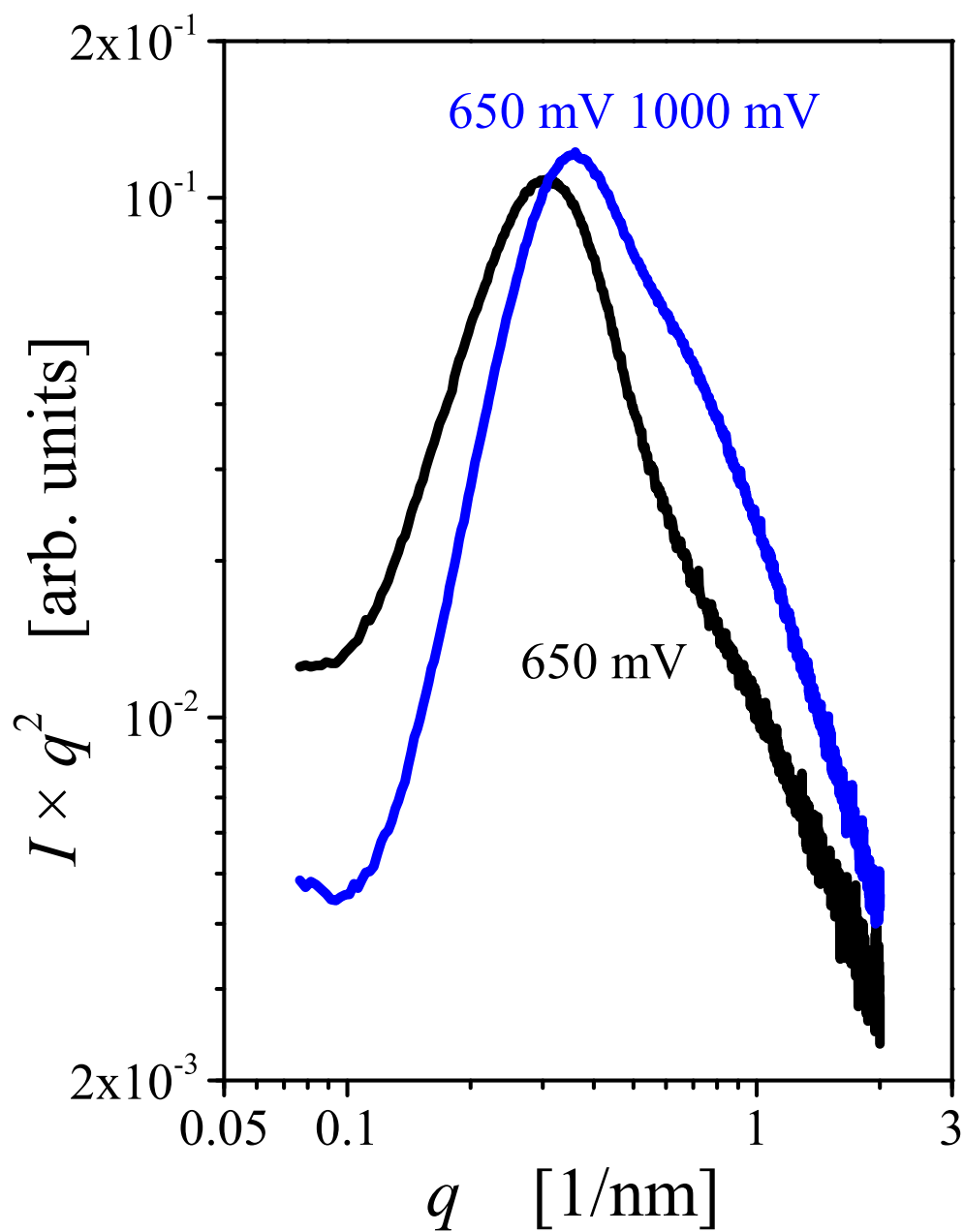
Figure 5.16: Small angle X-ray scattering curves of one $Ag_{80}Au_{19}Pt_1$ alloy dealloyed at 650 mV (black), and another first dealloyed at 650 mV and after the first dealloying directly deallyed at 1000 mV (blue).

5.4 Conclusion

In summary, another similar two-step dealloying approach like the dilute Ag-Au alloy towards fabrication of N³PG with an ultrafine lower hierarchy level ligament size is proposed. Starting out from a Pt doped Ag-Au alloy, a high Ag retention (46 at.%) which is close to the parting limit is maintained. By tailoring the annealing temperature and time, the upper hierarchy level ligament size can be modulated. A second dealloying step creates the lower hierarchy level ligaments. Compared with the dilute Ag-Au alloy where a volume shrinkage is up to 60 % occurs, the volume shrinkage of the Pt doped Ag-Au alloys is only 20 % which is within the range of NPG shrinkage prepared from the standard composition range. The lower hierarchy level ligament size is as small as 6 nm. The electron backscattering diffraction results suggest that the grain size remains the same as the master alloy when the hierarchical structure formed. Small angle X-ray scattering results confirm the existence of the ultrafine ligaments and the estimated ligament size is in good agreement with the SEM results. The present strategy is capable of producing bulk samples with a small volume shrinkage and ultrafine lower hierarchy level ligaments.

Chapter 6

Summary and outlook

6.1 Summary

Various strategies have been reported to prepare bimodal or hierarchical nanoporous gold (NPG). However, none of the present methods is capable of fabricating NPG with two levels of ligament size with a self-similar structure starting from a bulk sample. The contribution of the present thesis is that a novel two-step dealloying strategy towards fabricating hierarchical NPG starting with a bulk form alloy has been developed. The hierarchical NPG obtained by the present two-step dealloying strategy is defined as nested-network nanoporous gold, N^3PG. By deliberately controlling the dealloying process, a high Ag retention alloy which is close to the parting limit can be obtained. The high Ag retention is the core requirement to perform a second dealloying. The high Ag-content NPG is followed by coarsening the structure via annealing which results in the formation of the upper hierarchy level ligaments. Those are then treated by a second dealloying to yield the lower hierarchy level ligaments. The main findings of the research covered in this thesis can be summarized as follows:

i) Dilute Ag-Au alloy

A crucial issue to control the Ag retention is the correct choice of the dealloying conditions. To clarify the ambiguity of the determination of the critical dealloying potential, linear sweep voltammetry measurements and loss of passivation potential (LPP) by potential holding experiments were carried out to determine the true critical dealloying potential. It is found that the LPP is close to the true critical dealloying potential. By controlling the dealloying potential of the dilute Ag-Au alloys, the Ag retention can be controlled accordingly. A remarkable Ag retention up to 48 at.% can be found by dealloying the $Ag_{95}Au_5$ alloy. The high Ag retention is a prerequisite to conduct a second dealloying step to create the lower hierarchy level ligaments. The Ag retention decreases with increasing dealloying potential. A volume contraction to ~ 39 % of the original size and the development of cracks at the scale of 20-100 μm during the first dealloying step are found. Considering more than 80 wt.% of the original weight was removed from the alloy during dealloying, it is without doubt such a huge volume shrinkage can be observed.

Through selecting proper annealing parameters, the upper hierarchy level ligaments can be tuned from its initial size to several microns. By applying a second dealloying step, the lower hierarchy level ligaments are created with a ligament size of ~ 15 nm. The upper hierarchy level ligaments were well preserved after the second dealloying step, no further shrinkage was observed during this step. The corresponding hierarchical NPG shows a nested network structure with self similar ligaments in two length scales. Using two different electrochemical methods including the capacitance in the double layer region and the Au oxidation reduction peak, the surface areas were evaluated. The results show that both methods proved the N^3PG (3.0 m^2 g^{-1}) has a specific surface area as large as NPG. A simple charging experiment was performed in the double region, N^3PG shows an acceleration of the signal transport into the pore space by more than two orders of magnitude, as compared to conventional NPG with comparable mass-specific surface area.

ii) Pt doped Ag-Au alloy

Inspired by Jin's work [91], another two-step dealloying strategy towards fabricating N^3PG with an ultrafine ligament size was developed from the Pt doped Ag-Au alloys. By replacing 1 at.% of Au by Pt, a significant less noble element retention is found. One advantage due to Pt doping is that the volume shrinkage becomes less, only 20 % compared with the dilute Ag-Au alloys. Crack free sample can be prepared from the Pt doped Ag-Au alloys after dealloying. The critical dealloying potential of the Pt doped Ag-Au alloys was determined directly by the LPP method. The ligament size after the first dealloying step is ~ 22 nm. A high Ag retention was found after the first dealloying which is up to 46 at.%. Similar to the dealloying of dilute Ag-Au alloys, the upper hierarchy level ligaments can be modulated by annealing. After the second dealloying step, an ultrafine ligament size is observed to be as small as 6 nm which greatly increases the surface area. The ultrafine ligament is related to the Pt addition where the fast diffusivity of Au is slowed down [27, 97]. X-ray diffraction results suggest that the lattice planes remain the same at each stage. Electron backscattering diffraction measurements confirm the crystal orientation is well maintained from the master alloy. The ultrafine ligaments were also characterized by small angle X-ray scattering which suggests that the lower hierarchical ligament size is ~ 6.5 nm.

6.2   Outlook

The present thesis demonstrates that the two-step dealloying strategy of fabricating N^3PG with self-similar structures from two alloy systems: the dilute Ag-Au alloys and the Pt doped Ag-Au alloys. Several issues are worth noting as future work:

The universality of the high less noble element retention in the dilute binary solid solution alloys is an interesting issue for understanding the role of the less noble elements during corrosion. The dilute Cu-Au alloy [54] is the first evidence to verify this observation, although only a certain thickness of dealloyed material was examined. The present results support these findings. It will be interesting to explore to use the dilute Cu-Au alloys as a candidate for making hierarchical NPG with self-similar structures, because a large atomic size mismatch between Cu and Au atoms where a less volume contraction is expected.

It is well known that NPG has various applications such as catalysts, sensors, actuators and etc. To explore the potential applications of the N³PG in this context would be the topmost work to be done in the future. It is expected that this hierarchical NPG is a good candidate towards catalyst and sensor applications since it can enhance the mass (gas or ions) and charge (in electrolyte) transport, therefore, accelerate the chemical reactions at the interface and the speed of signal transmission.

The effect of the third element towards stabilizing the less noble elements in the ternary alloy systems, especially, those with a low surface diffusivity such as Pd, is expected to be an potential work upon developing new alloy systems to fabricate hierarchical structures with an ultrafine lower hierarchy level ligament.

Using a neutral solution $AgNO_3$ as the dealloying solution, as stated by Snyder's work [59, 97] where Ag oxides formed which assists pinning the less noble elements, a high less noble element retention is expected to be maintained after the dealloying. This strategy can start with a high initial Au content within the standard composition range to prepare NPG in the master alloys.

NPG shows potential applications in automotive emission control even at low temperature. It has been suggested [98] that the distribution of Ag in NPG could have a strong influence on the catalytic mechanism. However, there are no relevant studies on of Ag residues effect on the catalytic properties for CO oxidation. Since the amount of Ag in NPG can be controlled, the present study shows how nanoporous metal with high Ag content can be synthesized, thereby opening a pathway towards answering this question.

Reference

[1] G.Z. Cao. *Nanostructures & Nanomaterials: Synthesis, Properties, and Applications*. Imperial College Press, 2004.

[2] H.D. Yu, M.D. Regulacio, E.Y. Ye, and M.Y. Han. Chemical routes to top-down nanofabrication. *Chem. Soc. Rev.*, 42:6006–6018, 2013.

[3] Y. Ding and J. Erlebacher. Nanoporous metals with controlled multimodal pore size distribution. *J. Am. Chem. Soc.*, 125:7772–7773, 2003.

[4] J. Biener. Nanoscale synthesis and characterization laboratory overview for FY2005. Technical report, Argonne National Laboratory, 2005.

[5] J. Biener, G.W. Nyce, A.M. Hodge, M.M. Biener, A.V. Hamza, and S.A. Maier. Nanoporous plasmonic metamaterials. *Adv. Mater.*, 20:1211–1217, 2008.

[6] Z.H. Zhang, Y. Wang, Z. Qi, J.K. Lin, and X.F. Bian. Nanoporous gold ribbons with bimodal channel size distributions by chemical dealloying of Al-Au alloys. *J. Phys. Chem. C*, 113:1308–1314, 2009.

[7] M.E. Cox and D.C. Dunand. Bulk gold with hierarchical macro-, micro-and nano-porosity. *Mater. Sci. Eng. A*, 528:2401–2406, 2011.

[8] X.F. Xing, D.Q. Han, Y.F. Wu, Y. Guan, N. Bao, and X.H. Xu. Fabrication and electrochemical property of hierarchically porous Au-Cu films. *Mater. Lett.*, 71:108–110, 2012.

[9] X.G. Wang, J.Z. Sun, C. Zhang, T.Y. Kou, and Z.H. Zhang. On the microstructure, chemical composition, and porosity evolution of nanoporous alloy through successive dealloying of ternary Al-Pd-Au precursor. *J. Phys. Chem. C*, 116(24):13271–13280, 2012.

[10] S. Sattayasamitsathit, A.M. O'ahony, X.Y. Xiao, S.M. Brozik, C.M. Washburn, D.R. Wheeler, W. Gao, S. Minteer, J. Cha, D.B. Burckel, R. Polsky, and J. Wang. Highly ordered tailored three-dimensional hierarchical nano/microporous gold-carbon architectures. *J. Mater. Chem.*, 22:11950–11956, 2012.

[11] M.N. Lee, M.A. Santiago-Cordoba, C.E. Hamilton, N.K. Subbaiyan, J.G. Duque, and K.A.D. Obrey. Developing monolithic nanoporous gold with hierarchical bicontinuity using colloidal bijels. *J. Phys. Chem. Lett.*, 5:809–812, 2014.

[12] J. Erlebacher, M.J. Aziz, A. Karma, N. Dimitrov, and K. Sieradzki. Evolution of nanoporosity in dealloying. *Nature*, 410:450–453, 2001.

[13] J. Weissmüller, R.C. Newman, H. J. Jin, A.M. Hodge, and J.W. Kysar. Nanoporous metals by alloy corrosion: Formation and mechanical properties. *MRS Bull.*, 34:577–586, 2009.

[14] J. Erlebacher and K. Sieradzki. Pattern formation during dealloying. *Scr. Mater.*, 49:991–996, 2003.

[15] http://www.corrosion.org/images_index/nowisthetime.pdf.

[16] H.J. Jin, D. Kramer, Y. Ivanisenko, and J. Weissmüller. Macroscopically strong nanoporous Pt prepared by dealloying. *Advanced Engineering Materials*, 9:849–854, 2007.

[17] M. Hakamada, H. Nakano, T. Furukawa, M. Takahashi, and M. Mabuchi. Hydrogen storage properties of nanoporous palladium fabricated by dealloying. *J. Phys. Chem. C*, 114:868–873, 2009.

[18] X.G. Wang, Z. Qi, C.C. Zhao, W.M. Wang, and Z.H. Zhang. Influence of alloy composition and dealloying solution on the formation and microstructure of monolithic nanoporous silver through chemical dealloying of Al-Ag alloys. *J. Phys. Chem. C*, 113:13139–13150, 2009.

[19] Z. Qi, C.C. Zhao, X.G. Wang, J.K. Lin, W. Shao, Z.H. Zhang, and X.F. Bian. Formation and characterization of monolithic nanoporous copper by chemical dealloying of Al-Cu alloys. *J. Phys. Chem. C*, 113:6694–6698, 2009.

[20] Z.H. Zhang, Y. Wang, Z. Qi, W.H. Zhang, J.Y. Qin, and J. Frenzel. Generalized fabrication of nanoporous metals (Au, Pd, Pt, Ag, and Cu) through chemical dealloying. *J. Phys. Chem. C*, 113:12629–12636, 2009.

[21] Z.H. Zhang, Y. Wang, Y.Z. Wang, X.G. Wang, Z. Qi, H. Ji, and C.C. Zhao. Formation of ultrafine nanoporous gold related to surface diffusion of gold adatoms during dealloying of Al_2Au in an alkaline solution. *Scr. Mater.*, 62:137–140, 2010.

[22] T. Wada, K. Yubuta, A. Inoue, and H. Kato. Dealloying by metallic melt. *Mater. Lett.*, 65:1076–1078, 2011.

[23] Y.C.K. Chen-Wiegart, T. Wada, N. Butakov, X.H. Xiao, F. De Carlo, H. Kato, J. Wang, D.C. Dunand, and E. Maire. 3D morphological evolution of porous titanium by X-ray micro-and nano-tomography. *J. Mater. Res.*, 28:2444–2452, 2013.

[24] A. Wittstock, V. Zielasek, J. Biener, C.M. Friend, and M. Bäumer. Nanoporous gold catalysts for selective gas-phase oxidative coupling of methanol at low temperature. *Science*, 327:319–322, 2010.

[25] D. Kramer, R.N. Viswanath, and J. Weissmüller. Surface-stress induced macroscopic bending of nanoporous gold cantilevers. *Nano Lett.*, 4:793–796, 2004.

[26] J. Biener, A. Wittstock, L.A. Zepeda-Ruiz, M.M. Biener, V. Zielasek, D. Kramer, R.N. Viswanath, J. Weissmüller, M. Bäumer, and A.V. Hamza. Surface-chemistry-driven actuation in nanoporous gold. *Nat. Mater.*, 8:47–51, 2009.

[27] H.J. Jin, X.L. Wang, S. Parida, K. Wang, M. Seo, and J. Weissmüller. Nanoporous Au-Pt alloys as large strain electrochemical actuators. *Nano Lett.*, 10:187–194, 2010.

[28] H.J. Jin and J. Weissmüller. A material with electrically tunable strength and flow stress. *Science*, 332:1179–1182, 2011.

[29] P. Wahl, T. Traußnig, S. Landgraf, H.J. Jin, J. Weissmüller, and R. Würschum. Adsorption-driven tuning of the electrical resistance of nanoporous gold. *J. Appl. Phys.*, 108:073706, 2010.

[30] E.M. Steyskal, M. Besenhard, S. Landgraf, Y. Zhong, J. Weissmüller, P. Pölt, M. Albu, and R. Würschum. Sign-inversion of charging-induced variation of electrical resistance of nanoporous platinum. *J. Appl. Phys.*, 112:073703, 2012.

[31] Y. Ding and M.W. Chen. Nanoporous metals for catalytic and optical applications. *MRS Bull.*, 34:569–576, 2009.

[32] J. Snyder, T. Fujita, M.W. Chen, and J. Erlebacher. Oxygen reduction in nanoporous metal-ionic liquid composite electrocatalysts. *Nat. Mater.*, 9:904–907, 2010.

[33] L.C. Wang, Y. Zhong, H.J. Jin, D. Widmann, J. Weissmüller, and R.J. Behm. On the role of residual Ag in nanoporous Au catalysts for CO oxidation: A combined microreactor and TAP reactor study. *ChemCatChem*, 4:251–259, 2012.

[34] Y. Ding, Y.J. Kim, and J. Erlebacher. Nanoporous gold leaf:Ancient technology/advanced material. *Adv. Mater.*, 16:1897–1900, 2004.

[35] M. Hakamada and M. Mabuchi. Nanoporous gold prism microassembly through a self-organizing route. *Nano Lett.*, 6:882–885, 2006.

[36] L. Zhang, L.Y. Chen, H.W. Liu, Y. Hou, A. Hirata, T. Fujita, and M.W. Chen. Effect of residual silver on surface-enhanced raman scattering of dealloyed nanoporous gold. *J. Phys. Chem. C*, 115:19583–19587, 2011.

[37] B.L. Su, C. Sanchez, and X.Y. Yang. *Hierarchically Structured Porous Materials*. Wiley-VCH Verlag & Co. KGaA, 2011.

[38] R. Lakes. Materials with structural hierarchy. *Nature*, 361:511–515, 1993.

[39] Reprinted from (Ref. [3]), (Ref. [6]) and (Ref. [9]) with permission of Copyright (2003), Copyright (2009), and Copyright (2012) American Chemical Society. From (Ref. [10]), with permissions of Copyright (2012) Royal Society of Chemistry. From (Ref. [7]) and (Ref. [8]) with permissions of Copyright (2011) and Copyright (2012) Elsevier. From (Ref [5]) with permissions of Copyright (2008) John Wiley and Sons. From (Ref. [4]) with permissions of Copyright (2005) LLNL.

[40] H.J. Jin, L. Kurmanaeva, J. Schmauch, H. Rösner, Y. Ivanisenko, and J. Weissmüller. Deforming nanoporous metal: Role of lattice coherency. *Acta Mater.*, 57:2665–2672, 2009.

[41] S. Parida, D. Kramer, C.A. Volkert, H. Rösner, J. Erlebacher, and J. Weissmüller. Volume change during the formation of nanoporous gold by dealloying. *Phys. Rev. Lett.*, 97:035504, 2006.

[42] A.J. Bard and L.R. Faulkner. *Electrochemical Methods: Fundamentals and Applications. 2nd Ed.* Wiley, New York., 2001.

[43] A.J. Bard, G. Inzelt, and F. Scholz. *Electrochemical Dictionary. 2nd Ed.* Springer, 2012.

[44] http://iramis.cea.fr/Phocea/Vie_des_labos/Ast/ast_sstechnique.php?id_ast=1065.

[45] S.K. Sinha, E.B. Sirota, and S. Garoff. X-ray and neutron scattering from rough surfaces. *Phys. Rev. B*, 38:2297–2311, 1988.

[46] K. Sieradzki, N. Dimitrov, D. Movrin, C. McCall, N. Vasiljevic, and J. Erlebacher. The dealloying critical potential. *J. Electrochem. Soc.*, 149:B370–B377, 2002.

[47] J. Snyder and J. Erlebacher. Kinetics of crystal etching limited by terrace dissolution. *J. Electrochem. Soc.*, 157:C125–C130, 2010.

[48] J. Erlebacher. An atomistic description of dealloying. *J. Electrochem. Soc.*, 151:C614–C626, 2004.

[49] A. Dursun, D.V. Pugh, and S.G. Corcoran. Dealloying of Ag-Au alloys in halide-containing electrolytes affect on critical potential and pore size. *J. Electrochem. Soc.*, 150:B355–B360, 2003.

[50] Y. Zhong, J. Markmann, H.J. Jin, Y. Ivanisenko, L. Kurmanaeva, and J. Weissmüller. Crack mitigation during dealloying of $Au_{25}Cu_{75}$. *Adv. Eng. Mater.*, 16:389–398, 2013.

[51] H. Okamoto and T.B. Massalski. *Phase diagrams of binary gold alloys*. ASM International Metals Park, OH, 1987.

[52] N.A. Senior and R.C. Newman. Synthesis of tough nanoporous metals by controlled electrolytic dealloying. *Nanotechnology*, 17:2311–2316, 2006.

[53] A.M. Hodge, R.T. Doucette, M.M. Biener, J. Biener, O. Cervantes, and A.V. Hamza. Ag effects on the elastic modulus values of nanoporous Au foams. *J. Mater. Res.*, 24:1600–1606, 2009.

[54] B.G. Ateya, J.D. Fritz, and H.W. Pickering. Kinetics of dealloying of a copper-5 atomic percent gold alloy. *J. Electrochem. Soc.*, 144:2606–2613, 1997.

[55] B.G. Ateya, G. Geh, A.H. Carim, and H.W. Pickering. Selective dissolution below the critical potential and back alloying in copper-gold alloy. *J. Electrochem. Soc.*, 149:B27–B33, 2002.

[56] K. Wang and J. Weissmüller. Composites of nanoporous gold and polymer. *Adv. Mater.*, 25:1280–1284, 2013.

[57] F. Kertis, J. Snyder, L. Govada, S. Khurshid, N. Chayen, and J. Erlebacher. Structure/processing relationships in the fabrication of nanoporous gold. *JOM*, 62:50–56, 2010.

[58] L.H. Qian and M.W. Chen. Ultrafine nanoporous gold by low-temperature dealloying and kinetics of nanopore formation. *Appl. Phys. Lett.*, 91:083105–083105, 2007.

[59] J. Snyder, P. Asanithi, A. B Dalton, and J. Erlebacher. Stabilized nanoporous metals by dealloying ternary alloy precursors. *Adv. Mater.*, 20:4883–4886, 2008.

[60] D.V. Pugh, A. Dursun, and S.G. Corcoran. Formation of nanoporous platinum by selective dissolution of Cu from $Cu_{0.75}Pt_{0.25}$. *J. Mater. Res.*, 18:216–221, 2003.

[61] C. J. Dotzler, B. Ingham, B. N. Illy, K. Wallwork, M. P. Ryan, and M. F. Toney. In situ observation of strain development and porosity evolution in nanoporous gold foils. *Advanced Functional Materials*, 21:3938–3946, 2011.

[62] NF Berk. Scattering properties of a model bicontinuous structure with a well defined length scale. *Physical review letters*, 58:2718, 1987.

[63] A. Michels and J. Weissmuller. Magnetic-field-dependent small-angle neutron scattering on random anisotropy ferromagnets. *Reports on Progress in Physics*, 71:066501, 2008.

[64] H.J. Jin, S. Parida, D. Kramer, and J. Weissmüller. Sign-inverted surface stress-charge response in nanoporous gold. *Surf. Sci.*, 602:3588–3594, 2008.

[65] A. Dursun, D.V. Pugh, and S.G. Corcoran. Probing the dealloying critical potential. *J. Electrochem. Soc.*, 152:B65–B72, 2005.

[66] Q. Zhang and Z.H. Zhang. On the electrochemical dealloying of Al-based alloys in a NaCl aqueous solution. *Phys. Chem. Chem. Phys.*, 12:1453–1472, 2010.

[67] C.C. Zhao, X.G. Wang, Z. Qi, H. Ji, and Z.H. Zhang. On the electrochemical dealloying of Mg-Cu alloys in a NaCl aqueous solution. *Corros. Sci.*, 52:3962–3972, 2010.

[68] S. Trasatti and A. Petrii. Real surface area measurements in electrochemistry. *Pure Appl. Chem.*, 63:711–734, 1991.

[69] P.S. Germain, W.G. Pell, and B.E. Conway. Evaluation and origins of the difference between double-layer capacitance behaviour at Au-metal and oxidized Au surface. *Electrochim. Acta*, 49:1775–1788, 2004.

[70] N. Asao, N. Hatakeyama, Menggenbateer, T. Minato, E. Ito, M. Hara, Y. Kim, Y. Yamamoto, M.W. Chen, W. Zhang, and A. Inoue. Aerobic oxidation of alcohols in the liquid phase with nanoporous gold catalysts. *Chem. Commun.*, 48:4540–4542, 2012.

[71] http://serc.carleton.edu/research_education/geochemsheets/wds.html.

[72] Z. Qi and J. Weissmüller. Hierarchical nested-network nanostructure by dealloying. *ACS Nano*, 7:5948–5954, 2013.

[73] H.W. Pickering. Characteristic features of alloy polarization curves. *Corro. Sci.*, 23:1107–1120, 1983.

[74] Dorota Artymowicz, Zoe Coull, Mariusz Bryk, and Roger Newman. Distribution of the retained less-noble element in dealloyed materials. *ECS Transactions*, 33:1–14, 2011.

[75] E. Rouya, S. Cattarin, M.L. Reed, R.G. Kelly, and G. Zangari. Electrochemical characterization of the surface area of nanoporous gold films. *J. Electrochem. Soc.*, 159:K97–K102, 2012.

[76] Y.H. Tan, J.A. Davis, K. Fujikawa, N.V. Ganesh, A.V. Demchenko, and K.J. Stine. Surface area and pore size characteristics of nanoporous gold subjected to thermal, mechanical, or surface modification studied using gas adsorption isotherms, cyclic voltammetry, thermogravimetric analysis, and scanning electron microscopy. *J. Mater. Chem.*, 22:6733–6745, 2012.

[77] J. Richer and J. Lipkowski. Measurement of physical adsorption of neutral organic species at solid electrodes. *J. Electrochem. Soc.*, 131:121–128, 1986.

[78] K. Fitzner, Q.T. Guo, J.W. Wang, and Kleppa O.J. Enthalpies of liquid-liquid mixing in the systems Cu-Ag, Cu-Au and Ag-Au by using an in-situ mixing device in a high temperature single-unit differential calorimeter. *J. Alloys Compound.*, 291:190–200, 1999.

[79] R.C. Newman, S.G. Corcoran, J. Erlebacher, M.J. Aziz, and K. Sieradzki. Alloy corrosion. *MRS Bull.*, 24:24–28, 1999.

[80] P. Strasser, S. Koh, and J. Greeley. Voltammetric surface dealloying of Pt bimetallic nanoparticles: an experimental and DFT computational analysis. *Phys. Chem. Chem. Phys.*, 10:3670–3683, 2008.

[81] M. Kamundi, L. Bromberg, E. Fey, C. Mitchell, M. Fayette, and N. Dimitrov. Impact of structure and composition on the dealloying of $Au_xAg_{(1-x)}$ alloys on the nanoscale. *J. Phys. Chem. C*, 116:14123–14133, 2012.

[82] L. Tang, B.C. Han, K. Persson, C. Friesen, T. He, K. Sieradzki, and G. Ceder. Electrochemical stability of nanometer-scale Pt particles in acidic environments. *J. Am. Chem. Soc.*, 132:596–600, 2009.

[83] O.S. Ivanova and F.P. Zamborini. Electrochemical size discrimination of gold nanoparticles attached to glass/indium-tin-oxide electrodes by oxidation in bromide-containing electrolyte. *Anal. Chem.*, 82:5844–5850, 2010.

[84] L. Tang, X.Q. Li, R.C. Cammarata, C. Friesen, and K. Sieradzki. Electrochemical stability of elemental metal nanoparticles. *J. Am. Chem. Soc.*, 132:11722–11726, 2010.

[85] W.J. Plieth. Electrochemical properties of small clusters of metal atoms and their role in the surface enhanced raman scattering. *J. Phys. Chem.*, 86:3166–3170, 1982.

[86] W.J. Plieth. The work function of small metal particles and its relation to electrochemical properties. *Surf. Sci.*, 156:530–535, 1985.

[87] A. Henglein. Remarks on the electrochemical potential of small silver clusters in aqueous solution. *Berichte der Bunsengesellschaft für physikalische Chemie*, 94:600–603, 1990.

[88] A. Henglein. Physicochemical properties of small metal particles in solution: "microelectrode" reactions, chemisorption, composite metal particles, and the atom-to-metal transition. *J. Phys. Chem.*, 97:5457–5471, 1993.

[89] A.A. Vega and R.C. Newman. Nanoporous metals fabricated through electrochemical dealloying of Ag-Au-Pt with systematic variation of Au: Pt ratio. *J. Electrochem. Soc.*, 161:C1–C10, 2014.

[90] A.A. Vega and R.C. Newman. Beneficial effects of adsorbate-induced surface segregation of Pt in nanoporous metals fabricated by dealloying of Ag-Au-Pt alloys. *J. Electrochem. Soc.*, 161:C11–C19, 2014.

[91] X.L. Ye, N. Lu, X.J. Li, K. Du, J. Tan, and H.J. Jin. Primary and secondary dealloying of Au(Pt)-Ag: Structural and compositional evolutions, and volume shrinkage. *J. Electrochem. Soc.*, 161:C517–C526, 2014.

[92] André Guinier. *X-ray diffraction in crystals, imperfect crystals, and amorphous bodies.* Courier Dover Publications, 1994.

[93] A.S. Edelstein and R.C. Cammaratra. *Nanomaterials: synthesis, properties and applications.* CRC Press, 1998.

[94] R.C. Newman. A theory of secondary alloying effects on corrosion and stress-corrosion cracking. *Corros. Sci.*, 33:1653–1657, 1992.

[95] X.Q. Li, Q. Chen, I. McCue, J. Snyder, P. Crozier, J. Erlebacher, and K. Sieradzki. Dealloying of noble-metal alloy nanoparticles. *Nano Lett.*, 14:25692577, 2014.

[96] I. McCue, J. Snyder, X. Li, Q. Chen, K. Sieradzki, and J. Erlebacher. Apparent inverse Gibbs-Thomson effect in dealloyed nanoporous nanoparticles. *Phys. Rev. Lett.*, 108:225503, 2012.

[97] J. Snyder, K. Livi, and J. Erlebacher. Dealloying silver/gold alloys in neutral silver nitrate solution: Porosity evolution, surface composition, and surface oxides. *J. Electrochem. Soc.*, 155:C464–C473, 2008.

[98] V. Zielasek, B. Jürgens, C. Schulz, J. Biener, M.M. Biener, A.V. Hamza, and M. Bäumer. Gold catalysts: nanoporous gold foams. *Angew. Chem. Int. Ed.*, 45:8241–8244, 2006.

Curriculum Vitae

Personal Data

Name	Qi
First Name	Zhen
Date of Birth	11 August, 1984
Place of Birth	Shandong, People's Republic of China

Education

09.1991 – 07.1997   Jinan Railway No.3 Elementary School, Shandong, China

09.1997 – 07.2000   Jinan Railway No.2 Middle School, Shandong, China

09.2000 – 07.2003   Jinan No.3 High School, Shandong, China

09.2003 – 07.2007   Bachelor in School of Materials Science and Engineering.
Shandong University, Ji'nan, China
Major: Materials Science and Engineering

09.2007 – 07.2009   Master in School of Materials Science and Engineering
Shandong University, Ji'nan, China
Major: Materials Engineering

09.2009 – 10.2010   Master-Doctorate in School of Materials Science and Engineering
Shandong University, Ji'nan, China
Major: Materials Engineering

10.2010 – present   Ph.D study at the Institute of Materials Physics and Materials Technology,
Hamburg University of Technology, Hamburg, Germany

Honors and Awards

2008   China-Japan Komatsu Scholarship, Shandong University
2009   Excellent Graduate Students Scholarship, Shandong University
2011   Zhongyan Scholarship, Shandong University